Investigation of inner-shell and subsequent field-induced processes in mono- and diatomic systems

Dissertation zur Erlangung des Doktorgrades
des Fachbereiches Physik
der Universität Hamburg

vorgelegt von
Murali Krishna Ganesa Subramanian

Hamburg
2022

Gutachter/innen der Dissertation:	Prof. Dr. Robin Santra
	Prof. Dr. Oriol Vendrell
Zusammensetzung der Prüfungskommission:	Prof. Dr. Robin Santra
	Prof. Dr. Oriol Vendrell
	Prof. Dr. Carmen Herrmann
	Prof. Dr. Markus Drescher
	Prof. Dr. Daniela Pfannkuche
Vorsitzende/r der Prüfungskommission:	Prof. Dr. Daniela Pfannkuche
Datum der Disputation:	13.05.2022
Vorsitzender Fach-Promotionsausschuss PHYSIK:	Prof. Dr. Wolfgang J. Parak
Leiter des Fachbereichs PHYSIK:	Prof. Dr. Günter H. W. Sigl
Dekan der Fakultät MIN:	Prof. Dr. Heinrich Graener

Eidesstattliche Versicherung/Declaration on oath

Hiermit versichere ich an Eides statt, die vorliegende Dissertationsschrift selbst verfasst und keine anderen als die angegebenen Hilfsmittel und Quellen benutzt zu haben.

Hamburg, den 21.02.2022

Unterschrift der Doktorandin/des Doktoranden

Abstract

With advent of modern experimental techniques using light sources, the dynamics initiated by inner-shell processes such as, inner-shell ionization followed by Auger-decay, and their subsequent dynamics can be investigated in their fundamental timescales. Theoretical description supported by computational methods are needed to complement the experimental investigations [1]. Comparing the experimental and theoretical results are important to interpret the results from the experiments. In this thesis, theoretical and computational methods will be presented which demonstrates the ability to investigate field-induced processes in mono- and diatomic systems.

Zusammenfassung

Mit dem Aufkommen moderner experimenteller Techniken, die Lichtquellen verwenden, kann die Dynamik, die durch Prozesse in der inneren Schale ausgelöst wird, wie z. B. Ionisierung in der inneren Schale, gefolgt von Auger-Zerfall, und ihre anschließende Dynamik in ihren fundamentalen Zeitskalen untersucht werden. Theoretische Beschreibungen, unterstützt durch rechnerische Methoden, sind notwendig, um die experimentellen Untersuchungen zu ergänzen [1]. Der Vergleich der experimentellen und theoretischen Ergebnisse ist wichtig, um die Ergebnisse der Experimente zu interpretieren. In dieser Arbeit werden theoretische und rechnerische Methoden vorgestellt, die die Fähigkeit demonstrieren, feldinduzierte Prozesse in mono- und diatomaren Systemen zu untersuchen.

Acknowledgements

I like to express my gratitude to my parents, family and friends for supporting me and for being there for me always. Last but not least, my heartfelt gratitude to my life companion and love, Ms. Rohini Vijayan, who had to put up with me every single day and constantly backed up. Without her, I would not have come to the place where I am now. Thank you so much!

List of Publications

1. *"Field-enabled quantum interference in atomic Auger decay"*,

   M. K. G. Subramanian, R. Brannath, R. Welsch, R. Santra, M. Drescher, *Phys. Rev. A*, **102**, 022807 (2020).

2. *"Infrared-laser-pulse-enhanced ultrafast fragmentation of N_2^{2+} following Auger decay: Mixed quantum-classical simulations"*,

   M. K. G. Subramanian, R. Santra, R. Welsch, *Phys. Rev. A*, **98**, 063421 (2018).

3. *"Choice of the electronic basis for field-induced surface hopping"*,

   M. K. G. Subramanian, R. Santra, R. Welsch, *Phys. Rev. A*, **102**, 013107 (2020).

List of Abbreviations

AMO   **A**tomic and **M**olecular **O**ptics

BE   **B**inding **E**nergy

BO   **B**orn-**O**ppenheimer

DOF   **D**egrees **O**f **F**reedom

EUV   **E**xtreme **U**ltra **V**iolet

FEL   **F**ree **E**lectron **L**aser

FSSH   **F**ewest **S**witches **S**urface **H**opping

HHG   **H**igh **H**armonic **G**eneration

IBO   **I**nstantaneous **B**orn-**O**ppenheimer

IR   **I**nfra-**R**ed

KE   **K**inetic **E**nergy

LCLS   **L**inac **C**oherent **L**ight **S**ource

LHS   **L**eft-**H**and **S**ide

MD   **M**olecular **D**ynamics

ML   **M**achine **L**earning

MQC   **M**ixed **Q**uantum-**C**lassical

PES   **P**otential **E**nergy **S**urfaces

QD   **Q**uantum **D**ynamics

RHS   **R**ight-**H**and **S**ide

SH   **S**urface **H**opping

SLAC   **S**tanford **L**inear **A**ccelerator **C**enter

TDSE   **T**ime-**D**ependent **S**chrödinger **E**quation

THz   **T**era-**H**ertz

TOF   **T**ime **O**f **F**light

Contents

Chapter 1

Introduction

Atomic, molecular, and optical (AMO) science is the study of light-matter and matter-matter interaction ranging from the quantum scale of atoms, molecules, or photons to classical electrodynamics. It has yielded major technological advances in numerous fields such as manufacturing, material science, communications, space exploration, defence, energy, environment, health and transportation [2, 3]. In the field of health, magnetic resonance imaging (MRI) stands out as one of the most crucial innovations from AMO science. Or consider the continued impact of the laser, which came from AMO science, developed by scientists, such as Jun-ichi Nishizawa, Charles H. Townsend, and Gordon Gould, among many others, over 60 years ago [4, 5, 6, 7]. The laser, combined with the semiconductor community have led to numerous modern technologies, such as optical storage devices and fiber-optics-based transmission systems, that otherwise would not exists.

The light-matter and matter-matter interaction further induces dynamics of atoms and molecules in their fundamental timescales span from attosecond timescales, characteristic of electronic dynamics [8, 9, 10, 11], to femtosecond timescales, characteristic of vibration and dissociation dynamics [12, 13, 14, 15, 16], to picosecond timescales, characteristic of rotation dynamics [17, 18, 19]. The technological advances in laser sources such as table-top light sources using high-harmonic generation (HHG) and the free-electron laser (FEL) [20], have paved the way to probe such dynamics with

techniques that can achieve atomic spatial resolution and temporal resolution [21].

There are numerous processes related to light-matter interaction which initiate the dynamics of atoms and molecules at their fundamental timescales. A few selected processes relevant to this work are listed below. The atomic processes occurring for a photon (light) with sufficient energy to remove an electron from an atom or a molecule or an ion are:

1. Photoionization, whereby an electron is removed from the parent ion through photon. If an electron is removed from an inner-most shell of the parent ion, then it is called as inner-shell photoionization.

2. Photoexcitation, whereby an electron excitation takes place through photon absorption.

3. Fluorescence, whereby an excited atomic ion relaxes to a lower energy state through the emission of a photon. The excited atomic ion comes from a previous ionization process having created a hole in the inner-shell.

4. Auger-Meitner decay, whereby an excited atomic ion is relaxed to a lower energy state through the emission of another electron. It is more often referred to as Auger decay, which will be the moniker used in this thesis. Note the similarity with fluorescence, where the mediation of relaxation was a photon rather than an electron. In contrast to fluorescence, Auger decay is a radiationless decay channel.

Together with advances in experimental techniques, both quantum and classical theoretical methods play a crucial role to investigate the dynamics initiated by the above mentioned processes. The increase in computational

power, along with numerical simulation techniques, greatly benefits the scientific community using computers. This thesis focuses on presenting computational and analytical techniques to study light-matter interaction processes such as, (inner-shell) photoionization and Auger decay, and their corresponding dynamics in mono- and diatomic systems in the presence of an external electric field.

In Chapt. 2, the theory underlying the simulations employed in Paper 5.2 and 5.3 to investigate the field-induced dynamics following the previous step, photoionization followed Auger decay, is presented.

In Chapt. 3, summary of results from Paper 5.1, 5.2 and 5.3 corresponds to the process of inner-shell photoionization followed by Auger decay in the presence of an external electric field are presented.

Chapter 4 concludes the research presented in the thesis with an outlook on future directions of research.

Chapter 2

Theory framework

In this chapter, the underlying theoretical framework behind simulations employed in Papers 5.2 & 5.3 is presented. The theory related to the research done in Paper 5.1 is presented in detail in its appendix.

2.1 Molecular dynamics

Molecular dynamics (MD) can be defined as a computer simulation approach used to investigate the properties of assemblies of molecules in terms of their structure and the microscopic interactions between them. The MD is based on two underlying approximations: the Born-Oppenheimer (BO) approximation and treatment of nuclear motion using classical mechanics.

In the BO approximation, due to the large mass of a nucleus compared to that of an electron, a separation of electronic and nuclear motion is justifiable. This approximation reduces the nuclear motion to a single PES. The PES describes the energy of the molecular system with respect to, mostly, nuclear coordinates. And, after every time step, with an updated electronic structure on a PES, the nuclei are propagated using classical equations of motion. One or both of these approximations become invalid in case of nonadiabatic dynamics, where the electronic and nuclear motion are comparable to each other and includes transition among PESs. The mixed quantum-classical methods (MQC) aim to overcome the issues in traditional MD.

2.2 Tully's FSSH algorithm

Tully's FSSH algorithm is one of the most popular MQC methods. It employs a simple picture in which the system, represented by classical trajectories, evolves on a single PES. These trajectories hop from one PES to another based on a hopping probability defined using a hopping criterion. After hopping, the momentum of classical trajectory is adjusted using energy conservation laws. The derivation of Tully's FSSH algorithm is discussed below.

The nonrelativistic Hamiltonian of a molecular system, with $\mathbf{R}$ denoting the nuclear coordinates of N nuclei and $\mathbf{r}$ denoting the electronic coordinates of n electrons, given by

$$H_{mol}(\mathbf{r}, \mathbf{R}) = T_n(\mathbf{R}) + T_e(\mathbf{r}) + V_{nn}(\mathbf{R}) + V_{ee}(\mathbf{r}) + V_{en}(\mathbf{r}, \mathbf{R}), \qquad (2.1)$$

where, $T_n(\mathbf{R})$ and $T_e(\mathbf{r})$ denote KE operator of nuclei and electrons respectively, given by

$$T_n(\mathbf{R}) = -\frac{\hbar^2}{2} \sum_{J=1}^{N} \frac{\nabla_{\mathbf{R}_J}^2}{M_J}, \qquad (2.2)$$

and

$$T_e(\mathbf{r}) = -\frac{\hbar^2}{2m_e} \sum_{j=1}^{n} \nabla_{\mathbf{r}_j}^2 \qquad (2.3)$$

The repulsion operator between the nuclei, $V_{nn}(\mathbf{R})$, and the one between the electrons, $V_{ee}(\mathbf{r})$, are given by

$$V_{nn}(\mathbf{R}) = \frac{e^2}{4\pi\epsilon_0} \sum_{J=1}^{N-1} \sum_{I>J}^{N} \frac{Z_I Z_J}{|\mathbf{R}_J - \mathbf{R}_I|}, \qquad (2.4)$$

and

$$V_{ee}(\mathbf{r}) = \frac{e^2}{4\pi\epsilon_0} \sum_{j=1}^{n-1} \sum_{i>j}^{n} \frac{1}{|\mathbf{r}_j - \mathbf{r}_i|}. \tag{2.5}$$

Finally, $V_{en}(\mathbf{r}, \mathbf{R})$ denotes electron-nuclear interaction operator

$$V_{en}(\mathbf{r}, \mathbf{R}) = -\frac{e^2}{4\pi\epsilon_0} \sum_{J=1}^{N} \sum_{j=1}^{n} \frac{Z_J}{|\mathbf{r}_j - \mathbf{R}_J|}, \tag{2.6}$$

where m_e, e and n denote the mass, charge, and number of electrons, respectively. The mass and charge of the J-th nucleus are denoted by M_J and Z_J. Lastly, ϵ_0 and $\hbar$ denote the permittivity of vacuum and the reduced Planck's constant. The properties of a molecule are captured in quantum mechanics by its wave function $\Psi(\mathbf{r}, \mathbf{R}, t)$. The time-evolution of $\Psi(\mathbf{r}, \mathbf{R}, t)$ is obtained by solving the time-dependent Schrödinger equation.

At this point, the clamped-nuclei approximation is employed i.e. the change in degrees of freedom (DOF) of the nucleus is negligible on the timescale of the electronic motion. This approximation is the first step of BO approximation. It implies that the KE operator of the nucleus, $T_n(\mathbf{R})$ is set to zero (i.e., $T_n(\mathbf{R}) = 0$) and what remains is:

$$H_{el}(\mathbf{r}, \mathbf{R}) = T_e(\mathbf{r}) + V_{nn}(\mathbf{R}) + V_{ee}(\mathbf{r}) + V_{en}(\mathbf{r}, \mathbf{R}). \tag{2.7}$$

To proceed, it is assumed that the nuclear coordinate $\mathbf{R}$ can be described by classical trajectory, i.e., $\mathbf{R} = \mathbf{R}(t)$. The wave function $|\Psi(\mathbf{r}, \mathbf{R}, t)\rangle$, which describes the electronic state at time t, can be expanded in terms of orthonormal electronic basis functions $|\psi_j(\mathbf{r}; \mathbf{R})\rangle$, i.e.,

$$|\Psi(\mathbf{r}, \mathbf{R}, t)\rangle = \sum_j c_j(t) |\psi_j(\mathbf{r}; \mathbf{R})\rangle, \tag{2.8}$$

where $c_j(t)$ are the complex-valued time-dependent expansion coefficients

and the notation $|\psi_j(\mathbf{r}; \mathbf{R})\rangle$ indicates that the basis functions depend parametrically on the nuclear coordinate $\mathbf{R}$. The matrix elements of the electronic Hamiltonian H_{el} with respect to this electronic basis are given by

$$E_{kj} = \langle \psi_k(\mathbf{r}; \mathbf{R}) | H_{el}(\mathbf{r}, \mathbf{R}) | \psi_j(\mathbf{r}; \mathbf{R}) \rangle . \tag{2.9}$$

In the time dependent electronic Schrödinger equation, i.e.,

$$i\hbar \frac{\partial |\Psi(\mathbf{r}, \mathbf{R}, t)\rangle}{\partial t} = H_{el}(\mathbf{r}, \mathbf{R}) |\Psi(\mathbf{r}, \mathbf{R}, t)\rangle \tag{2.10}$$

by substituting Eq. (2.8) in Eq. (2.10) gives

$$i\hbar \sum_j \frac{\partial c_j(t) |\psi_j(\mathbf{r}; \mathbf{R})\rangle}{\partial t} = H_{el}(\mathbf{r}, \mathbf{R}) \sum_j c_j(t) |\psi_j(\mathbf{r}; \mathbf{R})\rangle . \tag{2.11}$$

The left-hand side (LHS) of Eq. (2.11) is expanded as

$$i\hbar \sum_j \frac{\partial c_j(t) |\psi_j(\mathbf{r}; \mathbf{R})\rangle}{\partial t} = i\hbar \sum_j \left[\frac{\partial c_j(t)}{\partial t} |\psi_j(\mathbf{r}; \mathbf{R})\rangle + c_j(t) \left| \frac{\partial \psi_j(\mathbf{r}; \mathbf{R})}{\partial t} \right\rangle \right], \tag{2.12}$$

where the time derivative of $|\psi_j(\mathbf{r}; \mathbf{R})\rangle$ is nonzero due to the parametric dependence of $\mathbf{R}$ on time. Projecting $|\psi_k(\mathbf{r}; \mathbf{R})\rangle$ onto Eq. (2.12) gives

$$i\hbar \sum_j \left\langle \psi_k(\mathbf{r}; \mathbf{R}) \left| \frac{\partial c_j(t) \psi_j(\mathbf{r}; \mathbf{R})}{\partial t} \right\rangle = i\hbar \sum_j \left[\frac{\partial c_j(t)}{\partial t} \langle \psi_k(\mathbf{r}; \mathbf{R}) | \psi_j(\mathbf{r}; \mathbf{R}) \rangle \right. \right.$$
$$\left. + c_j(t) \left\langle \psi_k(\mathbf{r}; \mathbf{R}) \left| \frac{\partial \psi_j(\mathbf{r}; \mathbf{R})}{\partial t} \right\rangle \right]. \tag{2.13}$$

The term $|\partial \psi_j(\mathbf{r}; \mathbf{R})/\partial t\rangle$ can be written as $|\nabla_{\mathbf{R}} \psi_j(\mathbf{r}; \mathbf{R})\rangle \cdot d\mathbf{R}/dt$, using the chain rule, and the orthonormality of the basis functions, Eq. (2.13) is brought to

the following form:

$$i\hbar \sum_j \left\langle \psi_k(\mathbf{r};\mathbf{R}) \middle| \frac{\partial c_j(t)\psi_j(\mathbf{r};\mathbf{R})}{\partial t} \right\rangle = i\hbar \frac{\partial c_k(t)}{\partial t}$$
$$+ i\hbar \sum_j c_j(t) \left\langle \psi_k(\mathbf{r};\mathbf{R}) \middle| \nabla_{\mathbf{R}} \psi_j(\mathbf{r};\mathbf{R}) \right\rangle \cdot \frac{d\mathbf{R}}{dt}.$$
(2.14)

The nonadiabatic coupling vector is defined as $\mathbf{d}_{kj} = \langle \psi_k(\mathbf{r};\mathbf{R}) | \nabla_{\mathbf{R}} \psi_j(\mathbf{r};\mathbf{R}) \rangle$, which denotes the interaction between electronic and nuclear DOF. Using this in Eq. (2.14) gives

$$i\hbar \sum_j \left\langle \psi_k(\mathbf{r};\mathbf{R}) \middle| \frac{\partial c_j(t)\psi_j(\mathbf{r};\mathbf{R})}{\partial t} \right\rangle = i\hbar \frac{\partial c_k(t)}{\partial t} + i\hbar \sum_j c_j(t)\mathbf{d}_{kj} \cdot \frac{d\mathbf{R}}{dt}. \quad (2.15)$$

Equation (2.15) gives the simplified version of LHS of Eq. (2.11) after projecting $|\psi_k(\mathbf{r};\mathbf{R})\rangle$ onto it. Performing a similar projection on the RHS of Eq. (2.11) gives

$$\sum_j c_j(t) \langle \psi_k(\mathbf{r};\mathbf{R})|\hat{H}_{el}(\mathbf{r},\mathbf{R})|\psi_j(\mathbf{r};\mathbf{R})\rangle = \sum_j c_j(t)E_{kj}. \quad (2.16)$$

Setting Eq. (2.15) equal to Eq. (2.16) provides the time evolution of the expansion coefficient $c_k(t)$:

$$i\hbar \frac{\partial c_k(t)}{\partial t} = \sum_j c_j(t)\left[E_{kj} - i\hbar\mathbf{d}_{kj} \cdot \frac{d\mathbf{R}}{dt}\right]. \quad (2.17)$$

For a given classical trajectory $\mathbf{R}(t)$, the coefficients $c_j(t)$ can be obtained from numerical integration of Eq. (2.17).

These equations may be rewritten in the density matrix-notation, where the density-matrix elements are defined as

$$\rho_{kj}(t) = c_k(t)c_j^*(t) \quad (2.18)$$

$$\frac{\partial \rho_{kj}(t)}{\partial t} = \frac{\partial c_k(t)}{\partial t} c_j^*(t) + c_k(t) \frac{\partial c_j^*(t)}{\partial t} \tag{2.19}$$

Using the equations of motion for the coefficients $c_j(t)$ from Eq. (2.17), we may deduce

$$i\hbar \frac{\partial \rho_{kj}(t)}{\partial t} = \sum_l \left[\rho_{lj}(t) \left(E_{kl} - i\hbar \mathbf{d}_{kl} \cdot \frac{d\mathbf{R}}{dt} \right) \right. $$
$$\left. - \rho_{kl}(t) \left(E_{jl}^* + i\hbar \mathbf{d}_{jl}^* \cdot \frac{d\mathbf{R}}{dt} \right) \right]. \tag{2.20}$$

Using the unitary of the density matrix elements, i.e., $\rho_{kl}(t) = \rho_{lk}^*(t)$, we get

$$i\hbar \frac{\partial \rho_{kj}(t)}{\partial t} = \sum_l \left[\rho_{lj}(t) \left(E_{kl} - i\hbar \mathbf{d}_{kl} \cdot \frac{d\mathbf{R}}{dt} \right) - \rho_{lk}^*(t) \left(E_{jl}^* + i\hbar \mathbf{d}_{jl}^* \cdot \frac{d\mathbf{R}}{dt} \right) \right]. \tag{2.21}$$

In Eq. (2.21), the off-diagonal term ($k \neq j$) of $\partial \rho(t)/\partial t$, denotes the rate of change of coherence between states k and j and the diagonal term ($k = j$) of $\partial \rho(t)/\partial t$, gives the rate of change of population of state k. Specifying Eq. (2.21) for $\partial \rho_{kk}(t)/\partial t$, we get

$$i\hbar \frac{\partial \rho_{kk}(t)}{\partial t} = \sum_{l \neq k} \left[\rho_{lk}(t) \left(E_{kl} - i\hbar \mathbf{d}_{kl} \cdot \frac{d\mathbf{R}}{dt} \right) - \rho_{lk}^*(t) \left(E_{kl}^* + i\hbar \mathbf{d}_{kl}^* \cdot \frac{d\mathbf{R}}{dt} \right) \right]$$
$$= \sum_{l \neq k} \left[2i \operatorname{Im}\{\rho_{lk}(t) E_{kl}\} - 2i\hbar \operatorname{Re}\left\{ \rho_{lk}(t) \mathbf{d}_{kl} \cdot \frac{d\mathbf{R}}{dt} \right\} \right] \tag{2.22}$$

and finally reduces to

$$\frac{\partial \rho_{kk}(t)}{\partial t} = \sum_{l \neq k} b_{kl}, \tag{2.23}$$

where,

$$b_{kl} = \frac{2}{\hbar} \operatorname{Im}\{\rho_{lk}(t) E_{kl}\} - 2 \operatorname{Re}\left\{ \rho_{lk}(t) \mathbf{d}_{kl} \cdot \frac{d\mathbf{R}}{dt} \right\}. \tag{2.24}$$

In the adiabatic representation (BO representation) the off-diagonal term E_{kl} vanishes and the Eq. (2.24) becomes

$$b_{kl} = -2 \operatorname{Re} \left\{ \rho_{lk}(t) \mathbf{d}_{kl} \cdot \frac{d\mathbf{R}}{dt} \right\}. \tag{2.25}$$

At this point, an expression for probability of hopping can be deduced for an ensemble of classical nuclear trajectories $\mathbf{R}(t)$. Let M be the total number of classical trajectories and $M_{kk}(t)$ be the number of trajectories in state k at time t, which is given by

$$M_k(t) = \rho_{kk}(t)M, \tag{2.26}$$

where $\rho_{kk}(t)$ gives the population of state k at time t. After an infinitesimally small amount of time, i.e., $t' = t + \Delta t$, the number of trajectories in state k is given by

$$M_k(t') = \rho_{kk}(t')M, \tag{2.27}$$

where $\rho_{kk}(t')$ gives the population of state k at time t'. Suppose, $M_k(t')$ is less than $M_k(t)$, i.e., $\Delta M = M_k(t) - M_k(t') > 0$, then ΔM trajectories should hop from state k to any other state. The probability of hopping from state k to any other state in the time interval Δt is given as

$$P_{k \to anystate} = \frac{\Delta M}{M_k(t)} = \frac{\rho_{kk}(t) - \rho_{kk}(t')}{\rho_{kk}(t)} \approx -\frac{d\rho_{kk}}{dt} \frac{\Delta t}{\rho_{kk}(t)}. \tag{2.28}$$

By substituting Eq. (2.23),

$$P_{k \to anystate} = -\frac{\sum_{l \neq k} b_{kl} \Delta t}{\rho_{kk}(t)}. \tag{2.29}$$

The probability of hopping from state k to a particular state j, i.e., $l = j$ is given by,

$$P_{k \to j} = -\frac{b_{kj} \Delta t}{\rho_{kk}(t)}, \tag{2.30}$$

where Δt is the simulation time step for nuclear trajectory. The probability of hopping is compared to an uniformly distributed random number ζ between 0 and 1, and the hop occurs only if $P_{k \to j} > \zeta$. If hopping takes place, then the velocity of the classical trajectory is adjusted in the direction of the nonadiabatic coupling vector to conserve the total energy. No hopping takes place if there is not enough energy available to adjust the velocity.

The presence of an external field denoted by a Hamiltonian given as

$$H_{ext} = -\epsilon(t) \cdot \mu, \tag{2.31}$$

where μ is the dipole operator. Following identical derivation steps, the time evolution of $c_k(t)$ in the presence of an external field is given as

$$i\hbar \frac{\partial c_k(t)}{\partial t} = \sum_j c_j(t) \left[E_{kj} - i\hbar \mathbf{d}_{kj} \cdot \frac{d\mathbf{R}}{dt} - \mu_{kj} \cdot \epsilon(t) \right], \tag{2.32}$$

where $\mu_{kj} = \langle \psi_k(\mathbf{r}; \mathbf{R}) | \mu | \psi_j(\mathbf{r}; \mathbf{R}) \rangle$. By following identical density matrix formulation and derivation steps will give

$$b_{kl} = -2 \operatorname{Re} \left\{ \rho_{lk}(t) d_{kl} \cdot \frac{d\mathbf{R}}{dt} \right\} + \frac{2}{\hbar} \operatorname{Re}\{i\rho_{lk}\epsilon(t) \cdot \mu_{kl}\}. \tag{2.33}$$

Equation (2.33) has an extra term due to the external electric field. The velocity adjustment of the trajectory after hopping is carried out if the hopping takes place due to term containing nonadiabatic coupling term (the first term) in Eq. (2.33). It is not required to adjust the velocity if the hopping takes place due to the external electric field. To decide if the hop is due to nonadiabatic

coupling term or the external electric field term, the ratio of magnitude of two terms in Eq. (2.33) is calculated and a Monte Carlo strategy is employed to sample the ratio. This is also the formulation of BO-SH mentioned in Chapter 3. The simulation was carried out by setting $\mathbf{d}_{kl} = 0$, as the influence of nonadiabatic coupling was neglected in this research work, following Ref. [22].

Using IBO surfaces E_{kj}^{IBO}, the molecular wave function may be expanded in IBO electronic basis, i.e.,

$$|\Psi(\mathbf{r}, \mathbf{R}, \epsilon, t)\rangle = \sum_j c_j(t) |\psi(\mathbf{r}; \mathbf{R}, \epsilon)\rangle . \qquad (2.34)$$

Notice that basis functions depend parametrically on both the nuclear coordinate $\mathbf{R}$ and the external electric field ϵ. The IBO energies E_{kj}^{IBO} are given by

$$E_{kj}^{IBO} = \langle \psi_k(\mathbf{r}; \mathbf{R}, \epsilon)|H_{el}(\mathbf{r}, \mathbf{R}) - \epsilon(t) \cdot \mu|\psi_j(\mathbf{r}; \mathbf{R}, \epsilon)\rangle . \qquad (2.35)$$

Substituting the above two expression in time-dependent Schrödinger equation gives

$$i\hbar \sum_j \frac{\partial c_j(t) |\psi_j(\mathbf{r}; \mathbf{R}, \epsilon)\rangle}{\partial t} = [H_{el}(\mathbf{r}, \mathbf{R}) - \epsilon(t) \cdot \mu] \sum_j c_j(t) |\psi_j(\mathbf{r}; \mathbf{R}, \epsilon)\rangle . \qquad (2.36)$$

Applying chain rule and projecting $|\psi_k(\mathbf{r}; \mathbf{R}, \epsilon)\rangle$ onto the above expression gives

$$i\hbar \frac{\partial c_k(t)}{\partial t} + i\hbar \sum_j c_j(t)\mathbf{d}_{kj} \cdot \frac{d\mathbf{R}}{dt} + i\hbar \sum_j c_j(t) \langle \psi_k(\mathbf{r}; \mathbf{R}, \epsilon)|\nabla_\epsilon \psi_j(\mathbf{r}; \mathbf{R}, \epsilon)\rangle \cdot \frac{d\epsilon}{dt}$$
$$= \sum_j c_j(t) E_{kj}^{IBO} \qquad (2.37)$$

Using, Hellmann-Feynman theorem, i.e.,

$$\nabla_\epsilon \langle \psi_k(\mathbf{r};\mathbf{R},\epsilon)|H_{el}(\mathbf{r},\mathbf{R}) - \mu \cdot \epsilon|\psi_j(\mathbf{r};\mathbf{R},\epsilon)\rangle =$$

$$\langle \nabla_\epsilon \psi_k(\mathbf{r};\mathbf{R},\epsilon)|H_{el}(\mathbf{r},\mathbf{R}) - \mu \cdot \epsilon|\psi_j(\mathbf{r};\mathbf{R},\epsilon)\rangle$$

$$+ \langle \psi_k(\mathbf{r};\mathbf{R},\epsilon)|H_{el}(\mathbf{r},\mathbf{R}) - \mu \cdot \epsilon|\nabla_\epsilon \psi_j(\mathbf{r};\mathbf{R},\epsilon)\rangle$$

$$+ \langle \psi_k(\mathbf{r};\mathbf{R},\epsilon)|\nabla_\epsilon[H_{el}(\mathbf{r},\mathbf{R}) - \mu \cdot \epsilon]|\psi_j(\mathbf{r};\mathbf{R},\epsilon)\rangle \quad (2.38)$$

$$\nabla_\epsilon E_{kj}^{IBO} = E_j^{IBO} \langle \nabla_\epsilon \psi_k(\mathbf{r};\mathbf{R},\epsilon)|\psi_j(\mathbf{r};\mathbf{R},\epsilon)\rangle$$

$$+ E_k^{IBO} \langle \psi_k(\mathbf{r};\mathbf{R},\epsilon)|\nabla_\epsilon \psi_j(\mathbf{r};\mathbf{R},\epsilon)\rangle - \langle \psi_k(\mathbf{r};\mathbf{R},\epsilon)|\mu|\psi_j(\mathbf{r};\mathbf{R},\epsilon)\rangle \quad (2.39)$$

$$\nabla_\epsilon E_{kj}^{IBO} = (E_k^{IBO} - E_j^{IBO}) \langle \psi_k(\mathbf{r};\mathbf{R},\epsilon)|\nabla_\epsilon \psi_j(\mathbf{r};\mathbf{R},\epsilon)\rangle$$

$$- \langle \psi_k(\mathbf{r};\mathbf{R},\epsilon)|\mu|\psi_j(\mathbf{r};\mathbf{R},\epsilon)\rangle \quad (2.40)$$

For $k \neq j$, in the adiabatic representation, E_{kj}^{IBO} vanishes. Therefore,

$$\langle \psi_k(\mathbf{r};\mathbf{R},\epsilon)|\nabla_\epsilon \psi_j(\mathbf{r};\mathbf{R},\epsilon)\rangle = \frac{-\mu_{kj}}{\Delta E_{jk}^{IBO}}, \quad (2.41)$$

where $\mu_{kj} = \langle \psi_k(\mathbf{r};\mathbf{R},\epsilon)|\mu|\psi_j(\mathbf{r};\mathbf{R},\epsilon)\rangle$ gives the elements of transition dipole matrix and $\Delta E_{jk}^{IBO} = E_j^{IBO} - E_k^{IBO}$. Substituting Eq. (2.41) in Eq. (2.37) gives

$$i\hbar\frac{\partial c_k(t)}{\partial t} + i\hbar\sum_j c_j(t)\left(\mathbf{d}_{kj} \cdot \frac{d\mathbf{R}}{dt} - \frac{\mu_{kj}}{\Delta E_{jk}^{IBO}} \cdot \frac{d\epsilon}{dt}\right) = \sum_j c_j(t)E_{kj}^{IBO} \quad (2.42)$$

$$i\hbar\frac{\partial c_k(t)}{\partial t} = \sum_j c_j(t)\left(E_{kj}^{IBO} - i\hbar\mathbf{d}_{kj} \cdot \frac{d\mathbf{R}}{dt} + i\hbar\frac{\mu_{kj}}{\Delta E_{jk}^{IBO}} \cdot \frac{d\epsilon}{dt}\right). \quad (2.43)$$

The above equation gives the time evolution of $c_k(t)$ in IBO-SH formalism.

Following similar steps used in the derivation of BO-SH formalism and setting $\mathbf{d}_{kj} = 0$ gives the probability of hopping $P_{k \to j}$ given in Paper 5.3.

2.3 Formulation of o-BO-SH

In the o-BO-SH method, the electronic basis is transformed using a SU(2) transformation matrix, in order to reduce the average number of hops per trajectory in BO-SH. The transformation matrix $U(\theta, \phi)$, specific to a two-state case, is given as

$$U(\theta, \phi) = \begin{bmatrix} \cos\theta & \sin\theta e^{i\phi} \\ -\sin\theta e^{-i\phi} & \cos\theta \end{bmatrix}, \tag{2.44}$$

where θ and ϕ are the parameters to be optimized for every time step to which reduce the number of hops. Subsequently, the expansion coefficients $c(t)$ are correspondingly transformed as $c^{'}(t) = U(\theta, \phi)c(t)$. The E^{BO} and $\epsilon(t) \cdot \mu$ matrix elements are transformed into $U(\theta, \phi)E^{BO}U^{\dagger}(\theta, \phi)$ and $U(\theta, \phi)\epsilon(t) \cdot \mu U^{\dagger}(\theta, \phi)$, respectively. By setting $d_{kj} = 0$ and substituting these in the BO formalism of Eq. 2.32 gives the time evolution of the expansion coefficients in the transformed basis:

$$i\hbar \frac{\partial c^{'}_k(t)}{\partial t} = \sum_j c^{'}_j(t) \Big[\sum_a U_{ka}(\theta, \phi) E^{BO}_{kj} U^{\dagger}_{aj}(\theta, \phi)$$
$$- \sum_{a,b} U_{ka}(\theta, \phi) \epsilon(t) \cdot \mu_{ab} U^{\dagger}_{bj}(\theta, \phi) - i \sum_a U_{ka(\theta,\phi)} \frac{dU^{\dagger}_{aj}(\theta, \phi)}{dt} \Big]. \tag{2.45}$$

The probability of hopping in the transformed basis, obtained by following identical steps in the BO-SH formalism, is dependent on the parameters θ and ϕ, i.e., $P_{k \to j}$ is a function of (θ, ϕ). Note that k and j denotes the transformed PES. Optimizing $P_{k \to j}(\theta, \phi)$ with respect to θ and ϕ give the optimum values of $(\theta_{\text{opt}}, \phi_{\text{opt}})$. The optimized PESs are obtained using θ_{opt} and ϕ_{opt}, i.e.,

$E^{\mathrm{o}} = U(\theta_{\mathrm{opt}}, \phi_{\mathrm{opt}})E^{BO}U^{\dagger}(\theta_{\mathrm{opt}}, \phi_{\mathrm{opt}})$ and the classical trajectories are allowed to evolve on them.

For the case considered in Paper 5.3, its observed that the optimization leads to an approach very similar to Ehrenfest approach. However, the Ehrenfest approach has its own drawbacks and a smooth switch between the BO-SH and Ehrenfest-like o-BO-SH approach is discussed in Paper 5.3.

Chapter 3

Research summary

In the presence of an external electric field, inner-shell photoionization followed by Auger decay gives rise to numerous interesting phenomena. In this chapter, a brief summary of research work, from papers 5.1, 5.2 and 5.3, to investigate such processes in the presence of an external field is presented.

The basic underlying process behind inner-shell photoionization followed by Auger decay is presented in Fig. 3.1. Inner-shell photoionization is the process in which an inner-shell electron is removed from the parent ion using a high-energy external field. The electron-electron interaction and electron-hole interaction [23] in this process pave the way for many-body effects to occur, such as interchannel coupling [24, 25], core relaxation [26, 27, 28], core polarization [29], autoionization resonances [30], photoionization-with-excitation [31], double photoionization [32, 33, 34, 35], Auger decay [36, 37, 38, 39], and post-collision interaction [40].

Auger decay is the process whereby an excited ion with an inner-shell hole (from a previous inner-shell ionization process) relaxes to a lower energy state by ejecting an electron (referred to as the Auger electron). In turn, a valence electron will fill the core-hole, resulting in the residual atom containing two valence holes. The kinetic energy (KE) of the ejected Auger electron does not depend on the energy of incoming photon and is an intrinsic property of electronic structure of the parent system. Thus, the measurement of properties of Auger electrons is an excellent probe for the elemental and

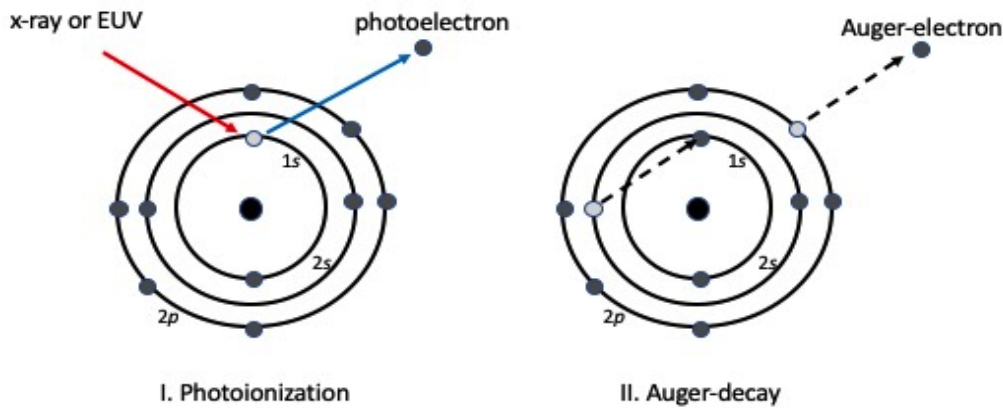chemical characteristics of the parent system [41]. This is the underlying process behind Auger spectroscopy.

FIGURE 3.1: A schematic diagram explaining the basic underlying process behind inner-shell photoionization (I) followed by Auger decay (II).

3.1 Laser-field-induced quantum interference in Auger decay

The emitted Auger and photoelectrons can be probed or controlled using intense and highly energetic laser fields [42, 43, 44, 45, 46]. The advances in technologies to use intense infra-red (IR) laser-fields [in Tera Hertz (THz) energy regime] synchronized with extreme ultra-violet (EUV) or x-ray pulses allow for the investigation of the laser-assisted Auger decay in THz regime.

In an experiment, performed by Roman Brannath and Markus Drescher (co-authors of Paper 5.1), magnesium (Mg) atoms are irradiated by ultrashort EUV pulses, which form a $2p$ core-hole by emitting photoelectrons. Due to spin-orbit coupling, the $2p^5 3s^2$ energy level of Mg^+ ion is split and thus the decay of core-hole states happens in two distinct Auger pathways, resulting in two distinct peaks in Auger spectrum. Later, the same experiment is performed in the presence of the THz pulses. The Mg atoms are irradiated

by ultrashort EUV pulses synchronized with THz pulses and an oscillatory structure reminiscent of an interference pattern was observed in the electron KE spectrum, thus concluding that an interference between relaxation pathways may be induced by the presence of a THz field.

An analytical model, based on time-dependent perturbation theory, was developed by Murali Krishna Ganesa Subramanian, Ralph Welsch and Robin Santra (authors of Paper 5.1) to provide a physical picture for the interference pattern observed in the above experiment. The theoretical formulation of the model is explained in detail in the appendix section of Paper 5.1. In this analytical model, the photoionization and Auger decay processes are treated in the perturbation framework. The THz field is too strong and so its interaction is treated in a nonperturbative fashion. To observe interference between two Auger pathways, the combined quantum states of Auger electrons, photoelectrons and Mg dication should be indistinguishable. Within the analytical model, it is demonstrated that the THz field streaks the system to evolve into indistinguishable quantum states which gives rise to interference pattern observed in the experiment.

3.2 Auger-decay followed by laser-field-induced fragmentation of N_2^{2+}

The field-induced fragmentation of molecules is very well studied in the AMO community [47, 48, 49, 50, 51]. Pump-probe spectroscopy gives the possibility to investigate the fragmentation dynamics in detail. In this technique, an ultrashort laser pulse is split into two parts; a pump pulse to initiate the excitation and a probe to monitor the pump-induced changes and the subsequent processes.

In a pump-probe experiment performed at LCLS, SLAC National Laboratory, using FEL [52], N_2^{2+} is produced from N_2 following an inner-shell photoionization event from the x ray, followed in turn by Auger decay. A decrease in unfragmented-N_2^{2+} as a function of time delay between the pump x-ray pulse and the probe IR pulse has been reported.

Using quantum-dynamics (QD) simulations [53], the interaction between an IR pulse and N_2 dication as a function of time delay, similar to the experiment performed, was investigated in detail. The results from the simulations were in very good agreement with the experiment. In addition to that, a direct dependence of unfragmented-N_2^{2+} on intensity and width of the IR pulse was observed. The simulation is computationally expensive and scales exponentially with increasing system size, illustrating the need for a MQC theoretical description.

To improve on this computational cost, a MQC method of the field-induced Tully's fewest switches surface hopping (FSSH) algorithm was employed using a quasidiabatic representation of N_2^{2+} states in Paper 5.2 to investigate the fragmentation of the N_2 dication. The theoretical framework of the employed algorithm is discussed in Chapter 2. In the MQC method, the electrons are treated quantum mechanically and the nuclei are treated classically, which greatly reduces the computational cost. Results from the FSSH simulations are found to be in good agreement with QD simulations. The computational simplicity of FSSH allows to investigate the same process in the adiabatic representation of N_2^{2+} states using more potential energy surfaces (PES). Slightly different fragmentation dynamics is reported in the adiabatic representation.

3.3 Further study of field-induced FSSH variants

Due to its computational efficiency, field-induced FSSH simulations is a widely used tool in molecular dynamics. The PESs in field-induced FSSH are optically coupled via the transition dipole moment. The transition dipole moment is nothing but the electric dipole moment associated with the transition between two states. These basic states used in field-induced FSSH can be field-free surfaces, adiabatic Born-Oppenheimer (BO) surfaces and instantaneous BO (IBO) surfaces which are the eigenstates of electronic Hamiltonian including electric field at that instant of time. Subsequently, the field-induced FSSH using BO and IBO surfaces are termed as BO-SH and IBO-SH, respectively. Theoretical formulation of BO- and IBO-SH are given in Chapter 4.

It has been shown that BO- and IBO-SH gives non-physical results compared to full quantum simulations for photoexcitation and stimulated emission processes in an exactly solvable H_2^+ model [22]. It is reported that non-physically high average number of hops per trajectory leads to this drawback. This was overcame by employing another field-induced FSSH variant using Floquet PES within FSSH framework; i.e., Floquet FSSH (F-SH) and found to be in good agreement with quantum simulations. However, Floquet picture has its own limitations as it is exact only for periodic continuous wave lasers.

In Paper 5.3, a version of field-induced FSSH termed as optimised-BO-SH (o-BO-SH) is proposed which minimizes the non-physical average number of hops compared to BO- and IBO-SH. The o-BO-SH is an Ehrenfest-like field-induced FSSH approach. In Ehrenfest dynamics, the nuclei is allowed to evolve using classical equations of motion, due to the force from the superposition of electronic eigenstates. In case of two level system, the system will experience force from the superposition of two states. If the nature of

the states are very distinct then the corresponding force could lead to non-physical results. In o-BO-SH, a smooth combination of Ehrenfest-like approach in strongly coupled region and BO-SH in weakly coupled region, the average number of hops is greatly reduced in the scenarios mentioned in Ref. [22]. The results from o-BO-SH simulations performs well compared to the full quantum simulations.

Chapter 4

Conclusion

This thesis is dedicated to inner-shell processes in the presence of an external electric field. It presents the possibility of using time-dependent perturbation theory and MQC to investigate various distinct field-induced inner-shell processes.

In Sec. 3.1, an overview of theoretical interpretation from paper 5.1, based on time-dependent perturbation theory, is provided to investigate the quantum interference in Auger decay of Mg atoms found in experiment. It demonstrates the possibility of inducing quantum interference using THz streaking process in multi-channel electronic decay pathways following inner-shell photoionization (see paper 5.1).

In Sec. 3.2, an overview of MQC scheme based on FSSH method from paper 5.2 to simulate the fragmentation dynamics of N_2^{2+} is shown. Results from the simulation are found to be in good agreement with the QD simulations and also computationally cheaper than the QD simulations (please see paper 5.2). This aspect will allow for the investigation of field-induced dynamics in more complex and bigger molecular systems. In Sec. 3.3, a variant of field-induced FSSH for a two level system from paper 5.3, o-BO-SH, is proposed which reduces the non-physical hopping between PESs in presence of an electric field. In the future, the proposed method can be extended to systems with more than two levels.

The MQC simulations can be further improved using machine learning

(ML) techniques [54]. With the help of ML techniques, the parameters such as the force experienced by the classical trajectory, can be predicted by predicting the PES. This will further reduce the computational cost.

Bibliography

[1] L. Hamonou, H. Hart, *Journal of Physics: Conference Series* **194** (2009).

[2] J. Hecht, *Optical Engineering* **49**, 1 (2010).

[3] N. R. Council, *Atomic, Molecular, and Optical Science: An Investment in the Future* (The National Academies Press, Washington, DC, 1994).

[4] E. M. Purcell, R. V. Pound, *Phys. Rev.* **81**, 279 (1951).

[5] J. P. Gordon, H. J. Zeiger, C. H. Townes, *Phys. Rev.* **95**, 282 (1954).

[6] A. L. Schawlow, C. H. Townes, *Phys. Rev.* **112**, 1940 (1958).

[7] A. Javan, *Phys. Rev. Lett.* **3**, 87 (1959).

[8] F. Schumann, J. Kirschner, *Journal of Electron Spectroscopy and Related Phenomena* **241**, 146943 (2020). Sources, Interaction with Matter, Detection and Analysis of Low Energy Electrons (SIMDALEE2).

[9] M. F. Kling, M. J. Vrakking, *Annual Review of Physical Chemistry* **59**, 463 (2008). PMID: 18031218.

[10] F. Calegari, *et al.*, *Science* **346**, 336 (2014).

[11] F. Krausz, M. Ivanov, *Rev. Mod. Phys.* **81**, 163 (2009).

[12] T. S. Rose, M. J. Rosker, A. H. Zewail, *The Journal of Chemical Physics* **88**, 6672 (1988).

[13] L. Windhorn, *et al.*, *Chemical Physics Letters* **357**, 85 (2002).

[14] A. Naves de Brito, *et al.*, *Chemical Physics Letters* **309**, 377 (1999).

[15] P. Q. Wang, *et al.*, *Phys. Rev. A* **74**, 043411 (2006).

[16] O. Geßner, *et al.*, *Science* **311**, 219 (2006).

[17] M. Maroncelli, G. R. Fleming, *The Journal of Chemical Physics* **86**, 6221 (1987).

[18] M. Lee, *et al.*, *The Journal of Chemical Physics* **85**, 4341 (1986).

[19] X. Wu, *et al.*, *Science Advances* **3** (2017).

[20] H. Zhang, K. Li, J. Yan, H. Deng, B. Sun, *Phys. Rev. Accel. Beams* **21**, 070701 (2018).

[21] L. Young, *et al.*, *Journal of Physics B: Atomic, Molecular and Optical Physics* **51**, 032003 (2018).

[22] T. Fiedlschuster, J. Handt, E. K. U. Gross, R. Schmidt, *Phys. Rev. A* **95**, 063424 (2017).

[23] M. Kutzner, *Radiation Physics and Chemistry* **70**, 95 (2004). Photoeffect: Theory and Experiment.

[24] P. Deshmukh, *Radiation Physics and Chemistry* **70**, 515 (2004). Indo-US Workshop on Radiation Physics with Synchrotrons and Other New Sources.

[25] W. Drube, *et al.*, *Journal of Physics B Atomic Molecular Physics* **46**, 5006 (2013).

[26] B. Gumhalter, *Phys. Rev. B* **19**, 2018 (1979).

[27] D. L. Lynch, V. McKoy, *Phys. Rev. A* **30**, 1561 (1984).

[28] G. B. Bachelet, N. E. Christensen, *Phys. Rev. B* **31**, 879 (1985).

[29] W. Müller, J. Flesch, W. Meyer, *The Journal of Chemical Physics* **80**, 3297 (1984).

[30] S. L. Sorensen, *et al.*, *Phys. Rev. A* **50**, 1218 (1994).

[31] A. S. Kheifets, I. Bray, *Phys. Rev. A* **58**, 4501 (1998).

[32] D. Akoury, *et al.*, *Science* **318**, 949 (2007).

[33] A. Huetz, P. Selles, D. Waymel, J. Mazeau, *Journal of Physics B: Atomic, Molecular and Optical Physics* **24**, 1917 (1991).

[34] J. A. R. Samson, *et al.*, *Phys. Rev. A* **57**, 1906 (1998).

[35] O. Schwarzkopf, B. Krässig, J. Elmiger, V. Schmidt, *Phys. Rev. Lett.* **70**, 3008 (1993).

[36] M. L. Knotek, P. J. Feibelman, *Phys. Rev. Lett.* **40**, 964 (1978).

[37] J. M. Schins, *et al.*, *Phys. Rev. Lett.* **73**, 2180 (1994).

[38] F. Trinter, *et al.*, *Nature* **505**, 664 (2014).

[39] F. Penent, *et al.*, *Phys. Rev. Lett.* **95**, 083002 (2005).

[40] P. van der Straten, R. Morgenstern, A. Niehaus, *Zeitschrift für Physik D Atoms, Molecules and Clusters* **8**, 35 (1988).

[41] H. H. Madden, *Journal of Vacuum Science and Technology* **18**, 677 (1981).

[42] R. Kanya, Y. Morimoto, K. Yamanouchi, *Phys. Rev. Lett.* **105**, 123202 (2010).

[43] L. Miaja-Avila, *et al.*, *Phys. Rev. Lett.* **97**, 113604 (2006).

[44] L. B. Madsen, *American Journal of Physics* **73**, 57 (2005).

[45] B. Cooper, V. Averbukh, *Phys. Rev. Lett.* **111**, 083004 (2013).

[46] P. Ranitovic, *et al.*, *Phys. Rev. Lett.* **106**, 053002 (2011).

[47] E. Itälä, K. Kooser, E. Rachlew, M. A. Huels, E. Kukk, *The Journal of Chemical Physics* **140**, 234305 (2014).

[48] B. Gaire, *et al.*, *Physical Review. A* **92** (2015).

[49] N. Berrah, *et al.*, *Journal of Electron Spectroscopy and Related Phenomena* **196**, 34 (2014). Advances in Vacuum Ultraviolet and X-ray Physics, The 38th International Conference on Vacuum Ultraviolet and X-ray Physics (VUVX2013), University of Science and Technology of China.

[50] D. Koulentianos, *et al.*, *Journal of Physics B: Atomic, Molecular and Optical Physics* **53**, 244005 (2020).

[51] E. T. Karamatskos, *et al.*, *Faraday Discuss.* pp. – (2021).

[52] J. M. Glownia, *et al.*, *Opt. Express* **18**, 17620 (2010).

[53] A. M. Hanna, O. Vendrell, A. Ourmazd, R. Santra, *Phys. Rev. A* **95**, 043419 (2017).

[54] J. Westermayr, P. Marquetand, *Machine Learning: Science and Technology* **1**, 043001 (2020).

Chapter 5

Publications

5.1 Field-enabled quantum interference in atomic Auger decay

Murali Krishna Ganesa Subramanian, Roman Brannath, Ralph Welsch, Robin Santra and MarKus Drescher

Statement of contribution

The theoretical concept was developed by Robin Santra. The experiment and writing the corresponding experimental part of the manuscript was done by Roman Brannath and Markus Drescher. And, the analytical calculations along with writing the theory part of the manuscript including appendix are done by myself, Robin Santra and Ralph Welsch.

Field-enabled quantum interference in atomic Auger decay

Murali Krishna Ganesa Subramanian [1,2] Roman Brannath,[2] Ralph Welsch [1] Robin Santra [1,2] and Markus Drescher [2]
[1]*Center for Free-Electron Laser Science, Deutsches Elektronen-Synchrotron DESY, 22607 Hamburg, Germany*
[2]*Department of Physics, Universität Hamburg, 22761 Hamburg, Germany*

We demonstrate that an external terahertz (THz) field enables the formation of interference between two distinct Auger pathways leading to the same final ionic state. The kinetic energy of Auger electrons ejected from either of two spin-orbit split one-hole states of magnesium cations is recorded. In the presence of the THz field, a clear oscillatory structure in the Auger spectrum emerges, which we find to be in very good agreement with an analytical model based on perturbation theory. For this interference to occur, the THz field has to chirp the energy of both Auger electrons and photoelectrons simultaneously, in order to create states with indistinguishable quantum properties.

I. INTRODUCTION

X-ray-induced innershell processes like photoionization of core electrons, Auger decay, or x-ray fluorescence are widespread tools to probe structural changes in atoms, molecules, and solids with element specificity [1,2]. Advances in x-ray light sources such as x-ray free-electron lasers and table-top sources using high harmonic generation make it possible to tackle problems at the forefront of science using ultrafast x-ray techniques that can achieve atomic spatial resolution and femtosecond time resolution [3]. In this context, external fields have been used to modify or control x-ray-induced innershell processes to obtain a more detailed picture of the investigated processes and to allow for new applications. For example, x-ray diffraction can be optically modulated allowing for the investigation of optically induced charges [4], innershell photoabsorption can be controlled by nonperturbative modification of the level structure of the bound electrons [5,6] or by laser-induced molecular alignment [7,8], line profiles of photoabsorption can be modified [9,10], and the streaking of ejected photoelectrons with near- or far-infrared light or the observation of circular dichroism is a useful tool in characterizing x-ray pulses [11–13].

A particularly interesting probe of the electronic structure of matter is based on the Auger effect, i.e., the nonradiative decay of a deeply bound core hole through the emission of an Auger electron. The recorded kinetic energy of the Auger electrons is an intrinsic property of the electronic structure of the target and does not depend on the energy of the incoming light. Therefore, Auger spectroscopy is an important and widely used probe of the electronic structure of atoms, molecules, and surfaces. The emission of Auger electrons and photoelectrons can be further probed or controlled by intense laser fields, e.g., in the infrared (IR) energy range. In such laser-assisted processes, the system is irradiated by an extreme-ultraviolet (EUV) or x-ray pulse, which creates a core hole and a photoelectron. The core hole can decay nonradiatively and an Auger electron is emitted. The emitted electrons are subsequently dressed by the applied intense laser field.

This leads, e.g., to the appearance of several side bands or to a continuous shift of the spectrum. Laser-assisted photoelectric effect [14–19], laser-assisted Auger decay [20,21], and laser-enabled Auger decay [22–24] have been observed. Recent technological advances allow for the creation of intense laser fields in the far-IR [or terahertz (THz)] energy range, which can be well synchronized with EUV or x-ray pulses [25,26]. This enables the study of laser-assisted Auger decay also in the THz regime [27].

Notably, if the final state can be reached via different quantum pathways, interference may occur. Various mechanisms underlying such interference in atomic or molecular systems have been identified. Upon scanning the energy of the photoelectron across the fixed energy of the Auger electron, both electrons can be made indistinguishable, thus creating interference in their spectra and angular distributions [28]. Also different resonant Auger transitions may accidentally have significant spectral overlap, thus giving rise to interference [29,30]. Spectral separation between Auger electrons may be partially bridged by postcollision interaction, predicted already in 1977 [31], but experimentally verified only in 2001 [32]. Molecular targets introduce additional channels, e.g., via lifetime-vibrational interference [33,34], where energetic degeneracy of electronic states is reached through nuclear motion.

All of these cases rely on a specific intrinsic electronic structure, whereas in the present work we demonstrate how interference is enabled through external control. Under conditions found in atomic magnesium used as an example, a time-varying light field can chirp the energy of Auger electrons and photoelectrons emitted from a spin-orbit split state so as to induce interference between two distinct Auger pathways that natively form two separate spectral peaks.

II. EXPERIMENT

In the experiment, an initial $2p$ core hole is formed in Mg atoms by photoionization using ultrashort EUV pulses at 91 eV of photon energy, generated as high harmonics of
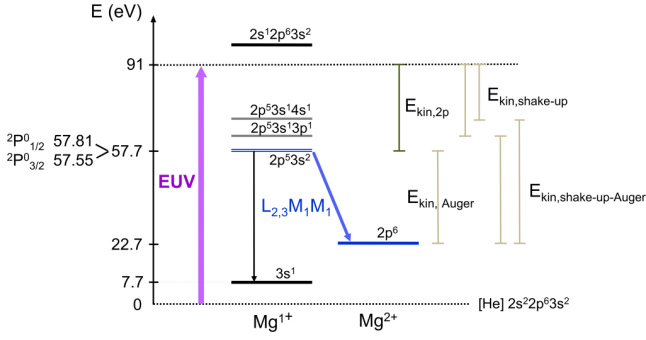
FIG. 1. Energy level diagram of Mg and its cations. Nonresonant excitation leads to core-excited states that relax upon emission of *LMM* Auger electrons. The excess kinetic energy of emitted photoelectrons and Auger electrons is indicated by vertical bars.
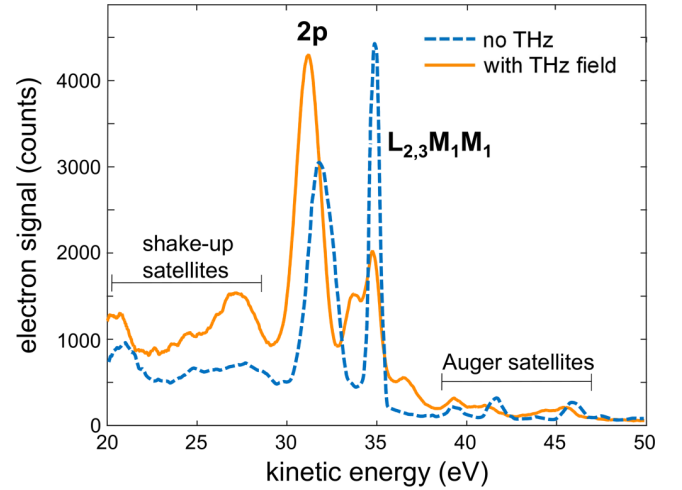

FIG. 2. Electron kinetic energy spectrum of atomic Mg after excitation at 91 eV of photon energy without (dashed blue line) and with (solid orange line) applied THz field.

800-nm, 38-fs, 2-mJ pulses from a 1-kHz Ti:sapphire laser system in a neon-gas target after compression of the fundamental pulses in a neon-filled hollow fiber [35]. Near-infrared pulses of 1 mJ of energy from the same laser are used to generate THz radiation by optical rectification in a LiNbO$_3$ crystal. Phase-matching between near- and far-infrared light fields by pulse-front tilting [36] yields 0.5-μJ single-cycle THz pulses centered at 0.6 THz. After temporal synchronization with a tunable optical delay line, EUV and THz pulses are focused into an effusive beam of Mg atoms formed a few millimeters above the orifice of a metal oven operated at up to 700 °C. The ejected photoelectrons and Auger electrons are collected in an approximately 20° solid angle perpendicular to the light propagation and guided into a time-of-flight spectrometer. Owing to an alignment of the spectrometer axis with the polarization of the THz beam, the escaping electrons are energetically streaked according to the phase of the THz vector potential at the instant of emission [25].

Figure 1 depicts the relevant energy levels of atomic magnesium. At 91 eV of photon energy, a 2p core electron is promoted into the ionization continuum. The $2p^53s^2$ level of Mg$^+$ is spin-orbit split by 0.28 eV and thus the decay of the intermediate hole states creates Auger electrons at 34.87 and 35.15 eV, respectively. The corresponding Auger lifetimes deduced from the literature vary considerably between a lower bound of about 20 fs, resulting from spectral linewidth measurements [37,38], and 500 fs predicted theoretically [31]. Regardless of their actual resolution in the experiment, natively emitted Auger electrons from Mg$^+$ ions form distinct peaks in the recorded kinetic energy spectrum and will thus not be able to interfere.

Figure 2 presents the unperturbed and the THz-streaked kinetic energy spectra of the ejected electrons. The unperturbed spectrum clearly shows the photoelectron peak around 32.5 eV and the Auger peak around 35 eV. Please note that with the given spectral resolution of the utilized time-of-flight spectrometer of >0.3 eV the fine structure of the *LMM* Auger feature, i.e., the two distinct Auger pathways under consideration, cannot be resolved in the unperturbed spectrum. The width of the 2p photoline is governed by the bandwidth of the exciting radiation, dictated by the 2-eV bandpass of the EUV multilayer mirror used for harmonic selection. The

application of the THz field significantly alters the Auger spectrum when the relative timing with respect to the EUV pulse corresponds to a steep slope of the THz vector potential while the electron wave packet is formed in the continuum. Rather than a plain broadening expected for regular streaking, the spectrum displays a clear oscillatory structure reminiscent of an interference pattern.

III. THEORY

To investigate whether and in what form the oscillatory structure in the spectrum results from quantum interference, we employ an analytical model based on time-dependent perturbation theory. In the present approach, the interaction of Mg atoms with the EUV pulse as well as the Auger decay are treated perturbatively. The strong THz field, however, is treated in a nonperturbative fashion. Within this model (for details of the derivation, see Appendices A and B) the probability of finding the Auger electron in state α is given as

$$
P_\alpha = \lim_{t \to \infty} \sum_{\substack{\gamma > \beta \\ \Pi(\Pi < \alpha)}} \left| \sum_{a''} \sum_{\substack{j \\ a}} \int_{-\infty}^{t} dt' \right.
$$
$$
\times \int_{-\infty}^{t'} dt'' u_{\alpha a''}(t,t') e^{-iI_{\beta\gamma}(t-t')}
$$
$$
\left. \times v_{a''j\beta\gamma} u_{\Pi a}(t,t'') \, e^{-i(I_j - i\frac{\Gamma_j}{2})(t'-t'')} \, \varepsilon_{\text{EUV}}(t'') \, z_{aj} \right|^2, \quad (1)
$$

where the t'' integral corresponds to photoionization and the t' integral corresponds to Auger decay, with $t' > t''$. The one-body matrix element z_{aj} determines the creation of a hole at time t'', in which j corresponds to the state of the hole and a corresponds to the state of the emitted photoelectron, with ionization energy $I_j = -\epsilon_j$. The photoionizing EUV pulse has
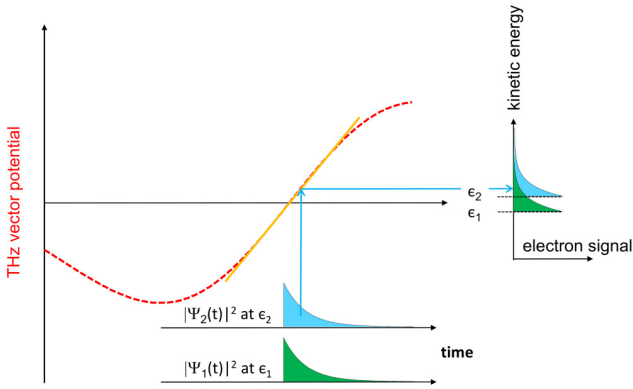
FIG. 3. Principle of field-enabled interference of Auger pathways of different initial Auger energies ϵ_1 and ϵ_2. The vector potential of the THz field (dashed curve) imprints the same gradual change (almost linear chirp) of the instantaneous frequency onto both wave packets, thus creating partial energetic degeneracy that may lead to interference, if they carry a defined phase relationship.

an electric field of $\varepsilon_{\text{EUV}}(t'')$. The term $\Gamma_j = 1/\tau_j$ corresponds to the decay rate of the hole in state j. The emitted photoelectron evolves from state a at time t'' to state Π at time t under the influence of the THz field, which is described by the term $u_{\Pi a}(t, t'')$. The two-body matrix element $v_{a''j\beta\gamma}$ determines the Auger-decay step. The initially created state with a hole in j decays to a state with a hole in γ and a simultaneously emitted Auger electron emitted from β into state a''. Now, the emitted Auger electron evolves under the influence of the THz field from state a'' at time t' to state α at final time t, which is captured by $u_{\alpha a''}(t, t')$. The different dicationic states described by the two holes in β and γ and the state of the photoelectron Π contribute incoherently to the signal. Please note that a full *ab initio* simulation of the process is not feasible as, e.g., both the photoelectron and the Auger electron are unbound and prohibitively large spatial grids are required to simulate the unbound motion of two electrons ejected from an atom.

To observe interference between the two Auger pathways discussed above, the whole system has to evolve into the same indistinguishable final states, i.e., the combined quantum states of the Auger electron, the photoelectron, and the dication have to be indistinguishable. For the dication, this is fulfilled here as both Auger pathways lead to the same final state. Therefore, to observe interference, the applied THz field has to modify both the photoelectron and the Auger electron. Since the large bandwidth of the EUV radiation blurs any substructure in the $2p$ photoelectron peaks, we focus the detailed discussion of the streaking process on the Auger electrons. First, the THz pulse has to streak the energy of the emitted Auger electron from the $j_1 = 3/2$ and $j_2 = 1/2$ photoionization channels to overlap their energies. This can be understood by describing the emitted Auger electron in terms of partial waves with energies ϵ_1 and ϵ_2, but with the same temporal profile, i.e., an exponentially decaying transition probability (see Fig. 3). The exposure of these electron partial waves to a time-varying THz field, which has a period greater than the Auger lifetime, results in time-dependent momentum transfer from the THz field to the Auger electron.

In the experimental setup used in this work, the detection of the emitted electrons is restricted to a small subset of emission angles. This detection scheme does not allow for the detection of the different angular momentum states of the emitted electrons. If, however, a similar experiment were performed with a detection of electrons at all emission angles, one would have to take into account the distinct angular momenta of the Auger electrons. The spin-orbit split one-hole states under consideration have a total angular momentum of $j = 1/2$ and $j = 3/2$, respectively. As the final state of Mg^{2+}, which is the same for both pathways, has an angular momentum of $j = 0$, and the total angular momentum has to be conserved, the emitted Auger electrons have an angular momentum of $j = 1/2$ and $j = 3/2$, respectively. Therefore, to observe interference in such a case, the emitted Auger electrons should be indistinguishable in terms of all quantum numbers, and therefore, the perturbing THz field has to chirp the energy of the Auger electrons as well as modify their angular momentum.

Making a short-pulse approximation, i.e., assuming the EUV pulse to be a δ pulse, and taking the effect of the THz field into account through a linear frequency chirp, i.e., a quadratic temporal phase $e^{-ibt'^2}$, we can define the transition amplitudes (for details, see Appendix B)

$$
\Psi_{\alpha\beta\gamma\Pi}(t'; t_{\text{EUV}})
$$
$$
= \begin{cases} \sum_j A_{j\alpha\beta\gamma\Pi} e^{-i(I_j - i\frac{\Gamma_j}{2} - I_{\beta\gamma})t'} e^{-ib(t' + t_{\text{EUV}})^2}, & t' \geqslant 0, \\ 0, & t' < 0, \end{cases}
$$
(2)

and rewrite the spectrum given in Eq. (1) as a Fourier transform of these transition amplitudes:

$$
P_\alpha = \sum_{\substack{\gamma > \beta \\ \Pi(\Pi < \alpha)}} \left| \int_{-\infty}^{\infty} dt' \, \Psi_{\alpha\beta\gamma\Pi}(t'; t_{\text{EUV}}) e^{i\varepsilon_\alpha t'} \right|^2.
$$
(3)

The parameter t_{EUV} represents the time at which the EUV pulse is centered, relative to the temporal evolution of the THz field.

IV. ANALYSIS

In order to fit the experimental Auger spectral shape, we exploit that there is only a single Auger channel in the present problem and that the complex expansion coefficients $A_{j\alpha\beta\gamma\Pi}$ cannot change much over the narrow range of photoelectron (Π) and Auger-electron (α) states considered. Hence, we write the Auger spectrum in the simplified form

$$
P_\alpha = \text{const.} \left| \sum_j A_j e^{-i\phi_j} \int_0^{\infty} dt' \, e^{-i(E_j - i\frac{\Gamma_j}{2} - \varepsilon_\alpha)t'} e^{-ib(t' + t_{\text{EUV}})^2} \right|^2,
$$
(4)

where $E_{3/2} = \epsilon_1 = 57.55$ eV and $E_{1/2} = \epsilon_2 = 57.81$ eV (cf. Fig. 1). In what follows, the phase difference $\Delta = \phi_{3/2} - \phi_{1/2}$, the electronic chirp parameter b, and the Auger lifetime τ, which is assumed to be the same for both pathways ($\tau = \tau_{3/2} = \tau_{1/2}$), serve as fit parameters. The branching ratio, i.e.,
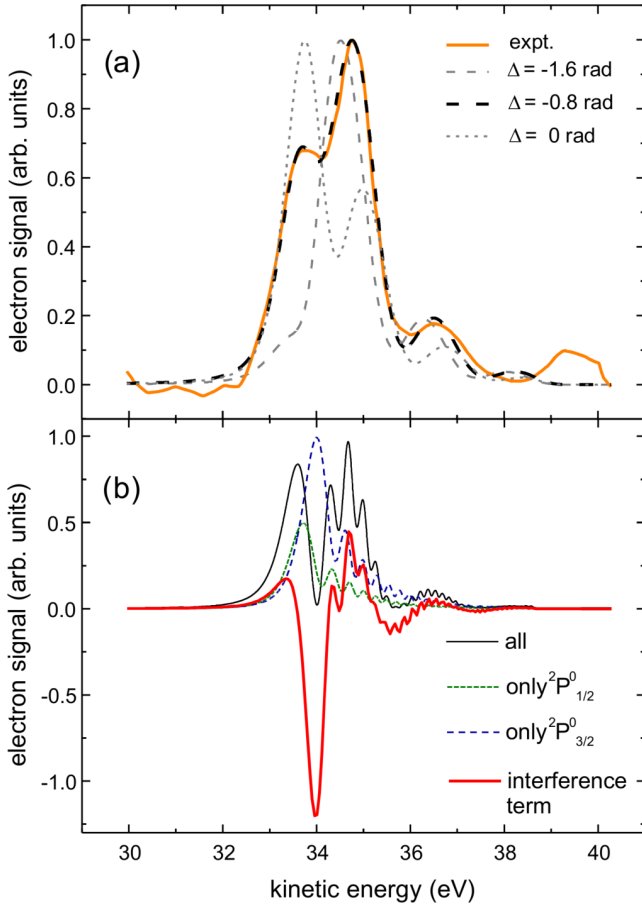
FIG. 4. (a) Experimental spectrum of streaked Mg *LMM* Auger lines (solid orange line) and simulation with the analytical model (dashed black line) with optimized parameters and with different values for the phase (gray, long dashed and short dashed lines). (b) The simulated spectrum is plotted for a δ-pulse excitation (thin black), together with the two isolated Auger fine-structure components assuming no interference (long-dashed blue line and short-dashed green line). The interference term is shown as a thick red line.

$(A_{3/2}/A_{1/2})^2$, is set to 2, as given by the relative weight of the magnetic substates [37].

To obtain a meaningful comparison with experimental data, the spectrum obtained from Eq. (4) is convolved with a Gaussian shape capturing the broadening effects of a finite spectrometer resolution of 0.3 eV and a finite duration of the EUV pulse. The resulting function is then fit to the experimental spectrum. Due to a residual detuning of the EUV-THz delay relative to the zero crossing of the THz vector potential, a small energy shift is added to the simulated spectrum.

The resulting best t, displayed in Fig. 4(a), is achieved for a phase difference Δ of -0.8 ± 0.6 rad, an Auger lifetime of $\tau = 9.0$ (+5.2/−3.8) fs, and an electronic chirp of $b = 119$ meV/fs, with the indicated errors resulting from a doubling of the residual between measured and simulated values. The combined spectral broadening of 0.6 eV is compatible with an EUV pulse duration below 5 fs. The mutual relationship of the fitting parameters reveals a pronounced sensitivity of the observed spectral profile to the phase Δ between the

electronic pathways of the two fine-structure components. This is exemplified in Fig. 4(a) by simulated spectra with the same set of parameters except phase differences set to $\Delta = 0$ rad and $\Delta = -1.6$ rad, respectively. The analytical model reproduces the experimental spectrum very well, which suggests that it captures the key features of the process.

In Fig. 4(b), the Gaussian convolution has been removed from the fitted spectrum P_α in order to further analyze the interference pattern. The full spectrum is decomposed into the two fine-structure components and the corresponding interference term. The sum over j in Eq. (4) has two terms and we can thus expand it as

$$P_\alpha = \{|z_1|^2 + |z_2|^2 + 2\mathcal{R}(z_1 z_2^*)\}. \quad (5)$$

The first two terms describe the two fine-structure components [blue and green lines in Fig. 4(b)], while the last term corresponds to the interference between the two Auger pathways [red line in Fig. 4(b)]. The total spectrum shows a clear, slowly oscillating interference pattern rather than two distinct Auger peaks. The superposition of the two electronic pathways results in a temporal beating at a time period $T = 2\pi/(\epsilon_2 - \epsilon_1)$. Due to the streaking, this period is mapped to a difference in kinetic energy of $\delta E_{kin} = b\hbar T$. For the best-fit parameters this results in a kinetic energy difference of about 1.7 eV, which roughly matches the peak separation in Fig. 4. Moreover, the simulated spectrum now shows a noticeable, high-frequency oscillation pattern in the fine-structure components as well as in the interference term, which can be interpreted as fringes in the spectral domain resulting from the short-pulse approximation for the photoionization step. The rapid oscillations are suppressed if the spectrum is convolved as in Fig. 4(a).

V. CONCLUSION

In this paper, we have demonstrated that it is possible to create interference between two distinct Auger pathways by applying an intense THz field. Specifically, photoionization of Mg by an EUV pulse creates a hole in the $2p$ shell. Thus, Mg$^+$ is prepared in either of two spin-orbit split one-hole states, which both decay to the same Mg^{2+} state by ejecting an Auger electron. When applying a THz field, we observed in the Auger spectrum interference between the associated electronic pathways. For this effect to manifest, not only the Auger-electron final states must be indistinguishable but also the same indistinguishability requirement applies to the photoelectron final states.

We interpreted the experimental spectrum by fitting an analytical model based on a perturbative expansion. By separating the model spectrum into its components, the importance of interference in explaining the experimentally observed spectral oscillations was clearly revealed. The analytical model agreed with the experimental data only if a significant nonvanishing phase difference between the interfering Auger pathways was taken into account. With the shape of the spectral peak being found to sensitively depend on the exact phase value, our method provides phase information from innershell processes that is difficult to obtain otherwise. We note, however, that this phase may contain contributions from the interaction of the outgoing electrons with the external THz field. Future work will focus on the isolation of intrinsic phases.

Owing to the pronounced interference profile, the Mg$^+$ Auger-decay lifetime could be extracted and was found to be at the lower bound of available predictions. In contrast to the examples of control given in the Introduction, the present approach shows how THz streaking may be employed to induce quantum interference in the electronic-decay pathways following multichannel innershell ionization.

APPENDIX A: THEORY AND DERIVATION

The EUV photoionization and the Auger-decay process are treated within the framework of perturbation theory to arrive at a condition for interference of two Auger pathways in magnesium. The far-infrared (FIR) or terahertz (THz) field cannot be treated perturbatively because it interacts strongly with the Auger electrons and photoelectrons. In such a case the total Hamiltonian of the system is given by

$$\hat{H}(t) = \hat{H}_0(t) + \lambda\hat{V}(t), \tag{A1}$$

where $\hat{H}_0(t) = \hat{H}_{0A} - E_0 + \hat{V}_{FIR}(t)$ is the atomic Hamiltonian including the FIR field, with $\hat{H}_{0A}$ being the unperturbed atomic Hamiltonian, E_0 the ground-state energy of the Mg atom, and $\hat{V}_{FIR}(t)$ the FIR field. $\hat{V}(t) = \hat{V}_{EUV}(t) + \hat{V}_A$ is the perturbation which has contributions from EUV photoionization $\hat{V}_{EUV}(t)$ and Auger decay $\hat{V}_A$. Please note that we have assumed atomic units throughout the derivation, i.e., $\hbar = 1$.

The time evolution of the system is given by the time-dependent Schrödinger equation in atomic units:

$$i\partial_t |\Psi, t\rangle = \hat{H}(t)|\Psi, t\rangle. \tag{A2}$$

We assume that we have solved the FIR-only problem using the initial condition for the time evolution operator:

$$\hat{U}_{FIR}(t, -\infty) \to \exp[-i(\hat{H}_{0A} - E_0)t] \text{ as } t \to -\infty. \tag{A3}$$

Therefore in the absence of the perturbation, i.e., $\lambda = 0$, the solution of Eq. (A2) is

$$|\Psi_{FIR}, t\rangle \equiv \hat{U}_{FIR}(t, -\infty)|\Psi_0\rangle, \tag{A4}$$

where $|\Psi_0\rangle$ is the ground state of the Mg atom. Now we make the ansatz

$$|\Psi, t\rangle = |\Psi, t\rangle^{(0)} + \lambda|\Psi, t\rangle^{(1)} + \lambda^2|\Psi, t\rangle^{(2)} + \cdots, \tag{A5}$$

where $|\Psi, t\rangle^{(0)} = |\Psi_{FIR}, t\rangle$, $|\Psi, t\rangle^{(1)}$, and $|\Psi, t\rangle^{(2)}$ are the zero-, first- and second-order corrected wave functions. The correction terms are calculated by substituting Eqs. (A5) and (A1) in Eq. (A2), which gives

$$i\partial_t[|\Psi_{FIR}, t\rangle + \lambda|\Psi, t\rangle^{(1)} + \lambda^2|\Psi, t\rangle^{(2)}]$$
$$= [\hat{H}_0(t) + \lambda\hat{V}(t)][|\Psi_{FIR}, t\rangle$$
$$+ \lambda|\Psi, t\rangle^{(1)} + \lambda^2|\Psi, t\rangle^{(2)}]. \tag{A6}$$

Now comparing the coefficients of the λ terms from both the right-hand side (RHS) and the left-hand side (LHS) in

Eq. (A6), we obtain the time evolution of the first-order correction term:

$$i\partial_t |\Psi, t\rangle^{(1)} = \hat{H}_0(t)|\Psi, t\rangle^{(1)} + \hat{V}(t)|\Psi_{FIR}, t\rangle, \tag{A7}$$

which can be solved as a first-order differential equation with variable coefficients. The solution is

$$|\Psi, t\rangle^{(1)} = -i\hat{U}_{FIR}(t, -\infty)\int_{-\infty}^t dt'\hat{U}_{FIR}^\dagger(t', -\infty)\hat{V}(t')|\Psi_{FIR}, t'\rangle, \tag{A8}$$

$$|\Psi, t\rangle^{(1)} = -i\int_{-\infty}^t dt'\hat{U}_{FIR}(t, t')\hat{V}(t')|\Psi_{FIR}, t'\rangle, \tag{A9}$$

where $\hat{U}_{FIR}(t, t') = U_{FIR}(t, -\infty)\hat{U}_{FIR}^\dagger(t', -\infty)$. Comparing the coefficients of λ^2 terms from both the RHS and the LHS in Eq. (A6), we obtain the time evolution of the second-order correction term:

$$i\partial_t |\Psi, t\rangle^{(2)} = \hat{H}_0(t)|\Psi, t\rangle^{(2)} + \hat{V}(t)|\Psi, t\rangle^{(1)}. \tag{A10}$$

It can be solved similarly as the first-order correction term, which gives

$$|\Psi, t\rangle^{(2)} = -i\int_{-\infty}^t dt'\hat{U}_{FIR}(t, t')\hat{V}(t')|\Psi, t'\rangle^{(1)}. \tag{A11}$$

Substituting Eq. (A9) into Eq. (A11), we get

$$|\Psi, t\rangle^{(2)} = -\int_{-\infty}^t dt'\int_{-\infty}^{t'} dt''\hat{U}_{FIR}(t, t')\hat{V}(t')\hat{U}_{FIR}$$
$$\times (t', t'')\hat{V}(t'')|\Psi_{FIR}, t''\rangle. \tag{A12}$$

Using $\hat{V}(t) = \hat{V}_{EUV}(t) + \hat{V}_A$ and Eq. (A4), we obtain

$$|\Psi, t\rangle^{(2)} = -\int_{-\infty}^t dt'\int_{-\infty}^{t'} dt''\hat{U}_{FIR}(t, t')[\hat{V}_{EUV}(t')$$
$$+ \hat{V}_A]\hat{U}_{FIR}(t', t'')$$
$$\times [\hat{V}_{EUV}(t'') + \hat{V}_A]\hat{U}_{FIR}(t'', -\infty)|\Psi_0\rangle. \tag{A13}$$

Out of four terms in the above equation, we are interested in the term in which there is first EUV photoionization and then Auger decay. The second-order corrected wave function for the corresponding process is

$$|\Psi, t\rangle^{(2)} = -\int_{-\infty}^t dt'\int_{-\infty}^{t'} dt''\hat{U}_{FIR}(t, t')\hat{V}_A\hat{U}_{FIR}(t', t'')$$
$$\times \hat{V}_{EUV}(t'')\hat{U}_{FIR}(t'', -\infty)|\Psi_0\rangle. \tag{A14}$$

We choose the polarization direction of the EUV pulse along the z axis to obtain $\hat{V}_{EUV}(t'') = \varepsilon_{EUV}(t'')\hat{Z}$, where ε_{EUV} describes the time evolution of the EUV pulse. We further assume that the FIR field is too weak to perturb the ground state. Hence, $\hat{U}_{FIR}(t'', -\infty)|\Psi_0\rangle = e^{-i(\hat{H}_{0A} - E_0)t''}|\Psi_0\rangle = |\Psi_0\rangle$. Substituting both relations into Eq. (A14) gives

$$|\Psi, t\rangle^{(2)} = -\int_{-\infty}^t dt'\int_{-\infty}^{t'} dt''\hat{U}_{FIR}(t, t')\hat{V}_A\hat{U}_{FIR}$$
$$\times (t', t'')\varepsilon_{EUV}(t'')\hat{Z}|\Psi_0\rangle. \tag{A15}$$

We now define the one-hole–one-particle wave functions, $|\Psi_k^b\rangle$ and $|\Psi_j^a\rangle$, and the two-hole–two-particle wave functions, $|\Psi_{k'k''}^{b'b''}\rangle$ and $|\Psi_{j'j''}^{a'a''}\rangle$, in which the subscript indices,

e.g., k and j, represent the holes and the superscript indices, e.g., a and b, represent the particles. These one-hole–one-particle and two-hole–two-particle wave functions are defined relative to $|\Psi_0\rangle$, which we assume to be a single Slater determinant, and are eigenstates of the

unperturbed atomic Hamiltonian $\hat{H}_{0A}$, which we assume to be a mean-field Hamiltonian. We insert four completeness relations $\sum_{\substack{j \\ a}} |\Psi_j^a\rangle \langle \Psi_j^a|$, $\sum_{\substack{k \\ b}} |\Psi_k^b\rangle \langle \Psi_k^b|$, $\sum_{\substack{j'' > j' \\ a'' > a'}} |\Psi_{j'j''}^{a'a''}\rangle \langle \Psi_{j'j''}^{a'a''}|$,

and $\sum_{\substack{k'' > k' \\ b'' > b'}} |\Psi_{k'k''}^{b'b''}\rangle \langle \Psi_{k'k''}^{b'b''}|$ into Eq. (A15) and obtain

$$|\Psi, t\rangle^{(2)} = -\sum_{\substack{k'' > k' \\ b'' > b'}} \sum_{\substack{j'' > j' \\ a'' > a'}} \sum_{\substack{k \\ b}} \sum_{\substack{j \\ a}} \int_{-\infty}^{t} dt' \int_{-\infty}^{t'} dt'' \, |\Psi_{k'k''}^{b'b''}\rangle \langle \Psi_{k'k''}^{b'b''}| \hat{U}_{\text{FIR}}(t, t') |\Psi_{j'j''}^{a'a''}\rangle$$

$$\times \langle \Psi_{j'j''}^{a'a''}| \hat{V}_A |\Psi_k^b\rangle \langle \Psi_k^b| \hat{U}_{\text{FIR}}(t', t'') |\Psi_j^a\rangle \varepsilon_{\text{EUV}}(t'') \langle \Psi_j^a| \hat{Z} |\Psi_0\rangle. \tag{A16}$$

As $\hat{Z}$ is a one-body operator we can use the Slater-Condon rules to evaluate $\langle \Psi_j^a| \hat{Z} |\Psi_0\rangle$, which gives $\langle \varphi_a| \hat{Z} |\varphi_j\rangle$, where φ_a and φ_j are atomic spin orbitals. We assume that the FIR field does not induce particle-hole excitations. We further assume that the FIR field does not have any effect on the holes but only on the particles. Therefore, $\langle \Psi_k^b| \hat{U}_{\text{FIR}}(t', t'') |\Psi_j^a\rangle$ reduces to $\delta_{jk} u_{ba}$, where u_{ba} is the transition amplitude of the photoelectron from a to b due to the FIR field. Thus we obtain

$$|\Psi, t\rangle^{(2)} = -\sum_{\substack{k'' > k' \\ b'' > b'}} \sum_{\substack{j'' > j' \\ a'' > a'}} \sum_{\substack{k \\ b}} \sum_{\substack{j \\ a}} \int_{-\infty}^{t} dt' \int_{-\infty}^{t'} dt'' \, |\Psi_{k'k''}^{b'b''}\rangle \langle \Psi_{k'k''}^{b'b''}| \hat{U}_{\text{FIR}}(t, t') |\Psi_{j'j''}^{a'a''}\rangle$$

$$\times \langle \Psi_{j'j''}^{a'a''}| \hat{V}_A |\Psi_k^b\rangle \delta_{jk} u_{ba}(t', t'') e^{-iI_j(t'-t'')} \varepsilon_{\text{EUV}}(t'') \langle \varphi_a| \hat{Z} |\varphi_j\rangle, \tag{A17}$$

where $I_j = -\epsilon_j$ is the ionization energy to remove a particle from orbital j. Utilizing the Kronecker δ we can remove the summation over k and obtain

$$|\Psi, t\rangle^{(2)} = -\sum_{\substack{k'' > k' \\ b'' > b'}} \sum_{\substack{j'' > j' \\ a'' > a'}} \sum_{b} \sum_{\substack{j \\ a}} \int_{-\infty}^{t} dt' \int_{-\infty}^{t'} dt'' \, |\Psi_{k'k''}^{b'b''}\rangle \langle \Psi_{k'k''}^{b'b''}| \hat{U}_{\text{FIR}}(t, t') |\Psi_{j'j''}^{a'a''}\rangle$$

$$\times \langle \Psi_{j'j''}^{a'a''}| \hat{V}_A |\Psi_j^b\rangle u_{ba}(t', t'') e^{-iI_j(t'-t'')} \varepsilon_{\text{EUV}}(t'') z_{aj}. \tag{A18}$$

The two-body operator $\hat{V}_A$ does not affect the ejected photoelectron which gives a condition on the index a', i.e., $a' = b$ and the summation of a' can be removed to obtain

$$|\Psi, t\rangle^{(2)} = -\sum_{\substack{k'' > k' \\ b'' > b'}} \sum_{\substack{j'' > j' \\ a'' > b}} \sum_{\substack{j \\ a}} \int_{-\infty}^{t} dt' \int_{-\infty}^{t'} dt'' \, |\Psi_{k'k''}^{b'b''}\rangle \langle \Psi_{k'k''}^{b'b''}| \hat{U}_{\text{FIR}}(t, t') |\Psi_{j'j''}^{ba''}\rangle$$

$$\times \langle \Psi_{j'j''}^{ba''}| \hat{V}_A |\Psi_j^b\rangle u_{ba}(t', t'') e^{-iI_j(t'-t'')} \varepsilon_{\text{EUV}}(t'') z_{aj}. \tag{A19}$$

The term consisting of the two-body operator $\hat{V}_A$ can also be evaluated using Slater-Condon rules, by assuming that the photoelectron, labeled as b in this case, is merely a spectator in the Auger process. Therefore,

$$|\Psi, t\rangle^{(2)} = -\sum_{\substack{k'' > k' \\ b'' > b'}} \sum_{\substack{j'' > j' \\ a'' > b}} \sum_{\substack{j \\ a}} \int_{-\infty}^{t} dt' \int_{-\infty}^{t'} dt'' \, |\Psi_{k'k''}^{b'b''}\rangle \langle \Psi_{k'k''}^{b'b''}| \hat{U}_{\text{FIR}}(t, t') |\Psi_{j'j''}^{ba''}\rangle$$

$$\times v_{a''jj'j''} u_{ba}(t', t'') e^{-iI_j(t'-t'')} \varepsilon_{\text{EUV}}(t'') z_{aj}. \tag{A20}$$

Here, $v_{a''jj'j''} = \langle \varphi_{a''}\varphi_j| \hat{V}_A |\varphi_{j'}\varphi_{j''}\rangle - \langle \varphi_{a''}\varphi_j| \hat{V}_A |\varphi_{j''}\varphi_{j'}\rangle$, where $\varphi_{a''}$, φ_j, $\varphi_{j'}$ and $\varphi_{j''}$ are again the atomic spin orbitals. As before, we assume that the FIR field does not affect the holes, but only the particles, which reduces $\langle \Psi_{k'k''}^{b'b''}| \hat{U}_{\text{FIR}}(t, t') |\Psi_{j'j''}^{ba''}\rangle$ to $\delta_{j'k'}\delta_{j''k''}u_{b'b}(t, t')u_{b''a''}(t, t')$, where $u_{b'b}(t, t')$ and $u_{b''a''}(t, t')$ are the transition amplitudes of the photoelectron from b to b' and of the Auger electron from a'' to b'', respectively:

$$|\Psi, t\rangle^{(2)} = -\sum_{\substack{k'' > k' \\ b'' > b'}} \sum_{\substack{j'' > j' \\ a'' > b}} \sum_{\substack{j \\ a}} \int_{-\infty}^{t} dt' \int_{-\infty}^{t'} dt'' \, |\Psi_{k'k''}^{b'b''}\rangle \delta_{j'k'}\delta_{j''k''} u_{b'b}(t, t')u_{b''a''}(t, t')$$

$$\times e^{-iI_{j'j''}(t-t')} v_{a''jj'j''} u_{ba}(t', t'') e^{-iI_j(t'-t'')} \varepsilon_{\text{EUV}}(t'') z_{aj}. \tag{A21}$$

Here, $I_{j'j''}$ is the eigenenergy of the double-hole state with holes in the orbitals j and j'. Resolving the Kronecker δ's further removes the summation over k' and k'':

$$
|\Psi, t\rangle^{(2)} = - \sum_{\substack{b'' > b' \\ a'' > b}} \sum_{\substack{j'' > j' \\ a}} \sum_{j} \int_{-\infty}^{t} dt' \int_{-\infty}^{t'} dt'' \, |\Psi_{j'j''}^{b'b''}\rangle u_{b'b}(t, t') u_{b''a''}(t, t')
$$

$$
\times \, e^{-iI_{j'j''}(t-t')} v_{a''jj'j''} u_{ba}(t', t'') e^{-iI_j(t'-t'')} \varepsilon_{\text{EUV}}(t'') z_{aj}. \tag{A22}
$$

The observable connected to the Auger-electron spectrum is defined as a sum over projectors onto the Auger-electron state α:

$$
\hat{P}_\alpha = \sum_{\substack{\gamma > \beta \\ \Pi(\Pi < \alpha)}} |\Psi_{\beta\gamma}^{\Pi\alpha}\rangle\langle\Psi_{\beta\gamma}^{\Pi\alpha}|, \tag{A23}
$$

where $|\Psi_{\beta\gamma}^{\Pi\alpha}\rangle$ is a two-hole–two-particle eigenstate of the unperturbed atomic Hamiltonian $\hat{H}_{0A}$. Now we take the expectation value with the second-order corrected state vector:

$$
P_\alpha = \sum_{\substack{\gamma > \beta \\ \Pi(\Pi < \alpha)}} \left|\langle\Psi_{\beta\gamma}^{\Pi\alpha}|\Psi, t^{(2)}\rangle\right|^2 = \sum_{\substack{\gamma > \beta \\ \Pi(\Pi < \alpha)}} \left| \sum_{\substack{b'' > b' \\ a'' > b}} \sum_{\substack{j'' > j' \\ a}} \sum_{j} \int_{-\infty}^{t} dt' \int_{-\infty}^{t'} dt'' \langle\Psi_{\beta\gamma}^{\Pi\alpha}|\Psi_{j'j''}^{b'b''}\rangle \right.
$$

$$
\left. \times \, u_{b'b}(t, t') u_{b''a''}(t, t') e^{-iI_{j'j''}(t-t')} v_{a''jj'j''} u_{ba}(t', t'') e^{-iI_j(t'-t'')} \varepsilon_{\text{EUV}}(t'') z_{aj} \right|^2. \tag{A24}
$$

Since, by assumption, both $|\Psi_{\beta\gamma}^{\Pi\alpha}\rangle$ and $|\Psi_{j'j''}^{b'b''}\rangle$ are eigenstates of the unperturbed atomic Hamiltonian $\hat{H}_{0A}$, we obtain

$$
P_\alpha = \sum_{\substack{\gamma > \beta \\ \Pi(\Pi < \alpha)}} \left| \sum_{\substack{b'' > b' \\ a'' > b}} \sum_{\substack{j'' > j' \\ a}} \sum_{j} \int_{-\infty}^{t} dt' \int_{-\infty}^{t'} dt'' \delta_{\beta j'} \delta_{\gamma j''} \delta_{\Pi b'} \delta_{\alpha b''} u_{b'b}(t, t') u_{b''a''}(t, t') \right.
$$

$$
\left. \times \, e^{-iI_{j'j''}(t-t')} v_{a''jj'j''} u_{ba}(t', t'') e^{-iI_j(t'-t'')} \varepsilon_{\text{EUV}}(t'') z_{aj} \right|^2. \tag{A25}
$$

Thus,

$$
P_\alpha = \sum_{\substack{\gamma > \beta \\ \Pi(\Pi < \alpha)}} \left| \sum_{\substack{a'' > b \\ a}} \sum_{j} \int_{-\infty}^{t} dt' \int_{-\infty}^{t'} dt'' u_{\Pi b}(t, t') u_{\alpha a''}(t, t') e^{-iI_{\beta\gamma}(t-t')} v_{a''j\beta\gamma} u_{ba}(t', t'') e^{-iI_j(t'-t'')} \varepsilon_{\text{EUV}}(t'') z_{aj} \right|^2. \tag{A26}
$$

We use $\sum_b u_{\Pi b}(t, t') u_{ba}(t', t'') = u_{\Pi a}(t, t'')$ in the above equation, which gives

$$
P_\alpha = \sum_{\substack{\gamma > \beta \\ \Pi(\Pi < \alpha)}} \left| \sum_{a''} \sum_{j} \int_{-\infty}^{t} dt' \int_{-\infty}^{t'} dt'' u_{\alpha a''}(t, t') e^{-iI_{\beta\gamma}(t-t')} \right.
$$

$$
\left. \times \, v_{a''j\beta\gamma} u_{\Pi a}(t, t'') e^{-iI_j(t'-t'')} \varepsilon_{\text{EUV}}(t'') z_{aj} \right|^2. \tag{A27}
$$

To account for the exponential decay of the hole j, we rewrite I_j as $I_j - i\frac{\Gamma_j}{2}$, where Γ_j is the decay rate. Hence,

$$
P_\alpha = \sum_{\substack{\gamma > \beta \\ \Pi(\Pi < \alpha)}} \left| \sum_{a''} \sum_{j} \int_{-\infty}^{t} dt' \int_{-\infty}^{t'} dt'' u_{\alpha a''}(t, t') e^{-iI_{\beta\gamma}(t-t')} \right.
$$

$$
\left. \times \, v_{a''j\beta\gamma} u_{\Pi a}(t, t'') e^{-i(I_j - i\frac{\Gamma_j}{2})(t'-t'')} \varepsilon_{\text{EUV}}(t'') z_{aj} \right|^2. \tag{A28}
$$

In Eq. (A28), the terms $u_{\Pi a}(t, t'')$ and $u_{\alpha a''}(t, t')$ represent the FIR dressed photoelectron (Π) and the Auger electron (α) after EUV photoionization and Auger decay, respectively. Here we emphasize the assumption that the holes are not affected by the FIR field. This is a generalized expression for the signal one gets within our model. The one-body term z_{aj} and the two-body term $v_{a''j\beta\gamma}$ represent the photoinonization and the Auger decay, respectively. The FIR field dressings of photoelectrons and Auger electrons are given by the matrix elements $u_{\Pi a}(t, t'')$ and $u_{\alpha a''}(t, t')$, respectively.

APPENDIX B: APPROXIMATIONS

To simplify Eq. (A28) and allow for a comparison with the experimental spectrum we first assume the EUV pulse to be a δ pulse in the form $\varepsilon_{\text{EUV}}(t) = \varepsilon_0 \, \delta(t - t_{\text{EUV}})$, where ε_0 is the strength of the pulse. By using this δ-pulse approximation in Eq. (A28), we get the following for $t > t_{\text{EUV}}$:

$$
P_\alpha = \sum_{\substack{\gamma > \beta \\ \Pi(\Pi < \alpha)}} \left| \sum_{a''} \sum_{\substack{j \\ a}} \int_{t_{\text{EUV}}}^t dt' u_{\alpha a''}(t, t') e^{-iI_{\beta\gamma}(t-t')} \right.
$$
$$
\left. \times v_{a''j\beta\gamma} u_{\Pi a}(t, t_{\text{EUV}}) e^{-i(I_j - i\frac{\Gamma_j}{2})(t'-t_{\text{EUV}})} \varepsilon_0 z_{aj} \right|^2 . \quad \text{(B1)}
$$

Second, we look at the form of the equation in the absence of the FIR field. The transition amplitudes are then

$$
u_{\alpha a''}(t, t') = e^{-i\varepsilon_\alpha(t-t')} \delta_{\alpha a''}, \quad \text{(B2)}
$$

$$
u_{\Pi a}(t, t_{\text{EUV}}) = e^{-i\varepsilon_\Pi(t-t_{\text{EUV}})} \delta_{\Pi a}. \quad \text{(B3)}
$$

Using these, we get the following for $t > t_{\text{EUV}}$:

$$
P_\alpha = \sum_{\substack{\gamma > \beta \\ \Pi(\Pi < \alpha)}} \left| \sum_j \int_{t_{\text{EUV}}}^t dt' e^{-i\varepsilon_\alpha(t-t')} e^{-iI_{\beta\gamma}(t-t')} \right.
$$
$$
\left. \times v_{\alpha j\beta\gamma} e^{-i\varepsilon_\Pi(t-t_{\text{EUV}})} e^{-i(I_j - i\frac{\Gamma_j}{2})(t'-t_{\text{EUV}})} \varepsilon_0 \, z_{\Pi j} \right|^2 \quad \text{(B4)}
$$

$$
= \sum_{\substack{\gamma > \beta \\ \Pi(\Pi < \alpha)}} \left| \sum_j \int_{t_{\text{EUV}}}^t dt' e^{i\varepsilon_\alpha t'} e^{iI_{\beta\gamma}t'} \right.
$$
$$
\left. \times v_{\alpha j\beta\gamma} e^{i\varepsilon_\Pi t_{\text{EUV}}} e^{-i(I_j - i\frac{\Gamma_j}{2})(t'-t_{\text{EUV}})} \varepsilon_0 z_{\Pi j} \right|^2 , \quad \text{(B5)}
$$

where we exploited that $|e^{-i(I_{\beta\gamma} + \varepsilon_\alpha + \varepsilon_\Pi)t}|^2 = 1$. By carrying out the integral and expanding the modulus, the resulting expression for the Auger-electron spectrum, in the limit $t \to \infty$, will be in the form of Lorentzians, peaked at the energies $I_j - I_{\beta\gamma}$.

To approximately take the FIR field into account, we employ Eq. (B1) and make the following ansatz for the transition amplitudes:

$$
u_{\alpha a''}(t, t') = e^{-i\epsilon_\alpha(t-t')} e^{-ibt'^2} g_{\alpha a''}, \quad \text{(B6)}
$$

$$
u_{\Pi a}(t, t_{\text{EUV}}) = e^{-i\epsilon_\Pi(t-t_{\text{EUV}})} g_{\Pi a}. \quad \text{(B7)}
$$

This ansatz is motivated by the following two observations. First, we are interested in the limit of large t, i.e., much larger than the duration of the FIR pulse. At large times t, both the photoelectron and the Auger electron propagate freely. Second, t' is constrained by the exponential decay to an interval that is short in comparison to the FIR cycle and, thus, also in comparison to the FIR pulse duration.

In this way, we take into consideration a leading-order FIR-induced electronic chirp on the timescale governed by the Auger decay. Moreover, by replacing the previous Kronecker δ's in Eqs. (B2) and (B3), with $g_{\alpha a''}$ and $g_{\Pi a}$, we take into consideration that the FIR field can change the state of both the photoelectron and the Auger electron.

We insert the expressions for the electronic transition amplitudes given in Eqs. (B6) and (B7) into Eq. (B1):

$$
P_\alpha = \sum_{\substack{\gamma > \beta \\ \Pi(\Pi < \alpha)}} \left| \sum_j \int_{t_{\text{EUV}}}^t dt' e^{-iI_{\beta\gamma}(t-t')} e^{-i\epsilon_\alpha(t-t')} e^{-ibt'^2} \right.
$$
$$
\times e^{-i(I_j - i\frac{\Gamma_j}{2})(t'-t_{\text{EUV}})} e^{-i\epsilon_\Pi(t-t_{\text{EUV}})}
$$
$$
\left. \times \underbrace{\sum_{a\,a''} v_{a''j\beta\gamma} g_{\alpha a''} g_{\Pi a} \varepsilon_0 z_{aj}}_{A_{j\alpha\beta\gamma\Pi}} \right|^2 . \quad \text{(B8)}
$$

By adding and removing suitable complex phase factors of modulus one, performing the substitution $t' - t_{\text{EUV}} \to t'$, and taking the limit $t \to \infty$, Eq. (B8) goes over into

$$
P_\alpha = \sum_{\substack{\gamma > \beta \\ \Pi(\Pi < \alpha)}} \left| \sum_j A_{j\alpha\beta\gamma\Pi} \int_0^\infty dt' e^{-i(I_j - i\Gamma_j/2 - I_{\beta\gamma} - \varepsilon_\alpha)t'} \right.
$$
$$
\left. \times e^{-ib(t' + t_{\text{EUV}})^2} \right|^2
$$
$$
= \sum_{\substack{\gamma > \beta \\ \Pi(\Pi < \alpha)}} \left| \int_{-\infty}^\infty dt' \Psi_{\alpha\beta\gamma\Pi}(t'; t_{\text{EUV}}) e^{i\varepsilon_\alpha t'} \right|^2 , \quad \text{(B9)}
$$

where we have rewritten the Auger spectrum in the presence of the FIR field in terms of the Fourier transform of transition amplitudes:

$$
\Psi_{\alpha\beta\gamma\Pi}(t'; t_{\text{EUV}})
$$
$$
= \begin{cases} \sum_j A_{j\alpha\beta\gamma\Pi} e^{-i(I_j - i\Gamma_j/2 - I_{\beta\gamma})t'} e^{-ib(t' + t_{\text{EUV}})^2}, & t' \geqslant 0, \\ 0, & t' < 0. \end{cases}
$$
$$
\text{(B10)}
$$

The coefficients $A_{j\alpha\beta\gamma\Pi}$, defined in Eq. (B8), are complex numbers carrying phase information from photoionization (argument of z_{aj}) and Auger decay (argument of $v_{a''j\beta\gamma}$), and from the FIR dressing of the photoelectron (argument of $g_{\Pi a}$) and the Auger electron (argument of $g_{\alpha a''}$).

Equation (B9) is consistent with the expectation that, if $b = 0$, the time t_{EUV} at which the pump δ pulse is assumed

to be centered has no consequence for the Auger spectrum. Only if $b \neq 0$ (i.e., in the presence of the FIR field) does the transition amplitude in Eq. (B10) and, therefore, the Auger spectrum depend explicitly on t_{EUV}. This, in turn, implies that the Auger spectrum must depend on the distribution of t_{EUV} values, as defined by the envelope of the actual (non-δ) EUV field.

---

[1] D. Attwood, *Soft X-Rays and Extreme Ultraviolet Radiation: Principles and Applications* (Cambridge University, Cambridge, England, 1999).

[2] J. Als-Nielsen and D. McMorrow, *Elements of Modern X-Ray Physics* (Wiley & Sons, New York, 2011).

[3] L. Young, K. Ueda, M. Gühr, P. H. Bucksbaum, M. Simon, S. Mukamel, N. Rohringer, K. C. Prince, C. Masciovecchio, M. Meyer *et al.*, J. Phys. B: At., Mol. Opt. Phys. **51**, 032003 (2018).

[4] T. Glover, D. Fritz, M. Cammarata, T. Allison, S. Coh, J. Feldkamp, H. Lemke, D. Zhu, Y. Feng, R. Coffee *et al.*, Nature (London) **488**, 603 (2012).

[5] C. Buth, R. Santra, and L. Young, Phys. Rev. Lett. **98**, 253001 (2007).

[6] T. Glover, M. Hertlein, S. Southworth, T. Allison, J. van Tilborg, E. Kanter, B. Krässig, H. Varma, B. Rude, R. Santra *et al.*, Nat. Phys. **6**, 69 (2010).

[7] E. R. Peterson, C. Buth, D. A. Arms, R. W. Dunford, E. P. Kanter, B. Krässig, E. C. Landahl, S. T. Pratt, R. Santra, S. H. Southworth *et al.*, Appl. Phys. Lett. **92**, 094106 (2008).

[8] C. Buth and R. Santra, J. Chem. Phys. **129**, 134312 (2008).

[9] C. Ott, A. Kaldun, P. Raith, K. Meyer, M. Laux, J. Evers, C. H. Keitel, C. H. Greene, and T. Pfeifer, Science **340**, 716 (2013).

[10] A. Kaldun, A. Blättermann, V. Stooß, S. Donsa, H. Wei, R. Pazourek, S. Nagele, C. Ott, C. Lin, J. Burgdörfer *et al.*, Science **354**, 738 (2016).

[11] I. Grguraš, A. R. Maier, C. Behrens, T. Mazza, T. Kelly, P. Radcliffe, S. Düsterer, A. Kazansky, N. Kabachnik, T. Tschentscher *et al.*, Nat. Photonics **6**, 852 (2012).

[12] W. Helml, A. Maier, W. Schweinberger, I. Grguraš, P. Radcliffe, G. Doumy, C. Roedig, J. Gagnon, M. Messerschmidt, S. Schorb *et al.*, Nat. Photonics **8**, 950 (2014).

[13] T. Mazza, M. Ilchen, A. J. Rafipoor, C. Callegari, P. Finetti, O. Plekan, K. C. Prince, R. Richter, M. Danailov, A. Demidovich *et al.*, Nat. Commun. **5**, 3648 (2014).

[14] T. E. Glover, R. W. Schoenlein, A. H. Chin, and C. V. Shank, Phys. Rev. Lett. **76**, 2468 (1996).

[15] P. M. Paul, E. S. Toma, P. Breger, G. Mullot, F. Augé, P. Balcou, H. G. Muller, and P. Agostini, Science **292**, 1689 (2001).

[16] A. Baltuška, T. Udem, M. Uiberacker, M. Hentschel, E. Goulielmakis, C. Gohle, R. Holzwarth, V. Yakovlev, A. Scrinzi, T. W. Hänsch *et al.*, Nature (London) **421**, 611 (2003).

[17] M. Drescher, M. Hentschel, R. Kienberger, M. Uiberacker, V. Yakovlev, A. Scrinzi, T. Westerwalbesloh, U. Kleineberg, U. Heinzmann, and F. Krausz, Nature (London) **419**, 803 (2002).

[18] L. Miaja-Avila, C. Lei, M. Aeschlimann, J. L. Gland, M. M. Murnane, H. C. Kapteyn, and G. Saathoff, Phys. Rev. Lett. **97**, 113604 (2006).

[19] K. Hütten, M. Mittermair, S. O. Stock, R. Beerwerth, V. Shirvanyan, J. Riemensberger, A. Duensing, R. Heider, M. S. Wagner, A. Guggenmos *et al.*, Nat. Commun. **9**, 719 (2018).

[20] J. M. Schins, P. Breger, P. Agostini, R. C. Constantinescu, H. G. Muller, G. Grillon, A. Antonetti, and A. Mysyrowicz, Phys. Rev. Lett. **73**, 2180 (1994).

[21] M. Meyer, P. Radcliffe, T. Tschentscher, J. T. Costello, A. L. Cavalieri, I. Grguras, A. R. Maier, R. Kienberger, J. Bozek, C. Bostedt *et al.*, Phys. Rev. Lett. **108**, 063007 (2012).

[22] P. Ranitovic, X. M. Tong, C. W. Hogle, X. Zhou, Y. Liu, N. Toshima, M. M. Murnane, and H. C. Kapteyn, Phys. Rev. Lett. **106**, 053002 (2011).

[23] B. Cooper and V. Averbukh, Phys. Rev. Lett. **111**, 083004 (2013).

[24] D. Iablonskyi, K. Ueda, K. L. Ishikawa, A. S. Kheifets, P. Carpeggiani, M. Reduzzi, H. Ahmadi, A. Comby, G. Sansone, T. Csizmadia *et al.*, Phys. Rev. Lett. **119**, 073203 (2017).

[25] U. Frühling, M. Wieland, M. Gensch, T. Gebert, B. Schütte, M. Krikunova, R. Kalms, F. Budzyn, O. Grimm, J. Rossbach *et al.*, Nat. Photonics **3**, 523 (2009).

[26] B. Schütte, U. Frühling, M. Wieland, A. Azima, and M. Drescher, Opt. Express **19**, 18833 (2011).

[27] B. Schütte, S. Bauch, U. Frühling, M. Wieland, M. Gensch, E. Plönjes, T. Gaumnitz, A. Azima, M. Bonitz, and M. Drescher, Phys. Rev. Lett. **108**, 253003 (2012).

[28] O. Schwarzkopf and V. Schmidt, J. Phys. B: At., Mol. Opt. Phys. **29**, 3023 (1996).

[29] E. Kukk, H. Aksela, A. Kivimäki, J. Jauhiainen, E. Nõmmiste, and S. Aksela, Phys. Rev. A **56**, 1481 (1997).

[30] R. Camilloni, M. Žitnik, C. Comicioli, K. C. Prince, M. Zacchigna, C. Crotti, C. Ottaviani, C. Quaresima, P. Perfetti, and G. Stefani, Phys. Rev. Lett. **77**, 2646 (1996).

[31] A. Niehaus, J. Phys. B: At. Mol. Phys. **10**, 1845 (1977).

[32] S. Rioual, B. Rouvellou, L. Avaldi, G. Battera, R. Camilloni, G. Stefani, and G. Turri, Phys. Rev. Lett. **86**, 1470 (2001).

[33] M. Neeb, J.-E. Rubensson, M. Biermann, and W. Eberhardt, J. Electron Spectrosc. Relat. Phenom. **67**, 261 (1994).

[34] R. Feifel, T. Tanaka, M. Hoshino, H. Tanaka, Y. Tamenori, V. Carravetta, and K. Ueda, Phys. Rev. A **74**, 062717 (2006).

[35] C. Vozzi, M. Nisoli, G. Sansone, S. Stagira, and S. De Silvestri, Appl. Phys. B **80**, 285 (2005).

[36] J. Hebling, G. Almasi, I. Z. Kozma, and J. Kuhl, Opt. Express **10**, 1161 (2002).

[37] B. Breuckmann, V. Schmidt, and W. Schmitz, J. Phys. B: At., Mol. Opt. Phys. **9**, 3037 (1976).

[38] L. Forrest, G. James, K. Ross, and V. Pejcev, J. Phys. B: At., Mol. Opt. Phys. **16**, 4671 (1983).

5.2 Infrared-laser-pulse-enhanced ultrafast fragmentation of N_2^{2+} following Auger decay: Mixed quantum-classical simulations

Murali Krishna Ganesa Subramanian, Robin Santra and Ralph Welsch

Phys. Rev. A, **98**, 063421 (2018).

©2018 American Physical Society

Statement of contribution

The theoretical concept of mixed quantum-classical simulation was developed by Robin Santra. All the calculations were carried out by myself under the guidance of Robin Santra and Ralph Welsch. The writing of manuscript was partly done by Ralph Welsch and myself.

Infrared-laser-pulse-enhanced ultrafast fragmentation of N₂²⁺ following Auger decay: Mixed quantum-classical simulations

Murali Krishna Ganesa Subramanian,[1,2,*] Robin Santra,[1,2,3] and Ralph Welsch[1]

[1]*Center for Free-Electron Laser Science, DESY, Notkestrasse 85, D-22607 Hamburg, Germany*
[2]*Department of Physics, University of Hamburg, Jungiusstrasse 9, D-20355 Hamburg, Germany*
[3]*The Hamburg Centre for Ultrafast Imaging, Luruper Chaussee 149, D-22761 Hamburg, Germany*

We employ mixed quantum-classical molecular dynamics simulations to investigate the fragmentation of N₂ molecules after core-level photoionization by an x-ray laser, subsequent Auger decay, and followed by a femtosecond IR pulse that interacts with N₂²⁺. The delayed IR pulse couples the dissociative electronic states of N₂²⁺ with electronic states that can support long-lived vibrational resonances. We compare our simulations with previous quantum dynamics calculations in a quasidiabatic representation, which employed a small number of electronic states. Good agreement for both the Auger spectrum as well as the influence of the delayed IR pulse is found. By employing the mixed quantum-classical treatment, we can greatly reduce the computational cost to simulate the fragmentation dynamics compared to the quantum dynamics simulations. Furthermore, we reinvestigate the title process by employing an extended set of adiabatic potential energy surfaces and also investigate the role of nonadiabatic coupling in the process. The use of the full set of adiabatic potentials increases the dissociation probability and changes the details of the interaction with the IR pulse, but no effect due to the nonadiabatic coupling is found.

I. INTRODUCTION

The technological advances of x-ray free-electron lasers (FELs) allow the study of complex molecular processes with high temporal and spatial resolution. Pump-probe experiments using FELs give the possibility to observe ultrafast phenomena in quantum systems that occur on the time scale of few tens to hundreds of femtoseconds. In particular, ultrashort x-ray pulses at FELs can be used to track atomic motion in molecules during photochemical processes [1]. Using the Linac Coherent Light Source (LCLS) at SLAC National Laboratory [2] core-shell ionization and subsequent dynamics in diatomic and polyatomic molecules such as N₂, H₂S, and SF₆ have been investigated [3–6].

Molecular nitrogen and its dication have been well studied in spectroscopy because of their metastable states [7–16]. To investigate the x-ray ionization and subsequent fragmentation dynamics of N₂, time-resolved pump-probe experiments were performed at LCLS [1]. Following core-shell ionization by an x-ray pulse, molecular N₂²⁺ is produced by Auger decay. The N₂ dication has a few vibrationally long-lived quasibound metastable states [7,17–19]. The experiment observed the unfragmented-N₂²⁺ yield as a function of time delay between the ionizing x-ray pulse and a subsequent IR pulse. A decrease in the unfragmented-N₂²⁺ yield has been reported from the experiment [1].

In a recent quantum dynamics (QD) [20] investigation, the interaction of the IR pulse with the dicationic system

as a function of time delay of the IR pulse has been investigated using the multiconfiguration time-dependent Hartree (MCTDH) [21–23] method and similar trends as in the experiment have been observed [20]. Additionally, the dependence of unfragmented N₂²⁺ on intensity and width of the IR pulse was investigated. For certain Auger energies and pulse delays, a slight increase in the unfragmented-N₂²⁺ yield was found. However, the exact wave packet propagation is very time consuming and its computational cost scales exponentially with increasing system size. Thus, this approach is less suitable to investigate the IR control of Coulomb explosions in polyatomic systems.

This work assesses the prospects of using the computationally efficient Tully's fewest switches surface hopping (FSSH) approach [24–28] to investigate the ultrafast dissociation of N₂²⁺. In FSSH the electrons are treated quantum mechanically, while the nuclei are treated classically, propagating along a trajectory $R(t)$. The classical trajectories evolve on a single potential energy surface (PES) and can switch between the electronic states based on a hopping probability, which is determined from the nonadiabatic coupling vector and the transition dipole moment for the case of an applied electric field [29–38].

The paper is organized as follows: In Sec. II, the basic expressions underlying the theory and the computational methods used in this work are presented. Section III discusses the Auger spectrum and unfragmented-N₂²⁺ yield, in a quasidiabatic representation from FSSH simulations, and compares to previous QD simulations [20]. Section IV gives a detailed discussion of the fragmentation dynamics in the adiabatic representation in comparison to the dynamics

---

*Corresponding author: murali.krishna@cfel.de

in the quasidiabatic representation and discusses the impact of nonadiabatic couplings. Finally, Sec. V summarizes this work.

II. THEORETICAL BACKGROUND

A. Fewest switches surface hopping

Throughout this work FSSH [24–27,29–39] is employed and the implementation largely follows Ref. [40]. In FSSH the electrons are treated quantum mechanically, while the nuclei are treated classically, propagating along a trajectory $R(t)$. The classical trajectories evolve on a single PES and can switch between the electronic states based on a hopping probability. To this end, the time-dependent Schrödinger equation (TDSE) for the electrons is solved along the nuclear trajectory,

$$i\hbar \dot{c}_k(t) = \sum_j c_j(t)[V_{kj} - i\hbar \dot{\vec{R}} \cdot \vec{d}_{kj}], \quad (1)$$

where the c_j are the expansion coefficients with respect to the representation adopted, the V_{kj} are the matrix elements of the electronic Hamiltonian, and the $\vec{d}_{kj}$ are the nonadiabatic coupling vectors (NAC). In the adiabatic representation, the matrix V_{kj} is diagonal. In the following, the adiabatic representation is assumed and, thus, V_{kj} is omitted if $k \neq j$. From Eq. (1) the rate of change of population of the jth electronic state reads

$$\dot{\rho}_{jj} = \sum_{k \neq j} b_{kj}, \quad (2)$$

where

$$b_{kj} = -2\text{Re}[\rho_{jk} \dot{\vec{R}} \cdot \vec{d}_{kj}], \quad (3)$$

$$\rho_{jk} = c_j c_k^*, \quad (4)$$

and the probability of switching from state j to state k, $P_{j \to k}$, is obtained as

$$P_{j \to k} = \frac{-b_{kj} \Delta t}{\rho_{jj}}, \quad (5)$$

where Δt is the time step for the nuclear dynamics. The hopping probability is compared to a uniformly distributed random number ζ, $0 < \zeta < 1$, and a hop occurs if $P_{j \to k}$ is larger than ζ. If a hop occurs, the velocities of the classical trajectory are adjusted along the direction the nonadiabatic coupling vector to conserve the total energy. Hopping is not performed if there is not enough energy available for this adjustment.

FSSH can be extended to account for coupling of electronic states due to an external field [29–34,36–38,41], where the Hamiltonian for the external field is given by $H_{\text{ext}} = -\vec{E}(t) \cdot \vec{\mu}$, with $\vec{\mu}$ the dipole operator in length form. In this work a Gaussian shaped pulse polarized along the z axis is used and

$$\vec{E}(t) = E_0 e^{-\frac{1}{2}(\frac{t-t_0}{\sigma})^2} \cos(\hbar\omega_f(t - t_0) + \Phi)\hat{z}, \quad (6)$$

where E_0 is the field amplitude, t_0 is the pulse center, σ is the pulse width, $\hbar\omega_f$ is the photon energy, and Φ is the phase of the electric field relative to the Gaussian envelope. The

corresponding TDSE reads

$$i\hbar \dot{c}_k(t) = c_k(t)V_k - i\hbar \sum_j c_j(t)[\dot{\vec{R}} \cdot \vec{d}_{kj} - i\vec{E}(t) \cdot \vec{\mu}_{kj}], \quad (7)$$

and we obtain the rate of change of population as

$$\dot{\rho}_{jj} = \sum_{k \neq j} -2\text{Re}[\rho_{jk} \dot{\vec{R}} \cdot \vec{d}_{kj}] + 2\text{Re}[i\rho_{jk}\vec{E}(t) \cdot \vec{\mu}_{kj}]. \quad (8)$$

The probability of hopping is then given as in Eq. (5). However, for this case, the velocity is only adjusted if the hop is due to the nuclear motion and not if the hop is mediated by the electric field as the energy for the hop is transferred to the system by the external field. To decide if a hop is due to the external electric field or due to the nuclear motion, the ratio of the magnitude of the two terms in Eq. (8) is calculated and a Monte Carlo strategy is employed to sample the ratio and to decide on the velocity adjustment.

B. Initial conditions, photoionization, and Auger decay

Initial nuclear positions and velocities on the ground-state PES of N_2 are obtained by either quasiclassical sampling or Wigner sampling of the normal mode coordinate [42,43].

In the quasiclassical sampling, the ensemble of Cartesian positions **X** and velocities **V** for the classical trajectories are calculated by [43]

$$\mathbf{X}_i = \mathbf{X}_{\text{eq}} + \frac{\mathbf{L}}{\sqrt{M\omega}} \cos(2\pi r_i), \quad (9)$$

$$\mathbf{V}_i = -\frac{\mathbf{L}\sqrt{\omega}}{\sqrt{M}} \sin(2\pi r_i), \quad (10)$$

where $i = 1, \ldots, N$ numbers the sample, **L**, M, and ω are the normal mode coordinate, normal mode mass, and normal mode frequency, respectively, $\mathbf{X}_{\text{eq}}$ is the ground-state equilibrium geometry, and r_i is a uniformly distributed random number in the interval [0,1].
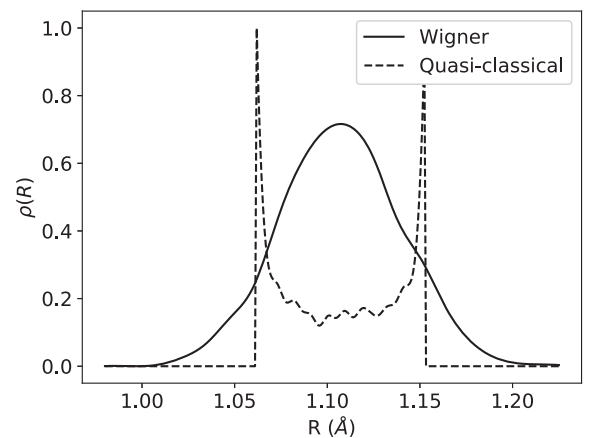

FIG. 1. The distribution of the initial N-N distance obtained from both the Wigner (solid line) and quasiclassical (dashed line) sampling methods.

The Wigner distribution [42] for the vibrational ground state is given as

$$W^{(n=0)}(R, P) = e^{-(P^2+R^2)}, \quad (11)$$

where (R, P) is a point in phase space. The Wigner distribution is sampled employing the von Neumann rejection scheme [42]. The corresponding phase space points are transformed to Cartesian coordinates,

$$\mathbf{X}_i = \mathbf{X}_{eq} + \frac{\mathbf{L}R_i}{\sqrt{M\omega}}, \quad (12)$$

$$\mathbf{V}_i = \frac{\mathbf{L}P_i\sqrt{\omega}}{\sqrt{M}}. \quad (13)$$

Please note that the harmonic approximation is employed in this work for sampling the ground vibrational state of N_2. The average energy of the initial trajectories is thus $\langle E \rangle = \frac{1}{2}\hbar\omega = 0.14$ eV, which is larger than the exact energy expectation value of 0.12 eV [20], the energy of the wave packet employed in the quantum dynamics calculations [20].

Both sampling methods have certain strengths and weaknesses. On the one hand, the Wigner sampling faithfully reproduces the position distribution of the initial quantum wave packet (see Fig. 1). The quasiclassical sampling, however, results in a distribution that peaks at the classical turning points (see Fig. 1). On the other hand, the quasiclassical sampling reproduces the energy spread of the sampled vibrational ground state, $\Delta E = \sqrt{\langle E^2 \rangle - \langle E \rangle^2} = 0$ eV, while
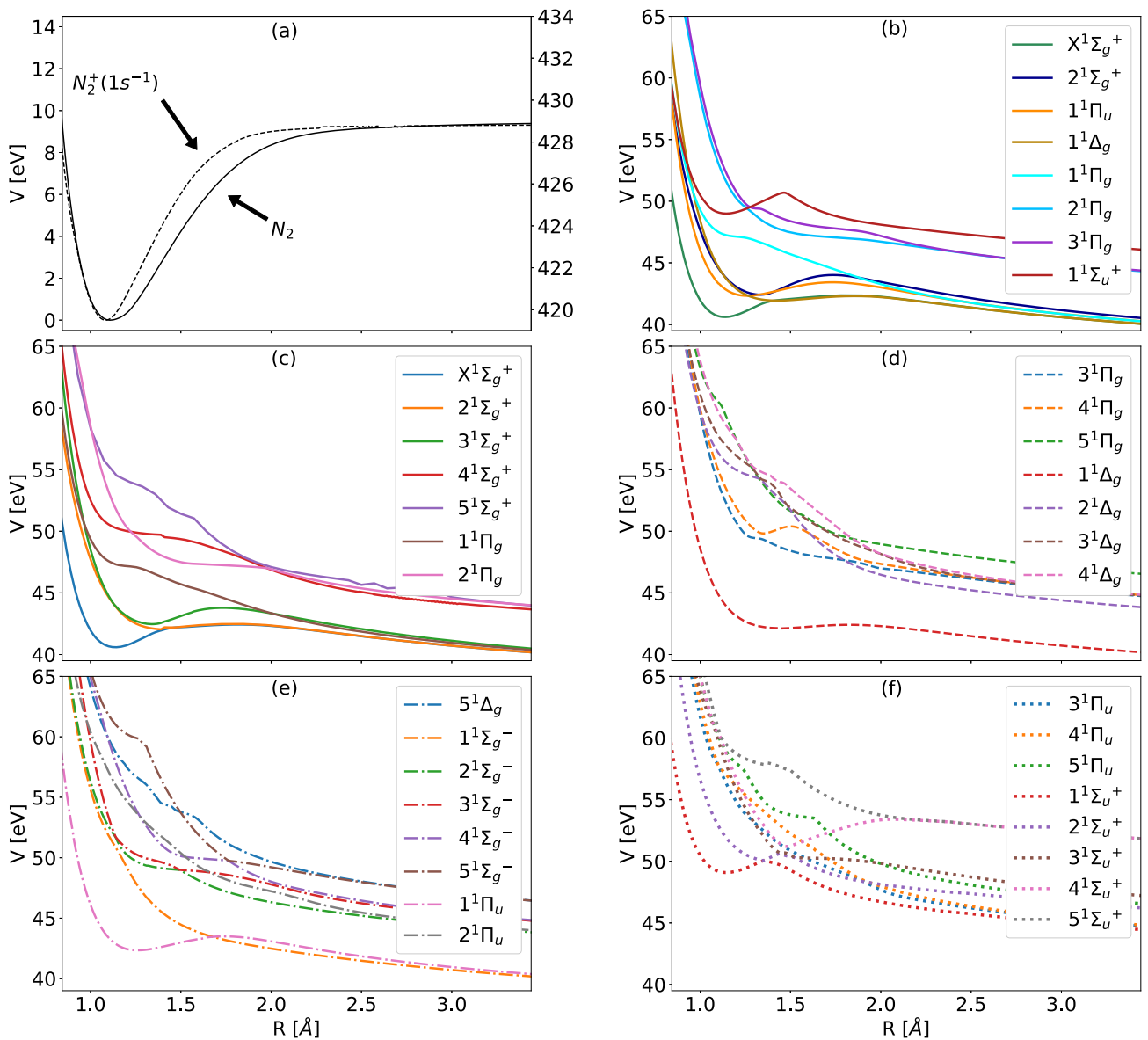

FIG. 2. PESs employed in this work are relative to the ground-state minimum of N_2. (a) The PES of N_2 (solid line) corresponds to the left-hand side y axis and the PES of core-ionized $N_2^+(1s^{-1})$ (dashed line) corresponds to the right-hand-side y axis. (b) Eight quasidiabatic PESs of N_2^{2+} as employed in previous QD simulations [20]. (c)–(f) Thirty adiabatic PESs of N_2^{2+} calculated at the CASSCF/aug-cc-pVTZ level of theory.

the Wigner sampling gives $\Delta E = \frac{1}{2}\hbar\omega = 0.14$ eV for the present case of an initial harmonic state. In this work, we have sampled 5000 trajectories of N_2 molecules that are initially aligned along the z axis. Then a counterclockwise rotation around the y axis with uniformly distributed random angles is performed to mimic the distribution of the rotational ground state relative to the IR polarization axis [20].

The sampled geometries are vertically lifted to the core-ionized N_2^+ electronic state and propagated on that PES. Please note that we follow Ref. [20] and only employ the core-ionized N_2^+ electronic state that corresponds to σ_u symmetry. The N_2^+ electronic state with σ_g symmetry is separated by about 100 meV [16,44] and thus inclusion of this electronic state would only have minimal effect on the results presented. A Monte Carlo scheme is employed to mimic the Auger decay [45,46] and the Auger rates are taken to be the same as in the previous QD simulation [20]. Please note that, following Ref. [20], we assume that the IR pulse has no effect on the Auger decay. If an Auger decay occurs, the trajectory is switched to the corresponding N_2^{2+} state and is subsequently propagated on the manifold of N_2^{2+} electronic states under the influence of the IR pulse as described in Sec. II A.

C. Electronic structure calculations

Electronic structure data such as energies, gradients, nonadiabatic coupling vectors, and transition dipole elements are calculated at the complete active space self-consistent field (CASSCF) level of theory employing the aug-cc-pVTZ basis set developed by Dunning [47] using the MOLCAS 8.2 package [48–51]. The nonadiabatic coupling vector $\vec{d}_{kj}$ is obtained using finite differences as [28]

$$d_{kj}\left(R + \frac{\Delta R}{2}\right) = \frac{1}{2\Delta R}(\langle\phi_k(r;R)|\phi_j(r;R+\Delta R)\rangle$$
$$- \langle\phi_k(r;R+\Delta R)|\phi_j(r;R)\rangle). \quad (14)$$

All the above mentioned electronic structure quantities are calculated on a regular R grid between 0.5 and 3.5 Å at a spacing of 0.01 Å and then interpolated on-the-fly using the smoothed spline interpolation scheme [52–54] in PYTHON. Figure 2 displays the different PESs employed in this work. Figure 2(a) displays the ground electronic state of N_2 and the core-ionized state of N_2^+ [20]. The two PESs are separated by about 420 eV; however, the minimum of the N_2^+ PES is in the Franck-Condon region. Figure 2(b) displays the quasidiabatic PESs of N_2^{2+} that were used in the previous QD simulations [20]. The $X^1\Sigma_g^+$ and $1^1\Sigma_u^+$ states have a local minimum in the Franck-Condon region. In contrast, the local
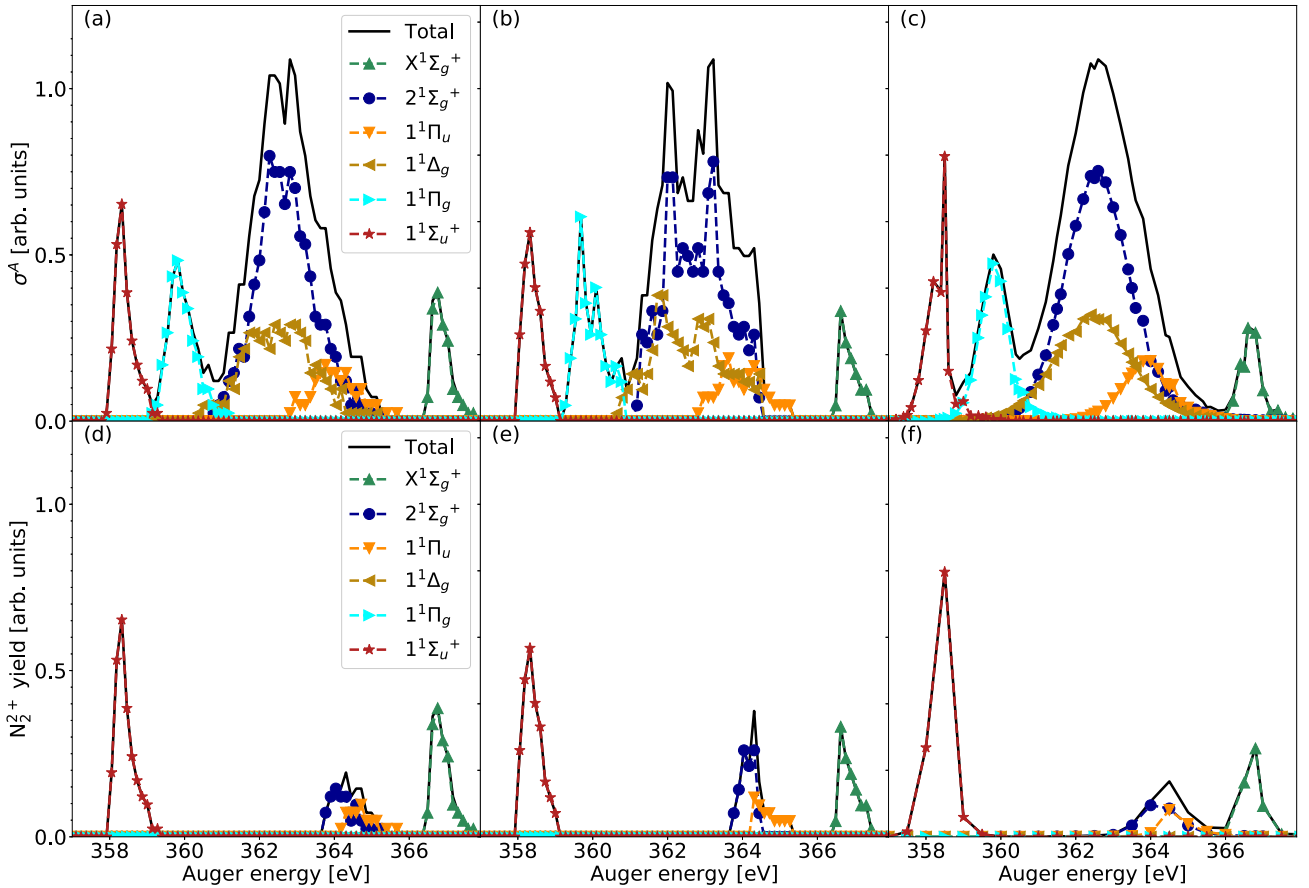

FIG. 3. Auger spectrum using quasidiabatic PESs [shown in Fig. 2(b)] from (a) FSSH (Wigner sampling), (b) FSSH (quasiclassical sampling), and (c) QD [20]. Unfragmented N_2^{2+} (IR free) from (d) FSSH (Wigner sampling), (e) FSSH (quasiclassical sampling), and (f) QD [20].

minima of the $1^1\Delta_g$, $2\,^1\Sigma_g^+$, and $1^1\Pi_u$ states are located outside of the Franck-Condon region, and the $1^1\Pi_g$, $2\,^1\Pi_g$, and $3\,^1\Pi_g$ do not show any local minimum.

Due to the high computational cost of the exact QD simulations, only a small set of quasidiabatic, uncoupled states could be employed in the previous work [20]. As the FSSH simulations performed in this work have a greatly reduced computational cost, we also studied an extended set of 30 adiabatic states of N_2^{2+} in the energy region of interest, which are depicted in Figs. 2(c)–2(f). Additionally, we investigated the role of nonadiabatic coupling in the Coulomb explosion.

III. COMPARISON TO QUANTUM DYNAMICS SIMULATIONS

A. Auger spectrum

In Fig. 3 the Auger electron kinetic-energy spectrum $\sigma^A(E)$ is presented (no IR pulse present). The full Auger spectrum obtained from FSSH employing both Wigner and quasiclassical sampling [Figs. 3(a) and 3(b), respectively] gives very good agreement with previous QD simulations [Fig. 3(c)] [20]. Please note that the Auger spectrum displayed in Fig. 3 is shifted by 11.95 eV, as was done in the QD simulations [20]. The peak positions and the peak widths match the QD spectrum, but small deviations are found for the relative peak heights. The Auger spectrum obtained from quasiclassical sampling shows a small splitting of the peaks, due to the inaccurate initial distribution (see also Fig. 1).

Figures 3(d)–3(f) show the Auger energy dependent unfragmented-N_2^{2+} yield from FSSH employing Wigner sampling (d), quasiclassical sampling (e), and from QD simulations (f) [20]. Very good agreement is found between all three simulations. Auger decay into the $1^1\Pi_g$ state leads to complete dissociation of N_2^{2+} due to its dissociative PES as shown and discussed in Sec. II A. The $1^1\Delta_g$ state has a shallow local minimum away from the Franck-Condon region, which also leads to complete dissociation. The $2\,^1\Sigma_g^+$ and $1^1\Pi_u$ states lead to partial dissociation. The local minimum on each PES
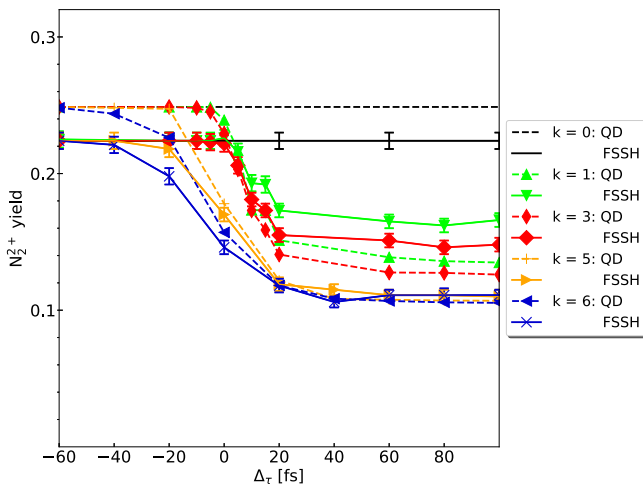
TABLE I. Parameters for the IR pulses employed in this work (cf. Ref. [20]).

IR pulse	I_0 (10^{14} W cm^{-2})	Δ_{IR} (FWHM) (fs)
$k = 0$	–	–
$k = 1$	6.68	3.54
$k = 3$	3.37	7.07
$k = 5$	0.84	28.28
$k = 6$	0.56	42.43

has a considerable depth, but both minima are away from the Franck-Condon region. The overall N_2^{2+} yield from the FSSH calculation is 0.22, which is slightly lower than the value obtained from QD simulations, which is 0.25 [20]. This difference is due to the initial energy of the trajectories, which is greater than the initial energy of the QD wave packet as discussed in Sec. II B. The results obtained with the Wigner sampling resemble the QD results slightly better due to the faithful reproduction of the initial quantum distribution. Thus,
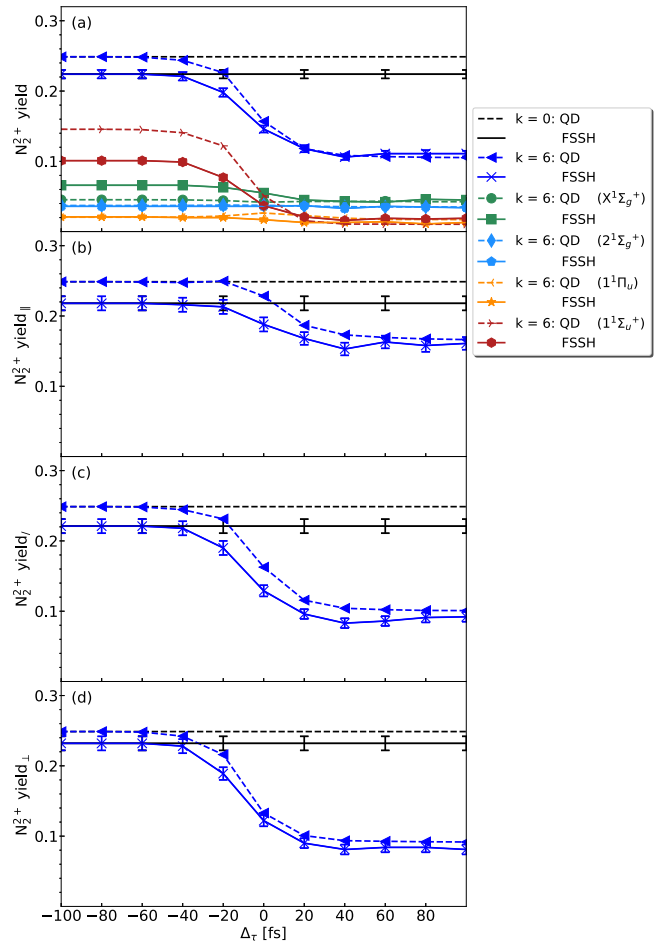

FIG. 5. N_2^{2+} yield with ($k = 6$) and without ($k = 0$) IR pulse. FSSH results are given by solid lines and QD results are given by dashed lines. (a) Overall N_2^{2+} yield as well as contributions from different Auger channels. (b) and (c) N_2^{2+} yield for alignment of N_2 parallel, diagonal, and perpendicular to the IR field.

FIG. 4. N_2^{2+} yield from FSSH (solid lines) and QD (dashed lines) in the presence of IR pulses with the pulse parameters given in Table I.
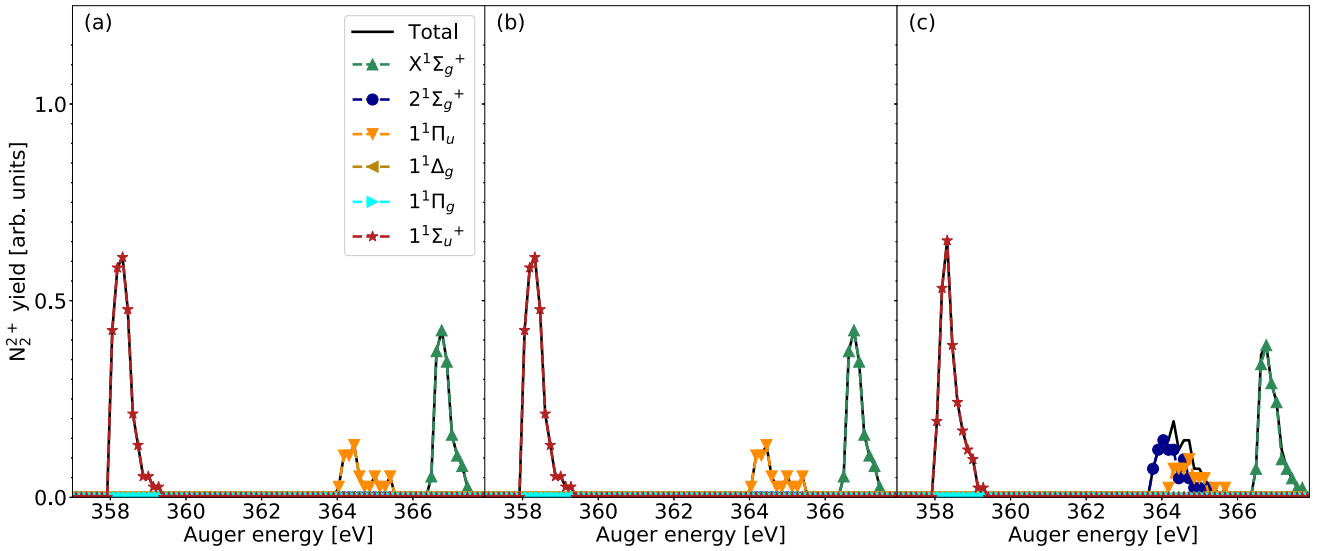
FIG. 6. N_2^{2+} yield (IR free) as a function of energy using the adiabatic PESs [shown in Figs. 2(c)–2(f)] from (a) FSSH (without NAC) and (b) FSSH (with NAC) in comparison to the N_2^{2+} yield from (c) FSSH using quasidiabatic PESs [same as in Fig. 3(d)].

for the remainder of this paper, we will show only results obtained with the Wigner sampling.

B. N_2^{2+} yield in the presence of an IR pulse

Figure 4 shows the unfragmented-N_2^{2+} yield from FSSH (solid lines) and QD [20] (dashed lines) as a function of time delay of an IR pulse, where the parameters of the different IR pulses are given in Table I. As discussed in the previous section (Sec. III A), the IR free ($k = 0$) yield obtained from FSSH is slightly smaller than the yield obtained from QD [20] due to the approximations in the initial sampling. In the presence of long IR pulses ($k = 5$ and $k = 6$), the unfragmented-N_2^{2+} yield from FSSH shows very good agreement with QD [20]. For short IR pulses ($k = 1$ and $k = 3$), we found less N_2^{2+} fragmentation from FSSH than QD [20]. This difference can be rationalized by the approximations in the sampling of the initial conditions. In particular, due to the harmonic approximation, the initial distribution is symmetric as compared to the slightly asymmetric initial distribution of the exact ground state in the QD simulations and the initial energy of the trajectories is slightly overestimated in FSSH. Additionally, the sampling of initial conditions ignores any rovibrational coupling, which is present in the QD simulations. Small differences in the dynamics resulting from the approximations in the sampling manifest themselves more strongly for short IR pulses than long IR pulses, due to less averaging in the former case. These shortcomings could, for example, be overcome by employing the ring polymer molecular dynamics approach [55,56] with nonequilibrium initial conditions [57] and surface hopping [58,59]. This is left for future work.

Figure 5 shows the unfragmented-N_2^{2+} yield as a function of time delay for the long IR pulse ($k = 6$) and no IR pulse ($k = 0$). Figure 5(a) gives the total yield of unfragmented-N_2^{2+}, which we discussed in the previous paragraph. The total unfragmented-N_2^{2+} yield in the presence of a long IR pulse ($k = 6$) shows very good agreement with QD simulations [20].

Figure 5(a) also gives the N_2^{2+} yield from the individual Auger channels. Again good agreement between the FSSH and QD simulations is found. The largest differences can be found for IR free cases (i.e., very negative delay times), which have been discussed above (cf. Fig. 3). In the presence of an IR pulse very good agreement between FSSH and QD simulations is found. The $2^1\Sigma_g^+$ channel does not undergo any fragmentation and $1^1\Pi_u$ undergoes minimal dissociation. The same behavior was observed in the QD simulations [20].

Figures 5(b)–5(d) show the N_2^{2+} yield for different initial alignments of the N_2 molecular axis relative to the IR polarization axis given by an angle θ. To this end, we define three regions: parallel (yield$_\parallel$) to the field ($0° < \theta < 30°$ and $150° < \theta < 180°$), diagonal (yield$_/$) to the field ($30° < \theta < 60°$ and $120° < \theta < 150°$), and perpendicular (yield$_\perp$) to the field ($60° < \theta < 120°$) [20]. All these quantities show good agreement with the QD simulations. The reduced computational cost and better scaling of FSSH compared to QD, while giving overall good agreement, will allow for the investigation of bigger systems and more complex dynamics.

IV. FRAGMENTATION IN ADIABATIC REPRESENTATION

Due to the increased efficiency of the FSSH simulations compared to the QD, we can also investigate the fragmentation dynamics including all 30 adiabatic PESs shown in Figs. 2(c)–2(f). In this section, we also investigate the role of non-Born-Oppenheimer effects due to nonadiabatic coupling of these PESs, which could not be done in the QD simulations [20].

Figure 6 shows the N_2^{2+} yield (IR free) as a function of Auger energy for uncoupled ($\vec{d}_{kj} = 0$) adiabatic PESs [Fig. 6(a)] and coupled adiabatic PESs [Fig. 6(b)] in comparison with the previously discussed results on the quasidiabatic PESs [Fig. 6(c)]. We observe that the state $2^1\Sigma_g^+$ leads to complete dissociation of N_2^{2+} compared to partial dissociation for the quasidiabatic PESs. The difference in fragmentation
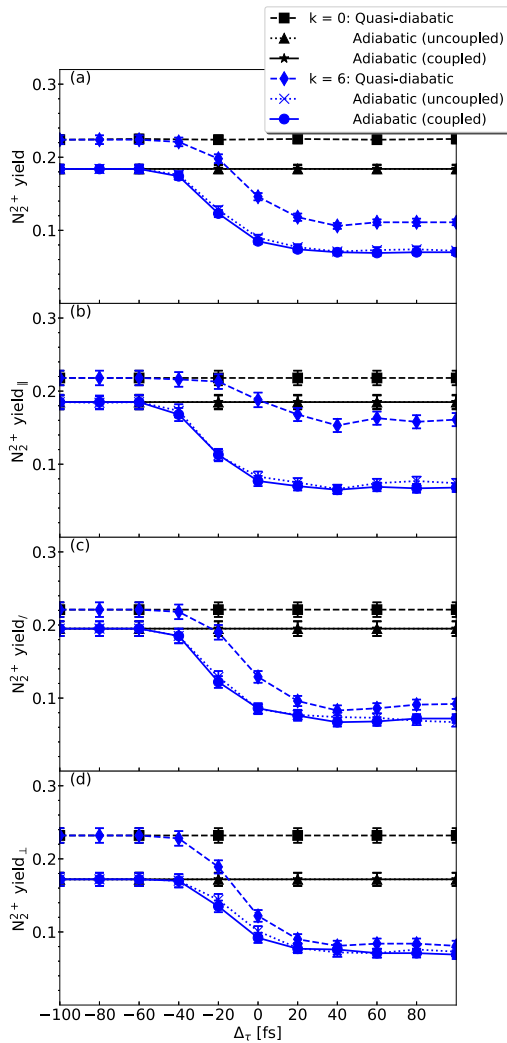
FIG. 7. N_2^{2+} yield from FSSH simulations using quasidiabatic (dashed), uncoupled adiabatic (dotted), and coupled adiabatic (solid) representations. (a) Total N_2^{2+} yield; (b)–(d) N_2 parallel, diagonal, and perpendicular to the IR field.

is due to the higher dissociation barrier on the quasidiabatic PESs, which results from smoothly changing from one to another adiabatic PES when constructing the quasidiabatic PESs and ignoring all off-diagonal potential matrix elements. No difference between the simulations employing uncoupled or fully coupled adiabatic PESs is observed. All other features in the Auger energy dependent IR free N_2^{2+} yield are the same for the adiabatic and quasidiabatic PESs as both sets are similar in the Franck-Condon region.

The increased number of PESs in the simulations that employ the adiabatic representation allows for more possible ways for the IR pulse to excite the system. Therefore, we will now analyze the N_2^{2+} yield when applying an IR pulse. Figure 7 shows the unfragmented-N_2^{2+} yield as a function of time delay of the IR pulse for uncoupled adiabatic (dotted lines) and coupled adiabatic PESs (solid lines) from FSSH simulations in comparison to the previously discussed yield on the quasidiabatic PESs (cf. Fig. 5). The total N_2^{2+} yield is shown in Fig. 7(a). We observe that the IR free N_2^{2+}
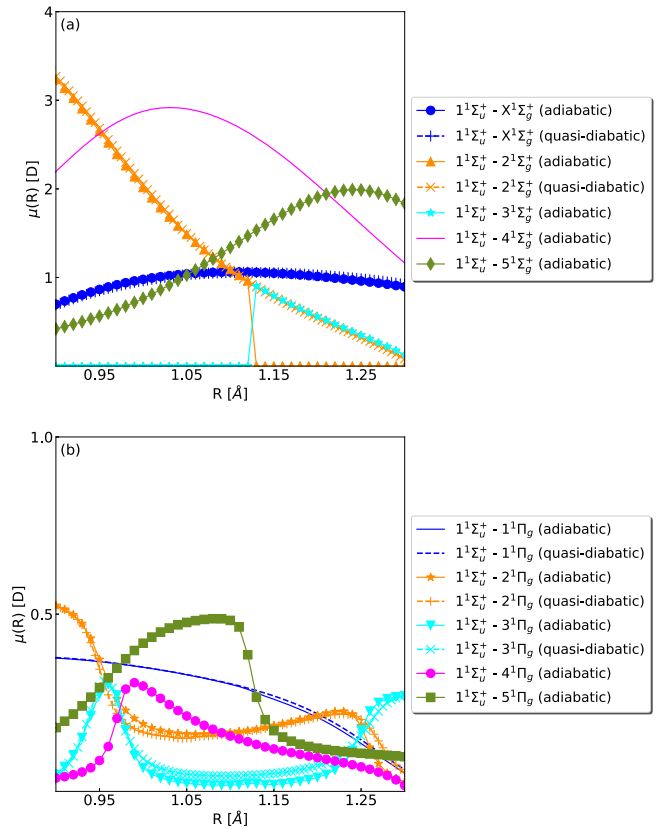

FIG. 8. Magnitude of (a) parallel (z) and (b) perpendicular (x, y) components of the transition dipole moments (μ) of the dominant metastable state $1\,^1\Sigma_u^+$ in the Franck-Condon region.

yield employing the adiabatic PESs (both coupled and uncoupled) is lower than on the quasidiabatic PESs, as discussed above (cf. Fig. 6). Overall, a similar magnitude of dissociation due to the IR pulse is found for the adiabatic and quasidiabatic PESs. No impact of nonadiabatic coupling is found for the cases considered in this work.

Figures 7(b)–7(d) give the unfragmented-N_2^{2+} yield in the three different alignment regions discussed in Sec. III B. In the presence of the IR pulse, we observe a different N_2^{2+} yield in these regions (coupled and uncoupled PESs) compared to the quasidiabatic PESs. This effect is most pronounced for N_2 aligned parallel to the IR field. This difference can be attributed to the inclusion of more adiabatic PESs, which gives trajectories the possibility to hop to more different PESs compared to the previous calculations. This is exemplified for the dominant metastable state $1^1\Sigma_u^+$. Figure 8 shows the parallel and perpendicular components of the transition dipole moment of $1^1\Sigma_u^+$ with respect to the IR pulse polarization. In the previous simulations this state was optically coupled via the parallel component of the transition dipole moment to two other states (i.e., $X\,^1\Sigma_g^+$ and $2\,^1\Sigma_g^+$) in the Franck-Condon region. In contrast, in the extended adiabatic representation, the same state is optically coupled to five other states (i.e., $X\,^1\Sigma_g^+$, $2\,^1\Sigma_g^+$, $3\,^1\Sigma_g^+$, $4\,^1\Sigma_g^+$, and $5\,^1\Sigma_g^+$) via the parallel component of the transition dipole moment in the Franck-Condon region. The states $4\,^1\Sigma_g^+$ and $5\,^1\Sigma_g^+$ in the adiabatic representation

are strongly coupled with the metastable state $1\,^1\Sigma_u^+$ via the parallel component [Fig. 8(a)], which results in increased N_2^{2+} fragmentation when the system is parallel to the IR pulse. Similarly, the same state was optically coupled to three other states (i.e., $1\,^1\Pi_g$, $2\,^1\Pi_g$, and $3\,^1\Pi_g$) via the perpendicular component of the transition dipole in the previous simulations. However, in the extended adiabatic representation, it is coupled to five other states (i.e., $1\,^1\Pi_g$, $2\,^1\Pi_g$, $3\,^1\Pi_g$, $4\,^1\Pi_g$, and $5\,^1\Pi_g$). Unlike the parallel component, the states $4\,^1\Pi_g$ and $5\,^1\Pi_g$ do not have a strong optical coupling via the perpendicular component of the transition dipole moment [Fig. 8(b)]. Thus, the effect of additional states is less strong when the system is diagonal or perpendicular to the IR pulse. Additionally, omitting the quasidiabatic representation and switching to a fully adiabatic representation also changes the coupling pattern. Similar trends are observed also for the other states.

V. CONCLUSION

We have performed x-ray pump-IR probe FSSH simulations of N_2 molecules and compared the results with previous QD simulations [20]. The x-ray pulse photoionizes the N_2 by removing an inner shell electron followed by Auger decay of the N_2^+ system to N_2^{2+}. The interaction of N_2^{2+} with a subsequent IR pulse has been studied. First, we conducted this study in the quasidiabatic (eight N_2^{2+} states) representation employed in the previous QD [20] studies. Results from FSSH simulations for long IR pulses are in good agreement with the QD simulations [20], whereas we observe slightly less fragmentation of N_2^{2+} in the presence of short IR pulses. This can be rationalized by the approximations made for sampling the initial conditions. Due to the increased efficiency of the FSSH simulations, we could reinvestigate the problem employing an extended set of 30 adiabatic PESs. In the adiabatic representation, the total unfragmented-N_2^{2+} yield is decreased compared to simulations in the quasidiabatic representation. Moreover, in contrast to the conclusions of Ref. [20], we find IR-induced molecular fragmentation for parallel alignment to be as strong as for perpendicular alignment. No impact of nonadiabatic coupling is found. FSSH greatly reduced the simulation cost and has a better scaling than QD simulations [20], which opens the door for investigation of fragmentation dynamics for larger systems. Polyatomic systems can be treated in mixed quantum-classical simulations by either on-the-fly electronic structure calculations or by using fitted PES, e.g., employing machine learning techniques.

[1] J. M. Glownia, J. Cryan, J. Andreasson, A. Belkacem, N. Berrah, C. I. Blaga, C. Bostedt, J. Bozek, L. F. DiMauro, L. Fang, J. Frisch, O. Gessner, M. Gühr, J. Hajdu, M. P. Hertlein, M. Hoener, G. Huang, O. Kornilov, J. P. Marangos, A. M. March, B. K. McFarland, H. Merdji, V. S. Petrovic, C. Raman, D. Ray, D. A. Reis, M. Trigo, J. L. White, W. White, R. Wilcox, L. Young, R. N. Coffee, and P. H. Bucksbaum, Opt. Express **18**, 17620 (2010).

[2] P. Emma, R. Akre, J. Arthur, R. Bionta, C. Bostedt, J. Bozek, A. Brachmann, P. Bucksbaum, R. Coffee, F.-J. Decker, Y. Ding, D. Dowell, S. Edstrom, A. Fisher, J. Frisch, S. Gilevich, J. Hastings, G. Hays, P. Hering, Z. Huang, R. Iverson, H. Loos, M. Messerschmidt, A. Miahnahri, S. Moeller, H.-D. Nuhn, G. Pile, D. Ratner, J. Rzepiela, D. Schultz, T. Smith, P. Stefan, H. Tompkins, J. Turner, J. Welch, W. White, J. Wu, G. Yocky, and J. Galayda, Nat. Photon. **4**, 641 (2010).

[3] N. Berrah, L. Fang, T. Osipov, B. Murphy, C. Bostedt, and J. D. Bozek, J. Electron. Spectrosc. Relat. Phenom. **196**, 34 (2014).

[4] T. Osipov, L. Fang, B. Murphy, F. Tarantelli, E. R. Hosler, E. Kukk, J. D. Bozek, C. Bostedt, E. P. Kanter, and N. Berrah, J. Phys. B: At., Mol. Opt. Phys. **46**, 164032 (2013).

[5] B. F. Murphy, L. Fang, M.-H. Chen, J. D. Bozek, E. Kukk, E. P. Kanter, M. Messerschmidt, T. Osipov, and N. Berrah, Phys. Rev. A **86**, 053423 (2012).

[6] L. Fang, T. Osipov, B. Murphy, F. Tarantelli, E. Kukk, J. P. Cryan, M. Glownia, P. H. Bucksbaum, R. N. Coffee, M. Chen, C. Buth, and N. Berrah, Phys. Rev. Lett. **109**, 263001 (2012).

[7] R. W. Wetmore and R. K. Boyd, J. Phys. Chem. **90**, 5540 (1986).

[8] P. R. Taylor and H. Partridge, J. Phys. Chem. **91**, 6148 (1987).

[9] B. Kempgens, A. Kivimäki, M. Neeb, H. M. Köppe, A. M. Bradshaw, and J. Feldhaus, J. Phys. B: At. Mol. Opt. Phys. **29**, 5389 (1996).

[10] W. Jiang, Y. G. Khait, and M. R. Hoffmann, J. Chem. Phys. **127**, 164308 (2007).

[11] J. P. Cryan, J. M. Glownia, J. Andreasson, A. Belkacem, N. Berrah, C. I. Blaga, C. Bostedt, J. Bozek, N. A. Cherepkov, L. F. DiMauro, L. Fang, O. Gessner, M. Gühr, J. Hajdu, M. P. Hertlein, M. Hoener, O. Kornilov, J. P. Marangos, A. M. March, B. K. McFarland, H. Merdji, M. Messerschmidt, V. S. Petrović, C. Raman, D. Ray, D. A. Reis, S. K. Semenov, M. Trigo, J. L. White, W. White, L. Young, P. H. Bucksbaum, and R. N. Coffee, J. Phys. B: At. Mol. Opt. Phys. **45**, 055601 (2012).

[12] H. Ågren, J. Chem. Phys. **75**, 1267 (1981).

[13] W. E. Moddeman, T. A. Carlson, M. O. Krause, B. P. Pullen, W. E. Bull, and G. K. Schweitzer, J. Chem. Phys. **55**, 2317 (1971).

[14] S. Svensson, A. N. de Brito, M. P. Keane, N. Correia, L. Karlsson, C. M. Liegener, and H. Agren, J. Phys. B: At. Mol. Opt. Phys. **25**, 135 (1992).

[15] G. Víkor, S. Ricz, L. Tóth, B. Sulik, J. Végh, Á. Kövér, and L. Kövér, Nucl. Instrum. Methods Phys. Res. B **124**, 393 (1997).

[16] S. Sorensen, C. Miron, R. Feifel, M. N. Piancastelli, O. Björne-holm, and S. Svensson, Chem. Phys. Lett. **456**, 1 (2008).

[17] Y. H. Jiang, A. Rudenko, M. Kurka, K. U. Kühnel, T. Ergler, L. Foucar, M. Schöffler, S. Schössler, T. Havermeier, M. Smolarski, K. Cole, R. Dörner, S. Düsterer, R. Treusch, M.

Gensch, C. D. Schröter, R. Moshammer, and J. Ullrich, Phys. Rev. Lett. **102**, 123002 (2009).

[18] E. Gagnon, P. Ranitovic, X.-M. Tong, C. L. Cocke, M. M. Murnane, H. C. Kapteyn, and A. S. Sandhu, Science **317**, 1374 (2007).

[19] P. Franceschi, D. Ascenzi, P. Tosi, R. Thissen, J. Žabka, J. Roithová, C. L. Ricketts, M. D. Simone, and M. Coreno, J. Chem. Phys. **126**, 134310 (2007).

[20] A. M. Hanna, O. Vendrell, A. Ourmazd, and R. Santra, Phys. Rev. A **95**, 043419 (2017).

[21] H.-D. Meyer, U. Manthe, and L. Cederbaum, Chem. Phys. Lett. **165**, 73 (1990).

[22] M. Beck, A. Jäckle, G. Worth, and H.-D. Meyer, Phys. Rep. **324**, 1 (2000).

[23] H.-D. Meyer and G. A. Worth, Theor. Chem. Acc. **109**, 251 (2003).

[24] J. C. Tully, J. Chem. Phys. **93**, 1061 (1990).

[25] J. C. Tully, Int. J. Quantum Chem. **40**, 299 (1991).

[26] J. C. Tully, Faraday Discuss. **110**, 407 (1998).

[27] N. Doltsinis and D. Marx, J. Theor. Comput. Chem. **1**, 319 (2002).

[28] E. Fabiano, T. Keal, and W. Thiel, Chem. Phys. **349**, 334 (2008).

[29] G. Granucci and M. Persico, J. Chem. Phys. **126**, 134114 (2007).

[30] G. Granucci, M. Persico, and A. Zoccante, J. Chem. Phys. **133**, 134111 (2010).

[31] J. J. Bajo, G. Granucci, and M. Persico, J. Chem. Phys. **140**, 044113 (2014).

[32] J. Petersen and R. Mitrić, Phys. Chem. Chem. Phys. **14**, 8299 (2012).

[33] R. Mitrić, J. Petersen, and V. Bonačić-Koutecký, Phys. Rev. A **79**, 053416 (2009).

[34] G. Tomasello, M. Wohlgemuth, J. Petersen, and R. Mitrić, J. Phys. Chem. B **116**, 8762 (2012).

[35] J. Petersen, M. Wohlgemuth, B. Sellner, V. Bonačić-Koutecký, H. Lischka, and R. Mitrić, Phys. Chem. Chem. Phys. **14**, 4687 (2012).

[36] P. Marquetand, M. Richter, J. González-Vázquez, I. Sola, and L. González, Faraday Discuss. **153**, 261 (2011).

[37] J. J. Bajo, J. González-Vázquez, I. R. Sola, J. Santamaria, M. Richter, P. Marquetand, and L. González, J. Phys. Chem. A **116**, 2800 (2012).

[38] D. Geißler, P. Marquetand, J. González-Vázquez, L. González, T. Rozgonyi, and T. Weinacht, J. Phys. Chem. A **116**, 11434 (2012).

[39] M. E.-A. Madjet, Z. Li, and O. Vendrell, J. Chem. Phys. **138**, 094311 (2013).

[40] S. Bazzi, R. Welsch, O. Vendrell, and R. Santra, J. Phys. Chem. A **122**, 1004 (2018).

[41] F. Agostini, A. Abedi, and E. K. U. Gross, J. Chem. Phys. **141**, 214101 (2014).

[42] L. Sun and W. L. Hase, J. Chem. Phys. **133**, 044313 (2010).

[43] W. L. Hase and D. G. Buckowski, Chem. Phys. Lett. **74**, 284 (1980).

[44] U. Hergenhahn, O. Kugeler, A. Rüdel, E. E. Rennie, and A. M. Bradshaw, J. Phys. Chem. A **105**, 5704 (2001).

[45] Y. Hao, L. Inhester, K. Hanasaki, S.-K. Son, and R. Santra, Struct. Dyn. **2**, 041707 (2015).

[46] S.-K. Son and R. Santra, Phys. Rev. A **85**, 063415 (2012).

[47] J. T. H. Dunning, J. Chem. Phys. **90**, 1007 (1989).

[48] G. Karlström, R. Lindh, P.-Å. Malmqvist, B. O. Roos, U. Ryde, V. Veryazov, P.-O. Widmark, M. Cossi, B. Schimmelpfennig, P. Neogrády, and L. Seijo, Comput. Mater. Sci. **28**, 222 (2003).

[49] V. Veryazov, P.-O. Widmarka, L. Serrano-Andres, R. Lindh, and B. Roos, Int. J. Quantum Chem. **100**, 626 (2004).

[50] F. Aquilante, L. D. Vico, N. Ferré, G. Ghigo, P.-Å. Malmqvist, P. Neogrády, T. Pedersen, M. Pitoňák, M. Reiher, B. Roos, L. Serrano-Andrés, M. Urban, V. Veryazov, and R. Lindh, J. Comput. Chem. **31**, 224 (2010).

[51] F. Aquilante, J. Autschbach, R. K. Carlson, L. F. Chibotaru, M. G. Delcey, L. D. Vico, I. F. Galván, N. Ferré, L. M. Frutos, L. Gagliardi, M. Garavelli, A. Giussani, C. E. Hoyer, G. L. Manni, H. Lischka, D. Ma, P. Å. Malmqvist, T. Müller, A. Nenov, M. Olivucci, T. B. Pedersen, D. Peng, F. Plasser, B. Pritchard, M. Reiher, I. Rivalta, I. Schapiro, J. Segarra-Martí, M. Stenrup, D. G. Truhlar, L. Ungur, A. Valentini, S. Vancoillie, V. Veryazov, V. P. Vysotskiy, O. Weingart, F. Zapata, and R. Lindh, J. Comput. Chem. **37**, 506 (2016).

[52] C. de Boor, J. Approx. Theory **6**, 50 (1972).

[53] M. G. Cox, J. Inst. Maths Applics **10**, 134 (1972).

[54] P. Dierckx, *Monographs on Numerical Analysis* (Oxford University Press, Oxford, 1995).

[55] I. R. Craig and D. E. Manolopoulos, J. Chem. Phys. **121**, 3368 (2004).

[56] S. Habershon, D. E. Manolopoulos, T. E. Markland, and T. F. Miller, Annu. Rev. Phys. Chem. **64**, 387 (2013).

[57] R. Welsch, K. Song, Q. Shi, S. C. Althorpe, and T. F. Miller, J. Chem. Phys. **145**, 204118 (2016).

[58] P. Shushkov, R. Li, and J. C. Tully, J. Chem. Phys. **137**, 22A549 (2012).

[59] R. Kaur and R. Welsch (unpublished).

5.3   Choice of the electronic basis for field-induced surface hopping

Murali Krishna Ganesa Subramanian, Robin Santra and Ralph Welsch

Phys. Rev. A, **102**, 013107 (2020).

Statement of contribution

The theoretical concept was developed by Robin Santra. All the analytical work was carried out by myself under the guidance of Robin Santra and Ralph Welsch. The writing of manuscript was partly done by Ralph Welsch and myself.

Choice of the electronic basis for field-induced surface hopping

Murali Krishna Ganesa Subramanian [1,2] Robin Santra [1,2,3] and Ralph Welsch [1,3]

[1]*Center for Free-Electron Laser Science, DESY, Notkestrasse 85, 22607 Hamburg, Germany*
[2]*Department of Physics, Universität Hamburg, Jungiusstrasse 9, 20355 Hamburg, Germany*
[3]*The Hamburg Centre for Ultrafast Imaging, Luruper Chaussee 149, 22761 Hamburg, Germany*

A method combining an Ehrenfest-like approach, which minimizes the number of surface hops, with Tully's fewest switches surface hopping is proposed for the description of nonadiabatic molecular dynamics in the presence of an external electromagnetic field. When two states are strongly coupled by the applied light field, an Ehrenfest-like approach is employed, which allows the system to be in a coherent superposition. Tully's fewest switches surface hopping (FSSH) is used for the weak- and no-coupling regimes to improve the asymptotic behavior of the method. The decision of which approach to employ at a given time is made based on a simple analysis of Rabi oscillations in a two-state model. The method is tested for two exactly solvable model systems, i.e., a stimulated emission scenario in a pulsed laser field and a photoexcitation scenario in a cw laser field. Position and momentum densities of the nuclei compare well with exact quantum dynamics simulations and improve on both a pure Ehrenfest and a pure FSSH approach. The method is efficient and easily implemented.

I. INTRODUCTION

Key phenomena in molecular processes such as charge transfer and transport [1–5], isomerization [6,7], photo-deactivation [8,9], or singlet fission [10] can be understood by investigating the dynamics on an atomic scale. In many of these processes, the Born-Oppenheimer approximation breaks down and we have to treat the coupled motion of electrons and nuclei. While exact, full-dimensional quantum dynamics approaches can readily simulate this, the computational effort of these methods scales exponentially with increasing system size. Therefore, mixed quantum classical descriptions, i.e., approaches employing a classical description of the nuclei and a quantum description of the electrons, have been developed. These methods include the Ehrenfest or mean-field approach [11,12] and Tully's fewest switches surface hopping (FSSH) approach [13–15].

In Ehrenfest dynamics, the nuclei evolve classically due to a force from a superposition of electronic eigenstates. However, due to the averaged potential, Ehrenfest dynamics fails to correctly describe processes with multiple reaction paths or processes that end up in distinct states that are well described by a single potential energy surface (PES). These processes can be better described by the popular FSSH approach. In FSSH, each classical trajectory evolves on a single PES and stochastically hops between the different PESs. The transition probabilities depend on the electronic population and on the nonadiabatic coupling (NAC) vector. For every hop, the velocities are scaled to conserve energy. By employing this energy-conservation procedure, the FSSH algorithm can approximately reproduce the Boltzmann distribution of quantum states. It allows for the FSSH method to investigate the relaxation of quantum states to thermal equilibrium [16], which is not possible in the Ehrenfest approach [16,17]. FSSH is an appealing approach due to its conceptual simplicity and

numerical efficiency, while being reasonably accurate. However, FSSH has several limitations such as missing nuclear quantum effects and quantum interference, lack of proper decoherence, and representation dependence [18]. In recent years, there has been a considerable theoretical advancement to overcome such limitations. Some of the recently developed FSSH-like algorithms include ring polymer surface hopping [19–24], global flux surface hopping (GFSH) [25], Liouville space FSSH [26], Liouville space GFSH [27], decoherence-induced surface hopping [28], and many others [29–38].

Further developments of the FSSH algorithm have focused on incorporating an external electric field to investigate light-induced nonadiabatic dynamics [39–42]. In field-induced FSSH, the PESs are optically coupled by the transition dipole moment μ. The basic states that are then employed in the FSSH algorithm can either be the field-free, adiabatic Born-Oppenheimer surfaces (BO-SH) [39,43–50] or instantaneous Born-Oppenheimer surfaces that are eigenstates of the electronic Hamiltonian including the electric field at time t (IBO-SH) [51–56]. However, it has recently been shown that for photoexcitation and stimulated emission processes in an exactly solvable H_2^+ model, these approaches suffer from an unphysically high average number of hops per trajectory, which lead to nonphysical results compared to full quantum simulations [57]. Another FSSH variant employing Floquet surfaces within the FSSH scheme, i.e., Floquet surface hopping (F-SH) [40,57], was found to reduce the average number of hops and, consequently, better reproduce the exact results. Yet, the Floquet picture is strictly exact only for time-periodic cw laser fields. In the present work, we propose an improved version of field-induced BO-SH, which we term optimized BO-SH (o-BO-SH), in which the number of hops per trajectory is minimized. To this end, the method employs an Ehrenfest-like approach in the strongly coupled region and regular BO-SH elsewhere. A simple analysis of Rabi oscillations in a two-state

model allows for the distinction of these two situations. The method is compared to exact quantum calculations as well as other surface hopping variants discussed in Ref. [57]. Similar ideas have been proposed for nonadiabatic dynamics without an external field [58–62], which will be discussed in Sec. IV.

The paper is organized as follows: In Sec. II, the model system employed in this work is introduced, the basic field-induced FSSH approach is reviewed, and the method proposed in this work is discussed in detail. Section III presents results on a model system and comparison to other works. Section IV gives a general discussion of the presented method and puts it into perspective, while Sec. V presents some conclusions.

II. THEORETICAL BACKGROUND

A. Model system and potential energy surfaces

In order to facilitate a systematic comparison, we follow Ref. [57] and employ a soft-core Hamiltonian given as

$$H = -\frac{\Delta_R}{2M} - \frac{\Delta_r}{2} + \frac{1}{R + 0.03} - \mu E(t)$$
$$- \frac{1}{\sqrt{(r - R/2)^2 + 1}} - \frac{1}{\sqrt{(r + R/2)^2 + 1}}, \quad (1)$$

where M is the reduced nuclear mass, R and r are the nuclear and electronic coordinates, respectively, and μ is the transition dipole moment operator. The BO surfaces $E_{0/1}^{\mathrm{BO}}(R)$ are calculated by diagonalizing the field-free Hamiltonian for fixed nuclear coordinates [57],

$$H^{\mathrm{BO}}(R) = -\frac{\Delta_r}{2} + \frac{1}{R + 0.03} - \frac{1}{\sqrt{(r - R/2)^2 + 1}}$$
$$- \frac{1}{\sqrt{(r + R/2)^2 + 1}}. \quad (2)$$

The IBO Hamiltonian includes the electric-field interaction $\mu E(t)$ and reads

$$H^{\mathrm{IBO}}(R, t) = H^{\mathrm{BO}}(R) - \mu E(t), \quad (3)$$

with the corresponding IBO energies $E_{0/1}^{\mathrm{IBO}}(R, t)$ given by [57]

$$E_{0/1}^{\mathrm{IBO}}(R, t) = E_{0/1}^{\mathrm{BO}}(R)\cos^2\theta(R, t) + E_{1/0}^{\mathrm{BO}}(R)\sin^2\theta(R, t)$$
$$\pm \mu_{01}^{\mathrm{BO}}(R)E(t)\sin2\theta(R, t), \quad (4)$$

where the mixing parameter $\theta(R, t)$ is given by [57]

$$\theta(R, t) = \frac{1}{2}\arctan\frac{2\mu_{01}^{\mathrm{BO}}(R)E(t)}{E_0^{\mathrm{BO}}(R) - E_1^{\mathrm{BO}}(R)}. \quad (5)$$

In this work, we have considered two cases of molecular dissociation following Ref. [57]: a Na_2^+-like molecule ($M = 23 \times 918$ a.u.) undergoing stimulated emission due to a Gaussian-shaped laser pulse with intensity $I = 3 \times 10^{12}$ W/cm^2 (see Sec. III A) and an H_2^+-like molecule ($M = 918$ a.u.) undergoing photon absorption due to a cw laser with intensity $I = 1 \times 10^{13}$ W/cm^2 (see Sec. III B). In the latter case, the initial trajectories were given an additional momentum of -2.5 a.u. The photon energy of the electromagnetic field is $\hbar\omega = 0.2$ a.u., which resonantly couples the lowest
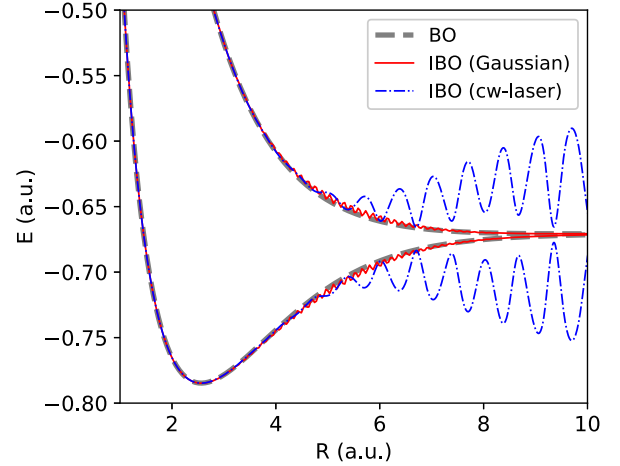

FIG. 1. The two lowest BO and IBO PESs [for both cases: stimulated emission (curve with smaller oscillations) and photon absorption (curve with bigger oscillations)], with the equilibrium distance, $R_{\mathrm{eq}} \approx 2.3$ a.u. The IBO surfaces were obtained by evolving a single classical trajectory, starting on the upper PES at $R = 0.85$ a.u. with zero initial momentum and employing the electric fields and reduced nuclear masses described in Sec. II A. As a consequence, the IBO PESs do not correspond to any single time— different points in space are calculated at different times.

two PESs at around $R = 3.5$ a.u. The two PESs are optically coupled via the dipole moment, which for the model system is approximated as $\mu_{kj} = \delta_{kj}R/2$. Figure 1 shows the lowest two BO and IBO PESs (for both cases described above).

B. Fewest switches surface hopping

A central component of the method proposed in this work is Tully's FSSH approach and the implementation largely follows Ref. [63]. In FSSH, the electrons are treated quantum mechanically, while the nuclei are treated classically, propagating along a trajectory $R(t)$. The classical trajectories evolve on a single PES and can switch between the electronic states based on a hopping probability. In the model cases employed here, the PESs are coupled only through the transition dipole moment μ_{kj} and, hence, we set the nonadiabatic-coupling vector $d_{kj} = 0$ throughout the simulations. We will focus on one-dimensional systems here, but the approach can be easily generalized to many degrees of freedom. We employ different field-induced FSSH variants. In BO-SH, we solve the time-dependent electronic Schrödinger equation (TDSE) along the nuclear trajectories employing the BO surfaces,

$$i\dot{c}_k(t) = \sum_j c_j(t)\left[V_{kj}^{\mathrm{BO}} - E(t)\mu_{kj}\right], \quad (6)$$

where the c_k's are the expansion coefficients of the electronic wave function and the V_{kj}^{BO} are the matrix elements of the field-free electronic Hamiltonian in the adiabatic representation, i.e., they are zero for $k \neq j$, and for $k = j$ they are the eigenvalues of the field-free Hamiltonian for fixed nuclei coordinates [i.e., $E_{0/1}^{\mathrm{BO}}(R)$]. The rate of change of the electronic

population is given by

$$\dot{\rho}_{jj}(t) = \sum_{k \neq j} 2\mathrm{Re}[i\rho_{jk}(t)E(t)\mu_{kj}]. \qquad (7)$$

The probability of hopping from state j to state k, $P_{j \to k}$, is obtained as [63]

$$P_{j \to k}(t) = \frac{-2\mathrm{Re}[i\rho_{jk}E(t)\mu_{kj}]\Delta t}{\rho_{jj}}. \qquad (8)$$

In case of IBO-SH, we use the IBO surfaces, $E_{0/1}^{\mathrm{IBO}}(R)$, and the time evolution of the expansion coefficients is derived using the Hellmann-Feynman theorem:

$$i\dot{c}_k(t) = \sum_j c_j(t)\left[V_{kj}^{\mathrm{IBO}} - \frac{i\dot{E}(t)\mu_{kj}}{\Delta E_{jk}^{\mathrm{IBO}}}\right], \qquad (9)$$

where $\Delta E_{jk}^{\mathrm{IBO}} = E_j^{\mathrm{IBO}} - E_k^{\mathrm{IBO}}$. The rate of change of the electronic population is given by

$$\dot{\rho}_{jj}(t) = -\sum_{k \neq j} 2\mathrm{Re}\left[\frac{\rho_{jk}\dot{E}(t)\mu_{kj}}{\Delta E_{jk}^{\mathrm{IBO}}}\right], \qquad (10)$$

and the probability of hopping from state j to state k is given as

$$P_{j \to k}(t) = 2\mathrm{Re}\left[\frac{\rho_{jk}(t)\dot{E}(t)\mu_{kj}}{\Delta E_{jk}^{\mathrm{IBO}}}\right]\frac{\Delta t}{\rho_{jj}(t)}. \qquad (11)$$

We assume that the energy required for any hop is provided by the field and thus do not perform any velocity adjustments after a hop occurs.

C. Optimized BO-SH

In this work, we propose a modified FSSH approach that we term the "optimized" BO-SH (o-BO-SH) method. It consists of two parts described in detail below. The first part aims at reducing the number of hops. To this end, we employ a

time-dependent transformation of the electronic basis. For the two-state model investigated here, this part is equivalent to an Ehrenfest approach. The second part consists of a criterion for when to employ the optimization and when to employ standard BO-SH. This part is based on the description of Rabi oscillations.

1. Optimization

In order to reduce the number of field-induced hops, the underlying electronic basis is transformed. The transformation matrix at each time step is obtained by minimizing the instantaneous hopping probability. For a two-state case, the transformation matrix reads

$$U(\theta, \phi) = \begin{bmatrix} \cos\theta & \sin\theta e^{i\phi} \\ -\sin\theta e^{-i\phi} & \cos\theta \end{bmatrix}, \qquad (12)$$

where θ and ϕ are parameters that are optimized at each time step and thus carry the time dependence. We note that there is no need to optimize the global phase of the electronic wave packet. Therefore, the parametrization employed in Eq. (12) captures all relevant SU(2) transformation matrices. Parametrizations for SU(n) matrices with $n > 2$ (i.e., for electronic subspaces consisting of more than two states) are available but are less straightforward [64].

The corresponding time-dependent Schrödinger equation in the new basis (labeled with a prime) reads

$$i\dot{c'}_k(t) = \sum_j c'_j(t)\left[\sum_a U_{ka}(\theta, \phi)V_{aa}^{\mathrm{BO}}U_{aj}^\dagger(\theta, \phi) \right.$$
$$\left. - \sum_{a,b} U_{ka}(\theta, \phi)E(t)\mu_{ab}U_{bj}^\dagger(\theta, \phi) \right.$$
$$\left. - i\sum_a U_{ka}(\theta, \phi)\dot{U}_{aj}^\dagger(\theta, \phi)\right], \qquad (13)$$

and the probability of hopping from a state j to state k is given by

$$P_{j \to k}(t) = \frac{-2\mathrm{Re}\{\left[-i\sum_a U_{ka}V_{aa}^{\mathrm{BO}}U_{aj}^\dagger + i\sum_{a,b} U_{ka}E(t)\mu_{ab}U_{bj}^\dagger + \sum_a U_{ka}\dot{U}_{aj}^\dagger\right]\rho'_{kj}\}\Delta t}{\rho'_{jj}}. \qquad (14)$$

Therefore, $P_{j \to k}$ is a function of θ and ϕ. Please note that j and k in Eq. (14) do not refer to BO PESs but to "optimized" PESs defined below. To reduce the number of hops, we minimize $P_{j \to k}$ with respect to θ and ϕ, i.e., $\min_{\theta, \phi} P_{j \to k}(\theta, \phi) = P_{j \to k}(\theta_{\mathrm{opt}}, \phi_{\mathrm{opt}})$ and obtain optimal values θ_{opt} and ϕ_{opt} at each time step. We perform the minimization using the function *minimize* from the Python library SciPy [65]. The temporal derivative of U, required for evaluating the hopping probability in Eq. (14), can be expressed in terms of $\dot{\theta}$ and $\dot{\phi}$, which we compute employing first-order finite differencing. This approach is numerically stable as long as the time step is small enough.

We carry out the standard FSSH algorithm with the new set of optimized PESs $V^o = U(\theta_{\mathrm{opt}}, \phi_{\mathrm{opt}})V^{\mathrm{BO}}U^\dagger(\theta_{\mathrm{opt}}, \phi_{\mathrm{opt}})$. Each classical trajectory then evolves on the optimized PES V_j^o, where j labels the current active electronic state of the

trajectory just as in FSSH. Gradients for solving Newton's equations of motion are obtained as approximate derivatives of the optimized PES, i.e., as

$$\frac{\partial}{\partial R}V_j^o = \sum_a U_{ja}(\theta_{\mathrm{opt}}, \phi_{\mathrm{opt}})\left(\frac{\partial}{\partial R}V_{aa}^{\mathrm{BO}}\right)U_{aj}^\dagger(\theta_{\mathrm{opt}}, \phi_{\mathrm{opt}}).$$

2. Criterion for employing the optimization

In order to reduce the field-induced hops, the optimization procedure is carried out when there is strong optical coupling through the transition dipole moment μ. However, as mentioned above, we find that for the cases investigated here, the optimization procedure described above results in an approach very close to the Ehrenfest approach. However, once the coupling is weak, the system will stay in the optimized, averaged state, which can lead to nonphysical behavior if the
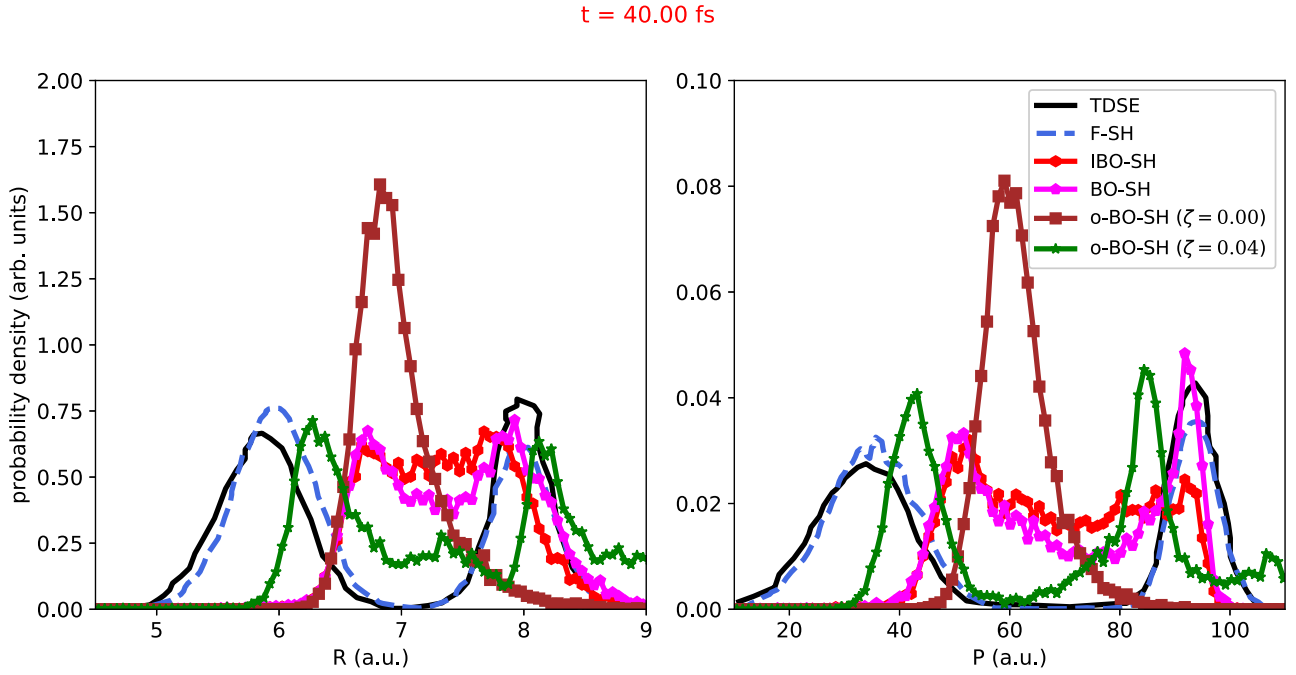
FIG. 2. The nuclear densities for scenario 1 at $t = 40$ fs, in position (left panel) and momentum (right panel) space, obtained from BO-SH, IBO-SH, and o-BO-SH for $\zeta = 0.00$ and o-BO-SH for $\zeta = 0.04$, in the presence of a Gaussian pulse, in comparison to TDSE and F-SH from Ref. [57].

two states show distinct gradients, similar to the problems arising in Ehrenfest dynamics. Thus, once the strength of the optical coupling is small, one should revert back to employing the normal BO PESs. To determine if the coupling is small, we employ a resonantly coupled two-level model exhibiting Rabi oscillations. The probability for switching the state in this model is given as

$$P_{\text{Rabi}} = \frac{|\epsilon(t)\mu_{01}|^2}{\left(\omega - \Delta E_{01}^{\text{BO}}\right)^2 + |E(t)\mu_{01}|^2},$$ (15)

where ω and $\epsilon(t)$ are the photon energy and the envelope associated with the electric field $E(t) = \epsilon(t)\cos(\omega t)$, and $\Delta E_{01}^{\text{BO}} = E_0^{\text{BO}} - E_1^{\text{BO}}$ is the energy difference of the two BO states. Therefore, once the switching probability is above a threshold value ζ, we employ the optimization algorithm described above and, if it is below that threshold value, we switch back to the BO PESs. To this end, we calculate the absolute square of the expansion coefficients of the current electronic state with respect to the k-th BO state, which gives the probability to switch to the k-th BO PES. A Monte Carlo strategy similar to the standard FSSH approach is employed to sample these probabilities.

III. RESULTS

The model systems employed in this work are described in Sec. II A. We consider two cases of molecular dissociation: A Na_2^+-like molecule undergoing stimulated emission due to a Gaussian pulse (see Sec. III A) and an H_2^+-like molecule undergoing photon absorption due to a cw laser (see Sec. III B). Throughout this work, we employ 10 000 classical trajectories sampled using Wigner sampling. Trajectories are propa-

gated using the Velocity-Verlet approach with a time step of 0.002 a.u.

A. Scenario 1: Stimulated emission in Gaussian pulse

First we discuss stimulated emission from an electronically excited Na_2^+-like molecule ($M = 23 \times 918$ a.u.) by a Gaussian pulse with 7 fs duration (full width at half maximum of the intensity), wavelength of $\lambda = 225$ nm, and peak intensity of $I = 3 \times 10^{12}$ W/cm^2.

Figure 2 shows the nuclear position and momentum densities at $t = 40$ fs, obtained from BO-SH, IBO-SH, and o-BO-SH in comparison with results from Ref. [57] employing F-SH and exact TDSE calculations. Here, *position* means internuclear distance, and *momentum* refers to the relative momentum of the two nuclei. The latter is positive when the two nuclei are moving away from each other; it is negative when they are approaching each other. The exact momentum density in Fig. 2(b) shows that the wave packet splits into a fast moving part (mean momentum $P \approx 94$ a.u. at $t = 40$ fs) and a slow moving part (mean momentum $P \approx 34$ a.u. at $t = 40$ fs). The fast moving part is on the ground electronic state and shows a mean position of $R \approx 5.9$ a.u., while the slow moving part is located on the excited electronic state and shows a mean position of $R \approx 7.9$ a.u.

The F-SH simulations from Ref. [57] show a similar behavior. However, both the BO-SH and IBO-SH approaches show a less distinct splitting in the densities. As discussed in Ref. [57], this failure can be attributed to the high number of hops per trajectory in these two approaches compared to F-SH (see also Table I). The optimization method introduced in this work reduces the number of hops. Yet, the pure optimization method (i.e., $\zeta = 0$), which reduces the number of hops to 0,

TABLE I. The average number of hops per trajectory in different FSSH methods for scenarios 1 and 2. The numbers for F-SH are taken from Ref. [57] (note the interchange of scenarios 1 and 2).

Method	Scenario 1	Scenario 2
F-SH	0.6	0.01
BO-SH	1.45	3.16
IBO-SH	2.15	42.3
o-BO-SH ($\zeta = 0.00$)	0.00	0.00
o-BO-SH ($\zeta = 0.04$)	0.98	0.22
o-BO-SH ($\zeta = 0.10$)	1.13	
o-BO-SH ($\zeta = 0.50$)	2.21	

shows no splitting at all due to the Ehrenfest-like character of that approach. If a larger value of ζ is employed, $\zeta = 0.04$ in this case, the trajectories are put onto the correct BO PES after they passed the coupling region and a distinct splitting of the distribution is found, which is closer to the exact values than pure BO- or IBO-SH.

The choice of an appropriate value for ζ is discussed next. It is clear that a too low value of ζ results in an Ehrenfest-like approach, which does not give reasonable results here, while a too high value of ζ results in a pure BO-SH approach, which is also unreasonable for the strongly driven systems discussed here. The observation in different tests is that while the coupling is strong, the optimization strategy performs well, and where the coupling is weak, the FSSH approach performs better. By examining Fig. 3, which shows the spatial dependence of the Rabi switching probability given in Eq. (15) for the current scenario, we can decide on a reasonable range for the ζ parameter. It can be seen that the switching probability peaks at the geometry where the frequency of the external field matches the energy difference of the two electronic states and that it falls off very quickly away from that point. To include
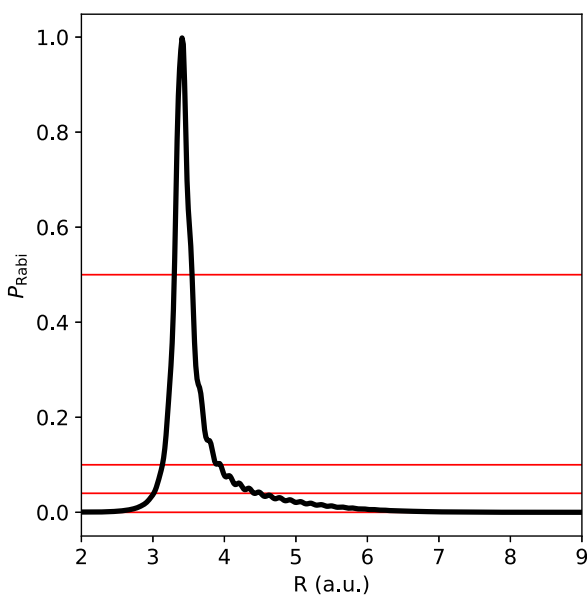

FIG. 3. Rabi switching probability, P_{Rabi}, as a function of position R.

the strong-coupling regime in the optimization algorithm, one therefore needs to choose a small, but nonzero value of ζ.

To gain better insight into the optimal value as well as the sensitivity of our results with respect to ζ, we performed simulations with $\zeta \in \{0, 0.04, 0.1, 0.5\}$. These values are also indicated as horizontal lines in Fig. 3. In Fig. 4, the resulting nuclear position and momentum densities for simulations with the different values of ζ are compared. At $t = 10$ fs, before the system enters the interaction region, all densities are equal. However, once the two states are coupled by the external laser field (e.g., around $t = 15$ fs), one can see the momentum density splitting up significantly for a high value of ζ (yellow and cyan line in Fig. 4). This is due to the high-ζ value forcing the system into one or the other BO PES while there is still significant coupling of the two states. As seen before, a value of $\zeta = 0$ results in no splitting of the density and an averaged position and momentum distribution, which is nonphysical.

The effect discussed above can be seen even better in Fig. 5, which shows the momentum density as a function of the θ optimization parameter at selected times. At $t = 15$ fs and a high value of ζ (second row, left column of Fig. 5), one can see that most of the trajectories are located either on the upper or lower BO PES, i.e., θ is either 0 or $\frac{\pi}{2}$. For $\zeta = 0$, one can see that there is no splitting and the systems ends up in an average state, i.e., the values of θ that are reached are always below $\frac{\pi}{2}$ and above 0, with an average close to $\frac{\pi}{4}$. Furthermore, over the full time, the distribution in θ is continuous and relatively compact.

B. Scenario 2: Photon absorption in cw laser

In this scenario, an H_2^+-like molecule ($M = 918$ a.u.) initially in its ground electronic state, but with an additional momentum of -2.5 a.u., is considered. The system evolves in a cw laser with $I = 10^{13}$ W/cm^2, switched on with a sin^2-shaped ramp (given in Ref. [57]).

Figure 6 shows the nuclear position and momentum densities at $t = 25$ fs obtained from BO-SH, IBO-SH, and o-BO-SH (for $\zeta = 0.0$ and 0.04) in comparison to calculations employing F-SH and exact TDSE simulations from Ref. [57]. A split in the wave packet is observed in the exact simulation, with one part staying in the ground electronic state and around the equilibrium position and a second part dissociating in the excited electronic state. Again, F-SH gives reasonably good results compared to the exact results. In contrast, both BO-SH and IBO-SH underestimate the dissociation probability and give a too small momentum for the dissociating part at $t = 25$ fs. This can be traced back to the high number of hops in BO- and IBO-SH (see Table I).

For this scenario, the o-BO-SH approach performs well compared to the exact approach not only for $\zeta = 0.4$, but also for $\zeta = 0.0$. The reason for the latter value to work well is as follows. The system is initialized in the ground electronic state near the potential minimum. For trajectories that stay in this region, there is only a small coupling, and thus θ will remain around 0 in the optimization algorithm and the trajectories correctly evolve on the ground electronic state. Only if the trajectories have enough energy to escape from the potential minimum is there a significant coupling and the trajectories start to evolve on optimized, average
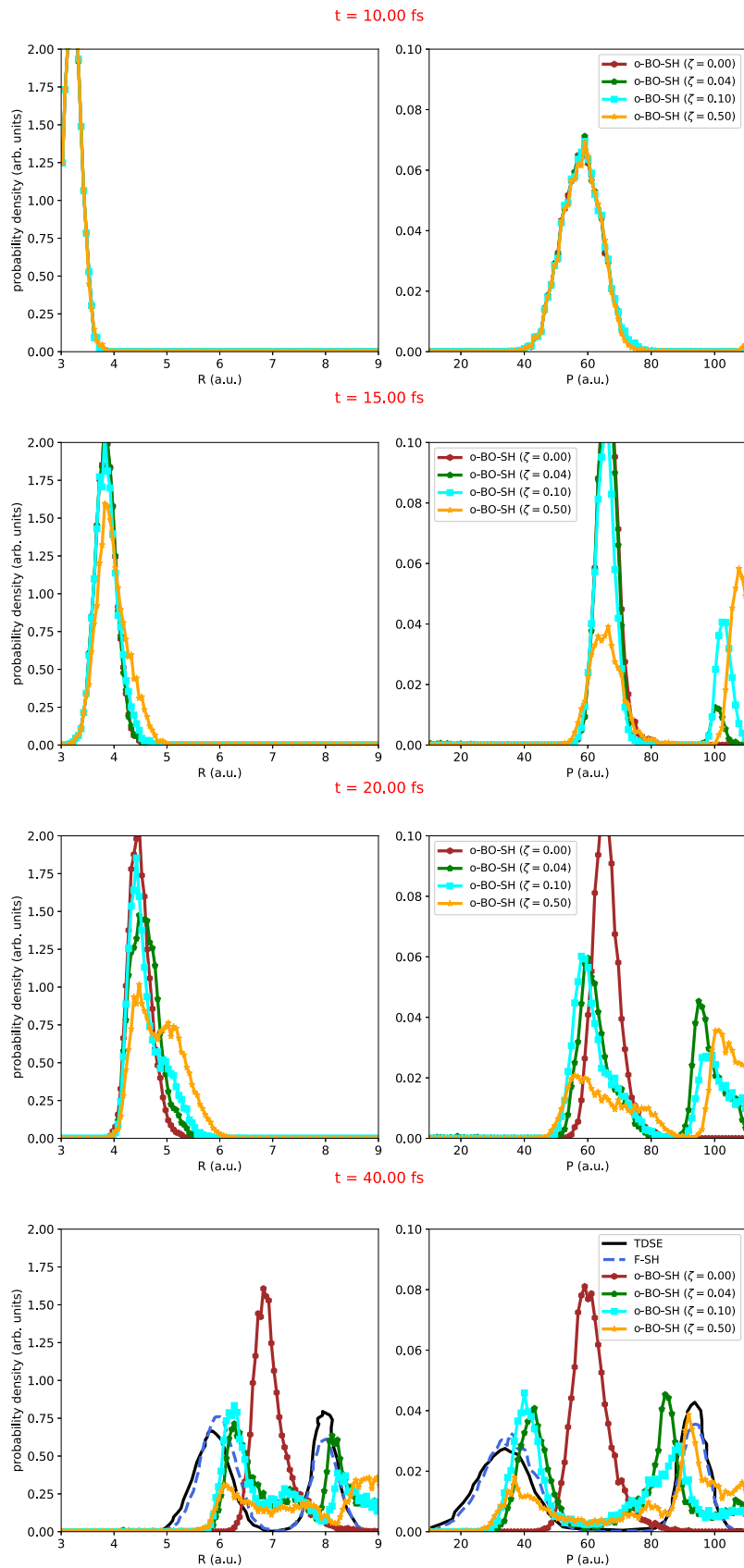
FIG. 4. Snapshots of nuclear densities at $t = 10, 15, 20$, and 40 fs in position (left panel) and momentum (right panel) space, o-BO-SH for $\zeta = 0.5, 0.1, 0.04$, and 0.0. At $t = 40$ fs, the nuclear densities from o-BO-SH are compared to TDSE and F-SH from Ref. [57].
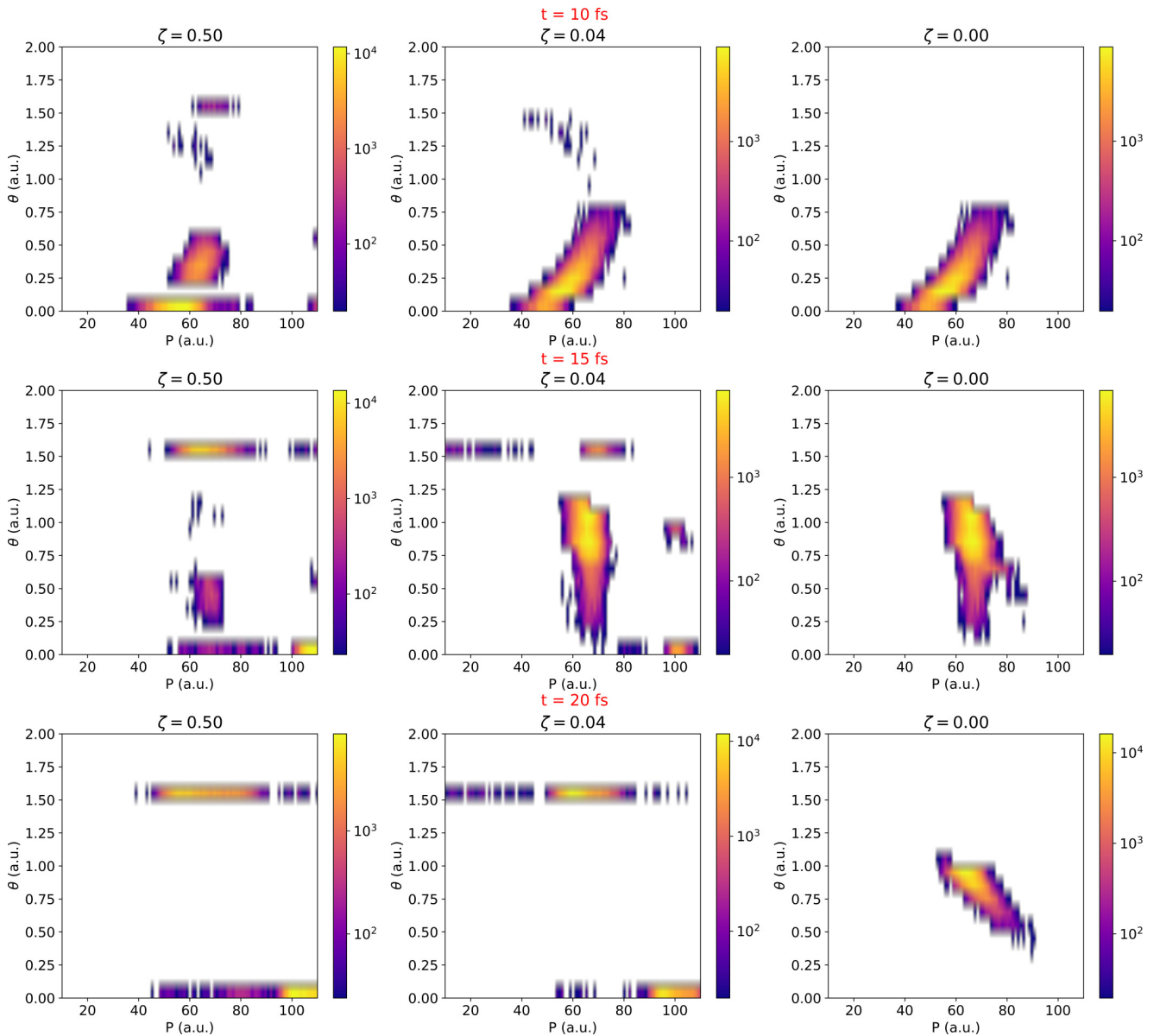
FIG. 5. The logarithmic distribution of momentum, P, and mixing parameter θ, at $t = 10$, 15, and 20 fs employing o-BO-SH for $\zeta = 0.50$ (left panels), 0.04 (center panels), and 0.0 (right panels).

states. However, for this dissociation case, there is no problem as the electronic states are degenerate in the dissociation limit.

Figure 7 shows the nuclear momentum density as a function of the optimization parameter θ at $t = 25$ fs from o-BO-SH for $\zeta = 0.04$. Again, $\theta = 0$ corresponds to a population of the lower BO PES, while a value of $\theta = \frac{\pi}{2}$ corresponds to a population of the upper BO PES. The two peaks in the momentum distribution can be directly associated with a population of the lower BO PES (peak around $P = 0$ a.u.) and the second peak associated with a population of the upper BO PES (peak around $P = 12$ a.u.), where the latter peak shows a broader θ distribution as both BO PESs are approximately degenerate at large distances.

IV. DISCUSSION

For cases where the external field strongly couples the different BO PESs, it is best to describe each trajectory using a superposition of BO states, as done in the Ehrenfest approach, instead of a simple BO state, which is employed in FSSH. However, once the strong coupling is no longer present, the Ehrenfest-like approach breaks down as the system cannot be described with a coherent superposition any longer, but each state should be treated individually as is done in FSSH. The proposed method combines these in a straightforward and easy-to-implement way, which also gives accurate results.

Methods that follow a similar spirit as o-BO-SH have been proposed before [58–62], yet only for cases that do not include an external electric field. The continuous surface
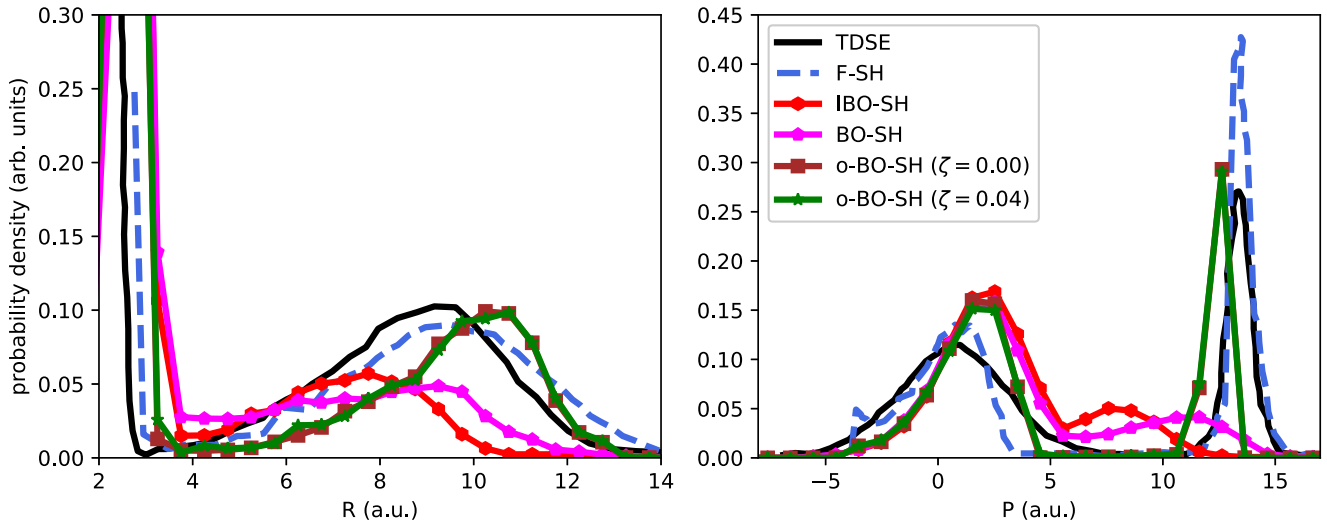
t = 25 fs

FIG. 6. The nuclear densities for scenario 2 at $t = 25$ fs, in position (left panel) and momentum (right panel) space, obtained from BO-SH, IBO-SH, o-BO-SH for $\zeta = 0.00$ and o-BO-SH for $\zeta = 0.04$, in the presence of a cw laser, in comparison to TDSE and F-SH from Ref. [57].

switching approaches (CSS, CCS2) [59,60] are variants of the Ehrenfest approach, but redefine the weights in the wave function. In areas of strong coupling, the weights should match the electronic populations and thus the approaches equal the Ehrenfest approach, while in areas of no coupling, the weights should be 0 or 1 to ensure correct dissociation. One of the important criteria for the definition of the weights is that the wave function should collapse in the regions of weak or no coupling. In that way, CSS and CSS2 are similar to the o-BO-SH method, which also uses the current coupling strength as a criterion for the wave-function collapse. However, in our o-BO-SH, the collapse of the wave functions is instantaneous, while CSS and CSS2 have a continuous way of collapsing

t = 25 fs

FIG. 7. The logarithmic distribution of momentum, P, and mixing parameter θ, at $t = 25$ fs employing o-BO-SH for $\zeta = 0.04$.

the wave function over some range of the potential. Mean-field dynamics with stochastic decoherence (MF-SD) [61] and augmented Ehrenfest (AE) [62] both have an instantaneous collapse of the wave function given by a rate. The rate is determined by analyzing either the difference between the Ehrenfest force and the forces for each electronic state [61] or by analyzing the Ehrenfest trajectories employing frozen Gaussians [62], which both differ from the o-BO-SH method that analyzes the coupling strength due to the external field.

For the two-state examples employed in this work, it was found that the optimization approach gives the same results as the Ehrenfest approach. It is not clear whether this holds true in any multistate case. Both approaches, i.e., the Ehrenfest approach and the optimization, can be easily implemented for a multistate case. The Ehrenfest approach is well known for any number of states, whereas for the optimization procedure, one needs to define a general, unitary matrix, perform the associated transformation of the electronic basis, and employ any standard optimization scheme to minimize the hopping probability.

V. CONCLUSION

For the mixed quantum classical description of the dynamics of molecules driven by coherent light fields, the F-SH method from Ref. [57] overcomes certain limitations of the Ehrenfest, BO-SH, and IBO-SH methods. However, the Floquet method underlying F-SH imposes restrictions on the nature of the light pulses that can be treated. Particularly, few-cycle or subcycle pulses, which can be synthesized for applications in quantum control [66,67], clearly violate the assumption of temporal (quasi-)periodicity inherent in the Floquet method. In contrast, the Ehrenfest, BO-SH, and IBO-SH methods are not affected by this specific limitation of F-SH.

Therefore, in this work, we have explored another FSSH variant for computing field-induced dynamics in molecules.
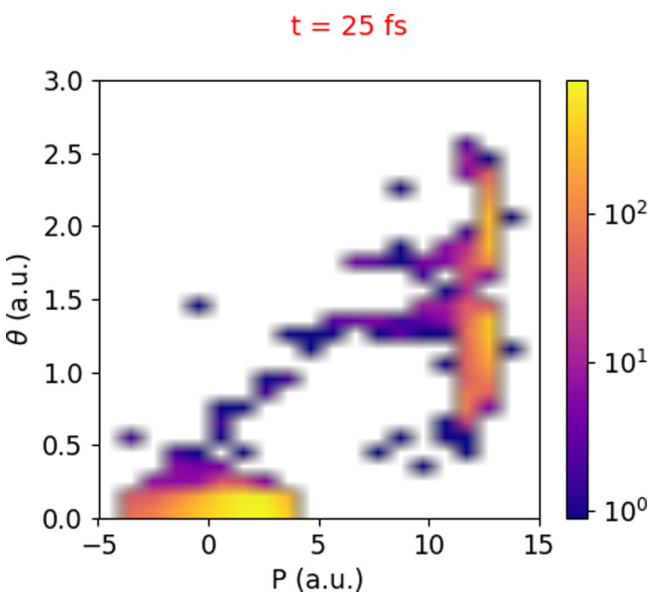
The proposed method combines an Ehrenfest-like approach for the strong-coupling region, which reduces the number of hops, and BO-SH in the weak-coupling regime. The switch between both approaches is performed based on a Rabi-oscillation model. The method is termed optimized BO-SH (o-BO-SH) and performs well compared to exact quantum results for different test cases of field-induced stimulated emission and photoabsorption employing a soft-core Hamiltonian. It is numerically efficient and can be easily generalized to treat multidimensional and multistate systems. It is left for future work to assess the accuracy of the method in these cases.

[1] A. Migliore, N. F. Polizzi, M. J. Therien, and D. N. Beratan, Chem. Rev. **114**, 3381 (2014).

[2] M. Cordes and B. Giese, Chem. Soc. Rev. **38**, 892 (2009).

[3] E. H. Jung, N. J. Jeon, E. Y. Park, C. S. Moon, T. J. Shin, T.-Y. Yang, J. H. Noh, and J. Seo, Nature (London) **567**, 511 (2019).

[4] T. M. Brenner, D. A. Egger, L. Kronik, G. Hodes, and D. Cahen, Nat. Rev. Mater. **1**, 15007 (2016).

[5] A. R. Arnold, M. A. Grodick, and J. K. Barton, Cell Chem. Biol. **23**, 183 (2016).

[6] O. P. Ernst, D. T. Lodowski, M. Elstner, P. Hegemann, L. S. Brown, and H. Kandori, Chem. Rev. **114**, 126 (2014).

[7] P. J. M. Johnson, A. Halpin, V. I. Prokhorenko, O. P. Ernst, and R. J. D. Miller, Nat. Chem. **7**, 980 (2015).

[8] M. Barbatti, A. J. A. Aquino, J. J. Szymczak, D. Nachtigallová, P. Hobza, and H. Lischka, Proc. Natl. Acad. Sci. **107**, 21453 (2010).

[9] K. Kleinermanns, D. Nachtigallová, and M. S. de Vries, Int. Rev. Phys. Chem. **32**, 308 (2013).

[10] M. B. Smith and J. Michl, Annu. Rev. Phys. Chem. **64**, 361 (2013).

[11] P. Ehrenfest, Z. Phys. **45**, 455 (1927).

[12] O. V. Prezhdo and V. V. Kisil, Phys. Rev. A **56**, 162 (1997).

[13] J. C. Tully, J. Chem. Phys. **93**, 1061 (1990).

[14] J. C. Tully, Int. J. Quantum Chem. **40**, 299 (1991).

[15] J. C. Tully, Faraday Discuss. **110**, 407 (1998).

[16] P. V. Parandekar and J. C. Tully, J. Chem. Phys. **122**, 094102 (2005).

[17] A. E. Sifain, L. Wang, and O. V. Prezhdo, J. Chem. Phys. **142**, 224102 (2015).

[18] L. Wang, A. Akimov, and O. V. Prezhdo, J. Phys. Chem. Lett. **7**, 2100 (2016).

[19] P. Shushkov, R. Li, and J. C. Tully, J. Chem. Phys. **137**, 22A549 (2012).

[20] R. Welsch, K. Song, Q. Shi, S. C. Althorpe, and T. F. Miller, J. Chem. Phys. **145**, 204118 (2016).

[21] R. Kaur and R. Welsch, J. Chem. Phys. **150**, 114105 (2019).

[22] F. A. Shakib and P. Huo, J. Phys. Chem. Lett. **8**, 3073 (2017).

[23] X. Tao, P. Shushkov, and T. F. Miller, J. Chem. Phys. **148**, 102327 (2018).

[24] X. Tao, P. Shushkov, and T. F. Miller, J. Phys. Chem. A **123**, 3013 (2019).

[25] L. Wang, D. Trivedi, and O. V. Prezhdo, J. Chem. Theory Comput. **10**, 3598 (2014).

[26] L. Wang, A. E. Sifain, and O. V. Prezhdo, J. Phys. Chem. Lett. **6**, 3827 (2015).

[27] L. Wang, A. E. Sifain, and O. V. Prezhdo, J. Chem. Phys. **143**, 191102 (2015).

[28] H. M. Jaeger, S. Fischer, and O. V. Prezhdo, J. Chem. Phys. **137**, 22A545 (2012).

[29] A. V. Akimov and O. V. Prezhdo, Phys. Rev. Lett. **113**, 153003 (2014).

[30] A. V. Akimov, D. Trivedi, L. Wang, and O. V. Prezhdo, J. Phys. Soc. Jpn. **84**, 094002 (2015).

[31] L. Wang and O. V. Prezhdo, J. Phys. Chem. Lett. **5**, 713 (2014).

[32] L. Wang and D. Beljonne, J. Phys. Chem. Lett. **4**, 1888 (2013).

[33] A. V. Akimov, R. Long, and O. V. Prezhdo, J. Chem. Phys. **140**, 194107 (2014).

[34] J. E. Subotnik and N. Shenvi, J. Chem. Phys. **134**, 024105 (2011).

[35] V. N. Gorshkov, S. Tretiak, and D. Mozyrsky, Nat. Commun. **4**, 2144 (2013).

[36] N. Shenvi, J. E. Subotnik, and W. Yang, J. Chem. Phys. **135**, 024101 (2011).

[37] L. Wang, R. Long, and O. V. Prezhdo, Annu. Rev. Phys. Chem. **66**, 549 (2015).

[38] A. V. Akimov and O. V. Prezhdo, Chem. Rev. **115**, 5797 (2015).

[39] R. Mitrić, J. Petersen, and V. Bonačić Koutecký, Phys. Rev. A **79**, 053416 (2009).

[40] T. Fiedlschuster, J. Handt, and R. Schmidt, Phys. Rev. A **93**, 053409 (2016).

[41] Y. Suzuki, A. Abedi, N. T. Maitra, and E. K. U. Gross, Phys. Chem. Chem. Phys. **17**, 29271 (2015).

[42] M. Richter, P. Marquetand, J. González-Vázquez, I. Sola, and L. González, J. Chem. Theory Comput. **7**, 1253 (2011).

[43] I. Tavernelli, B. F. E. Curchod, and U. Rothlisberger, Phys. Rev. A **81**, 052508 (2010).

[44] G. A. Jones, A. Acocella, and F. Zerbetto, J. Phys. Chem. A **112**, 9650 (2008).

[45] R. Mitrić, J. Petersen, M. Wohlgemuth, U. Werner, V. Bonačić-Koutecký, L. Wöste, and J. Jortner, J. Phys. Chem. A **115**, 3755 (2011).

[46] J. Petersen and R. Mitrić, Phys. Chem. Chem. Phys. **14**, 8299 (2012).

[47] J. J. Bajo, G. Granucci, and M. Persico, J. Chem. Phys. **140**, 044113 (2014).

[48] M. Fischer, J. Handt, and R. Schmidt, Phys. Rev. A **90**, 012525 (2014).

[49] M. Fischer, J. Handt, and R. Schmidt, Phys. Rev. A **90**, 012526 (2014).

[50] M. Fischer, J. Handt, and R. Schmidt, Phys. Rev. A **90**, 012527 (2014).

[51] F. Kelkensberg, G. Sansone, M. Y. Ivanov, and M. Vrakking, Phys. Chem. Chem. Phys. **13**, 8647 (2011).

[52] J. J. Bajo, J. González-Vázquez, I. R. Sola, J. Santamaria, M. Richter, P. Marquetand, and L. González, J. Phys. Chem. A **116**, 2800 (2012).

[53] I. Horenko, B. Schmidt, and C. Schütte, J. Chem. Phys. **115**, 5733 (2001).

[54] P. Dietrich, M. Y. Ivanov, F. A. Ilkov, and P. B. Corkum, Phys. Rev. Lett. **77**, 4150 (1996).

[55] M. Thachuk, M. Y. Ivanov, and D. M. Wardlaw, J. Chem. Phys. **105**, 4094 (1996).

[56] M. Thachuk, M. Y. Ivanov, and D. M. Wardlaw, J. Chem. Phys. **109**, 5747 (1998).

[57] T. Fiedlschuster, J. Handt, E. K. U. Gross, and R. Schmidt, Phys. Rev. A **95**, 063424 (2017).

[58] M. Herman, J. Chem. Phys. **110**, 4141 (1999).

[59] Y. L. Volobuev, M. D. Hack, M. S. Topaler, and D. G. Truhlar, J. Chem. Phys. **112**, 9716 (2000).

[60] M. D. Hack and D. G. Truhlar, J. Chem. Phys. **114**, 2894 (2001).

[61] M. J. Bedard-Hearn, R. E. Larsen, and B. J. Schwartz, J. Chem. Phys. **123**, 234106 (2005).

[62] J. E. Subotnik, J. Chem. Phys. **132**, 134112 (2010).

[63] M. K. Ganesa Subramanian, R. Santra, and R. Welsch, Phys. Rev. A **98**, 063421 (2018).

[64] T. Tilma and E. C. G. Sudarshan, J. Phys. A **35**, 10467 (2002).

[65] P. Virtanen *et al.*, Nat. Methods **17**, 261 (2020).

[66] A. Wirth, M. Th. Hassan, I. Grguras, J. Gagnon, A. Moulet, T. T. Luu, S. Pabst, R. Santra, Z. A. Alahmed, A. M. Azzeer, V. S. Yakovlev, V. Pervak, F. Krausz, and E. Goulielmakis, Science **334**, 195 (2011).

[67] S.-W. Huang, G. Cirmi, J. Moses, K.-H. Hong, S. Bhardwaj, J. R. Birge, L.-J. Chen, E. Li, B. J. Eggleton, G. Cerullo, and F. X. Kärtner, Nat. Photon. **5**, 475 (2011).